Sintering and Particle Dynamics in Supported Metal Catalysts

Hansen, Thomas Willum; Ståhl, Kenny

Publication date:
2006

Document Version
Publisher's PDF, also known as Version of record

Sintering and Particle Dynamics in Supported Metal Catalysts

Thomas Willum Hansen

Ph.D. thesis

January 2006

Haldor Topsøe A/S,
University of New Mexico
&
Technical University of Denmark

Preface

The work presented in this thesis is carried out in the Materials Characterization Group at Haldor Topsøe A/S in Lyngby, Denmark under the supervision of Poul Lenvig Hansen and Stig Helveg, and at Center for Micro-Engineered Materials in the Department of Chemical and Nuclear Engineering at the University of New Mexico under the supervision of Abhaya K. Datye, all under the supervision of Kenny Ståhl.

The involved institutions of the projects had different instrumentation and expertise to offer. These have been utilized in the best possible manor. However, due to the difference in location of the participating parts, the logistics of the projects became somewhat of a conundrum. The cost of the difference in location of the two facilities was a lot of traveling on my behalf giving rise to a somewhat discontinuous ph.d. program.

I would like to thank Poul Lenvig Hansen and Stig Helveg for their constant encouragement over the years, even when I was in the USA. Their dedication has been an inspiration. I would also like to thank Prof. Dr. Abhaya K. Datye for his enthusiasm and his always objective views on data obtained both in Denmark and at the University of New Mexico. Thanks also to Jens Sehested for valuable discussions on the models, and to my supervisor Kenny Ståhl at the Technical University of Denmark.

During this project I have been in contact with numerous people, all of which I want to thank. Robin Christensen for help with the XRD data and Anna Carlsson for help with software and microscopy. Thanks also to the rest of the Materials Characterization Group and the rest of the Environmental and Materials Department at Haldor Topsøe for creating a friendly and stimulating working environment.

At the University of New Mexico I would like to thank the people in the Catalysis group, Ayman, Travis, Jaime, Mangesh, Hien, Hugo, Michael, Elise, Marcus, Ganesh, Andrew, David, and John, and the people in the CMEM office, Estelle, Maureen, Bill, and Michelle.

Haldor Topsøe A/S and industry members of the Ceramic and Composite Materials Center are greatly acknowledged for financial support.

Finally I would like to thank my dad without whom this project would never have been a reality.

Previous work

- Thomas W. Hansen, Jakob B. Wagner, Poul L. Hansen, Søren Dahl, Haldor Topsøe, and Claus J. H. Jacobsen:
  Atomic-Resolution in Situ Transmission Electron Microscopy of a Promoter of a Heterogeneous Catalyst
  Science **294**, 1508-1510, (2001)

- Thomas W. Hansen, Poul L. Hansen, Søren Dahl, and Claus J. H. Jacobsen
  Support effect and active sites on promoted ruthenium catalysts for ammonia synthesis
  Catalysis Letters **84**, 7-12, (2002)

- Michael Brorson, Thomas W. Hansen, and Claus J. H. Jacobsen
  Rhenium(IV) Sulfide Nanotubes
  Journal of the American Chemical Society **124**, 11582-11583, (2002)

- Anne Krogh, Anke Hagen, Thomas W. Hansen, Claus Hviid Christensen, and Iver Schmidt
  Re/HZSM-5: a new catalyst for ethane aromatization with improved stability
  Catalysis Communications **4**, 627-630, (2003)

Abstract

Sintering represents a significant route of deactivation of supported metal catalysts. Hence a fundamental understanding of the phenomenon is important when designing catalysts more resistant to deactivation by sintering.

The aim of this work is to elucidate the mechanism of sintering under simulated industrial conditions. The main focus is on studying the assumptions leading to the derivation of a model for sintering of industrial steam-reforming catalysts. The validity in extrapolation of the model to the low-pressure simulated steam-reforming environment used in the in situ transmission electron microscope (in situ TEM) experiments in this study is also investigated, thus establishing a link over a wide range of pressure.

In this thesis, the sintering of oxide supported metal particles were studied using in situ TEM and scanning electron microscopy.

For the in situ TEM studies, a nickel-based steam-reforming catalyst was studied under conditions relevant for the steam-reforming reaction. Three sets of experiments were carried out.

One set of experiments focused on the effect of atmosphere. The catalyst samples were treated in atmospheres with and without water vapor present at different temperatures. Particle diameters were measured at different instances and particle size distributions determined as a function of time.

The second set of experiments focused on the effect of time. The catalyst samples were sintered in the in situ microscope for a certain period of time and the particle size distributions and mean particle diameter determined before and after treatment. The idea of these first two experiments is to create a reference to later online experiments and to compare with predictions from a model derived from experiments carried out at in a reactor at ambient pressure.

In the third set of experiments the migration of the metal particles was monitored online. Samples were treated in different atmospheres and temperatures and particle migration was recorded as a function of particle size.

An analysis of the three sets of experiments showed agreement with the trends found in reactor experiments under industrial conditions for the change in the mean particle diameter. Deviation from classical models were in that the smallest particles did not migrate the longest distances as classical theory predicts. Instead particles around 8-10nm are most mobile and

coalesce with other particles during their migration. A population of small particles was present on the support surface even after 5 hours of sintering. This population did, however, decrease in number over the sintering period. The presence of small particles suggests that a large number of the particles do not themselves migrate and participate in the sintering only when absorbed by other particles. These small particles are somehow anchored to the support. The frequency with which metal particles were observed to sinter can account for the changes observed in the particle size distributions. Based on the observations, a model is proposed that includes one activation energy related to the release of particles from their anchoring sites and a second activation energy accounting for the migration of metal particles over the support.

A series of sintering experiments on flat model catalysts were carried out and studied in the scanning electron microscope. These studies were aimed at supporting the observations and the model derived from the in situ TEM experiments. As the experiments with flat model systems produce particle size distributions with better statistics, the shape of these can be derived more convincingly. Further the flat model substrates decreases the complexity of the industrial catalyst studied in the in situ TEM by removing a spatial dimension. These experiments also showed that the smallest particles may be anchored to the support while larger particles show signs of migration.

Dansk Resumé

Sintring repræsenterer en signifikant deaktiveringsmekanisme for katalysatorer bestående af metalpartikler dispergeret på oxidbæremateriale. For at udvikle katalysatorer, der er mere resistente over for sintring, er en fundamental forståelse af fænomenet vigtig.

Målet med dette studium er at undersøge mekanismerne bag sintring under simulerede industrielle betingelser. Fokus vil være på at undersøge de antagelser, der bruges til at udlede en model for sintring af industrielle steam-reforming katalysatorer. Desuden at undersøge validiteten af at ekstrapolere denne model til det lavtrykssimulerede steam-reforming miljø, der er brugt i in situ TEM forsøgene i dette studium og dermed skabe en forbindelse over et stort trykområde.

Denne afhandling omhandler sintring af metalpartikler på en oxidbærer studeret med in situ transmissionselektronmikroskopi og skanningelektronmikroskopi.

Til in situ studierne, blev en nikkelbaseret steam-reforming katalysator studeret ved betingelser relevant for steam-reforming processen. Tre forsøgsserier blev udført.

I den første serie studeredes effekten af atmosfæren. Katalysatorprøver blev behandlet i atmosfærer med eller uden vanddamp ved forskellige temperaturer. Partikelstørrelser blev målt på forskellige tidspunkter, og partikelstørrelsesfordelinger blev bestemt som funktion af tid.

Den anden forsøgsserie fokuserede på effekten af tid. Katalysatorprøver blev behandlet i in situ mikroskopet i en given periode, og partikelstørrelsesfordelinger og middeldiametre blev bestemt før og efter behandlingen. Ideen bag disse to forsøg er at lave en reference for senere online forsøg og at sammenligne med en model udledt fra forsøg foretaget ved højt tryk.

I den tredie forsøgsserie fulgtes migrationen af partikler online. Katalysatorprøverne blev behandlet under forskellige atmosfærer og temperaturer, og migration blev målt som funktion af partikelstørrelse.

Analysen af de tre forsøgsserier viste overensstemmelse med udviklingen af metalpartikeldiameteren for forsøg udført under industrielle betingelser. Afvigelse fra de klassiske modeller viste sig ved, at det ikke er de mindste partikler, der migrerer længst, som klassisk teori forudsiger. I stedet viste det sig, at partikler omkring 8-10nm er mest mobile og sammensmelter med

andre partikler, de møder under deres migration. Der findes en bestand af små partikler på bæremateriale selv efter 5 timers sintring. Denne bestand falder dog i antal over sintringsperioden. Tilstedeværelsen af små partikler vidner om, at en stor del af partiklerne ikke selv migrerer, men kun deltager i sintringen ved at blive absorberet af andre partikler. Disse små partikler er ankret til supportmaterialet. Frekvensen, hvormed sintringsbegivenheder observeredes, kan redegøre for ændringen i partikelstørrelsesfordelingerne. En model er foreslået baseret på disse observationer, som inkluderer en aktiveringsenergi for at løsrive partikler fra deres forankringspunkt på bæremateriale og en aktiveringsenergi for migration over bæremateriale.

En forsøgsserie på flade modelkatalysatorer blev udført og studeret med skanningelektronmikroskopi. Disse forsøg blev gennemført med henblik på at understøtte modellen udledt fra in situ TEM studierne. Da forsøgene med flade modelsystemer producerer partikelstørrelsesfordelinger med bedre statistik, kan formen af fordelingerne bestemmes mere overbevisende. Desuden fjerner de flade bæremateriale noget af kompleksiteten af det industrielle bæremateriale ved at eliminere en dimension. Disse forsøg viste også, at små partikler kan være fikseret til bæreren, mens større partikler migrerer.

Contents

List of Figures

List of Tables

List of Symbols

a	-	atomic diameter
a_0	-	atomic diameter of metal, Bohr radius
A	-	amplitude, surface area per gram catalyst
$\mathbf{B}$	-	Magnetic field strength
c_{car}	-	number of particles per support surface area
c_{cat}	-	number of particle per gram catalyst
c_d, c_i	-	normalizing constant
C	-	constant
C_c	-	chromatic aberration coefficient
C_s	-	spherical aberration coefficient
d	-	particle diameter
$\bar{d}_0$	-	initial mean particle diameter
$\bar{d}$	-	average particle diameter
$\tilde{d}$	-	particle diameter normalized to mean particle diameter
D	-	dispersion
D_{eq}	-	
D_s	-	surface diffusion coefficient
D_0	-	constant, initial dispersion
D_p	-	particle diffusion coefficient
e	-	electron charge
E	-	
$\mathbf{E}$	-	electric field strength
f_{L-N}	-	log-normal function
$\mathbf{F}$	-	Lorentz force
$\mathcal{F}$	-	Fourier transform
g	-	ratio of facet diameter to particle radius
h	-	Planck constant
H_e	-	binding energy at cluster edge
H_s	-	binding energy on support
$H_{m,s}$	-	energy barrier for migration on support
H_c	-	binding energy on cluster
$H_{m,c}$	-	energy barrier for migration on cluster
I	-	intensity

k	-	
k	-	thermal conductivity
k_s	-	sintering rate constant
K_n	-	equilibrium constant
m	-	electron mass
m	-	sintering order in the generalized power law model
n	-	sintering order
N_0	-	number of surface sites
P	-	objective aperture function
P	-	pressure
q	-	magnitude of scattering vector
$\mathbf{q}$	-	scattering vector
Q	-	activation energy
r	-	radius of curvature
r_R	-	Rayleigh resolution
r_{sch}	-	resolution at scherzer defocus
r_{sph}	-	radius
R	-	
R_0	-	initial unperturbed particle radius
S	-	surface area
t	-	time
t_d, t_i	-	characteristic time
T	-	temperature
$\mathbf{v}$	-	velocity
V	-	volume
w	-	width of log-normal function
x_c	-	center of log-normal peak
X	-	metal loading
X_c	-	particle displacement
y_0	-	offset
Z	-	atomic number
α_s	-	jump length
β	-	collection semiangle
γ	-	relativistic factor
γ_s	-	surface energy of support
γ_{ms}	-	surface energy of metal-support interface
γ_m	-	surface energy of metal
γ_e	-	edge energy
γ_0	-	
δ	-	secondary electron coefficient
ΔF_{sch}	-	Scherzer defocus
η	-	backscatter electron coefficient
θ	-	coverage

θ	-	contact angle
λ	-	wavelength
μ	-	refractive index, chemical potential
μ_0	-	chemical potential of infinitely large particle
$\rho(E)$	-	density of electronic states
ρ	-	density of metal
σ	-	
τ	-	sintering time
ϕ_p	-	projected specimen potential
ϕ_d, ϕ_i	-	distribution function
Φ	-	collision rate per gram catalyst
Φ_j	-	collision rate of particles with diameter d_j
χ	-	contrast transfer function
ψ_i	-	complex image amplitude, initial state
ψ_f	-	final state
ψ_e	-	exit wave amplitude
Ω	-	atomic volume

Chapter 1

Introduction

Industrial catalysts often consist of metal nano-particles dispersed on an oxidic support material. Keeping the particles small is of major importance since the small particles provide a high metal surface area available for catalytic reactions. However, under industrial conditions, some of the nano-particles tend to grow in size while others vanish resulting in a decrease of total catalytically active surface area. This process is known as *sintering* and represent one of the major deactivation mechanisms of supported metal catalysts.

Recent advances in analytical techniques such as electron microscopies enable us to obtain further insight into the mechanisms of metal particle sintering. Earlier, the phenomenon has been studied using electron microscopy under vacuum conditions, but early versions of in situ transmission electron microscopy have also been used to study sintering.

A recent model for sintering of nickel-based steam-reforming catalysts predicts the evolution of the mean metal particle diameter as a function of atmosphere and time. The assumptions for this model allow for its extrapolation to the pressure regime used in the in situ TEM, thus establishing a link between reactor experiments and in situ TEM observations. This link, however has to be validated which is the main purpose of this work.

This work on sintering of supported metal catalysts is the result of a collaboration between Haldor Topsøe A/S and the University of New Mexico (UNM). The problem has been approached from two very different angles. At Haldor Topsøe A/S an in situ TEM was used and at UNM a high resolution scanning electron microscope.

At Haldor Topsøe A/S, the in situ transmission electron microscope, CM-300 FEG in situ from FEI company, was used to provide direct evidence for the sintering of metal particles. The in situ TEM seems the ideal instrument for analyzing sintering, however over a limited time scale. It is a good way of locally probing the sample online while it is exposed to a reactive environment. However, while the in situ TEM represents a major leap forward

in studying catalysts, there is still a major difference between the conditions in the in situ TEM and those found in industrial reactors. The in situ TEM operates in the millibar regime compared to the 100's of bars often found in industrial reactors. Introducing gases over the samples also decreases the image quality and increases the surface contamination of the metal particles. In situ TEM studies only give very local information and do not provide observations of sintering particles over a large area covering numerous particles. Further the influence of the electron beam in the microscope is still poorly understood.

The initial studies at Haldor Topsøe A/S were aimed at finding samples suitable for sintering studies, i.e. samples where sintering was observed at a time scale of hours suitable for in situ microscopy studies, and where the reactor environment could be mimicked in the in situ TEM. A strange task since scientist have been trying to prevent this for decades. At the same time the system of choice had to have some industrial relevance to make it feasible to conduct a 1.5 year study. The nickel on magnesium aluminum spinel represented a system of industrial importance in the steam-reforming process. A large body of literature was available on nickel-based steam reforming and detailed model was also available, resulting in the choice of this system.

While the in situ TEM gives local high resolution information on the sintering events as they happen, the technique only probes a limited area of the catalyst sample, and statistics are inherently limited using the technique. To substantiate the observations, a complimentary technique has been used.

In New Mexico, a newly installed high resolution scanning electron microscope was used to conduct sintering experiments with good statistics. The high-resolution scanning electron microscopy facility made it possible to detect metal particles of sizes relevant to catalysis. However these studies have to be carried out ex situ, i.e. samples have to treated in a facility external to the microscope and analyzed under high vacuum conditions.

The studies at the University of New Mexico were conducted using flat model systems. For such systems the metal particles were more easily observable and much of the complexity of the industrial catalyst is removed. The flat model substrates are more stable under the reaction conditions than the porous industrial support material providing more uniform conditions for the metal particles. Hence better statistics could be achieved on such samples and the observations from the in situ TEM experiments could be substantiated. As other systems than the Ni-based steam-reforming catalyst were investigated in the SEM, the universality of the model could be tested. The downside of the model system is that it does not contain the porous system of the commercial catalyst. Hence recondensation after evaporation, if it occurs, will most likely not take place. Also as the scanning electron microscope is not an in situ facility, the sample has to be transferred.

A goal of this work has been to relate the observations done in the mi-

croscopes to an existing model. Further, to determine the assumptions of the previous work, i.e. the Gruber model described in Chapter 4 and to explain the observed evolution of the particle size distributions by the events observed in the microscopes.

Overview of the Thesis

Chapter 2 gives a general and very basic introduction to catalysis and some of the challenges that face scientists working in this field and some of the accomplishments concerning sintering.

In Chapter 3 the experimental equipment used in investigating the sintering phenomenon is described. Detailed accounts of the microscopes are given together with a description of their optimal use. Also the strength and weaknesses of the techniques used are outlined.

Chapter 4 introduces the theory of sintering, from the mechanisms to some of the models used to explain sintering.

Chapter 5 takes the reader through the experiments and results obtained using the in situ transmission electron microscope. Data from three sets of experiments are presented. The first set deals with the rate of sintering as a function of atmosphere and temperature. Set two is sintering of catalysts over a 5 hour period without exposure to the electron beam, just using the in situ microscope as a reactor. The last set of experiments is an online observation of the sintering of the catalyst as it is exposed to a catalytically relevant environment. The chapter is concluded with considerations for a model explaining the observations of all three experiments.

Chapter 6 deals with the results obtained in New Mexico with the scanning electron microscope. These data are interpreted in terms of the model proposed in Chapter 5 derived from the observations done at Haldor Topsøe A/S.

Finally Chapter 7 sums up all the results and tries to put it all in perspective.

Chapter 2

Heterogeneous Catalysis

2.1 Catalysis

Chemical industry is the largest industry in the world today. Without chemical industry we would not be able to sustain the lives we are living today or uphold the population of the earth. The chemical production index has increased in almost all countries in the western world [1], and is not likely to decrease anytime soon.

Catalysis and catalytic processes play a major role in the chemical industry of industrialized countries today. 85-90% of chemicals produced involve catalytic processes [2]. The total value of fuel and chemicals derived from catalyzed processes was estimated to 17% of the GNP of the United States in 1989 amounting to $891 billion. Worldwide the value added from catalysis is about $3 trillion [3].

Much effort is put into research in catalysis from both private companies and universities all over the world, both in engineering new catalysts and in improving on existing catalysts. Catalysts are so much more than the automotive exhaust converter found in all modern cars. Organic products such as ethylene, methanol, and propylene, and inorganic products like ammonia, hydrogen and sulfuric acid are all produced in catalytic processes. Catalysis not only helps us in production. The diversity of catalysts is illustrated by the use of catalysts on the environmental protection side. Catalysts are used for limiting pollution from nitrous oxides, sulfuric oxides, and un-converted hydrocarbons from power plants and automobile exhausts. Catalysts are also involved in upgrading the value of fossil fuels by removing nitrogen, sulfur and impurity metals from crude oil.

The term *catalysis* was first used by the Swedish scientist Jøns Jacob Berzelius in 1836 and further defined by Wilhelm Ostwald:

> *A catalysts is a substance that accelerates the rate of a chemical reaction without being part of its final products.*

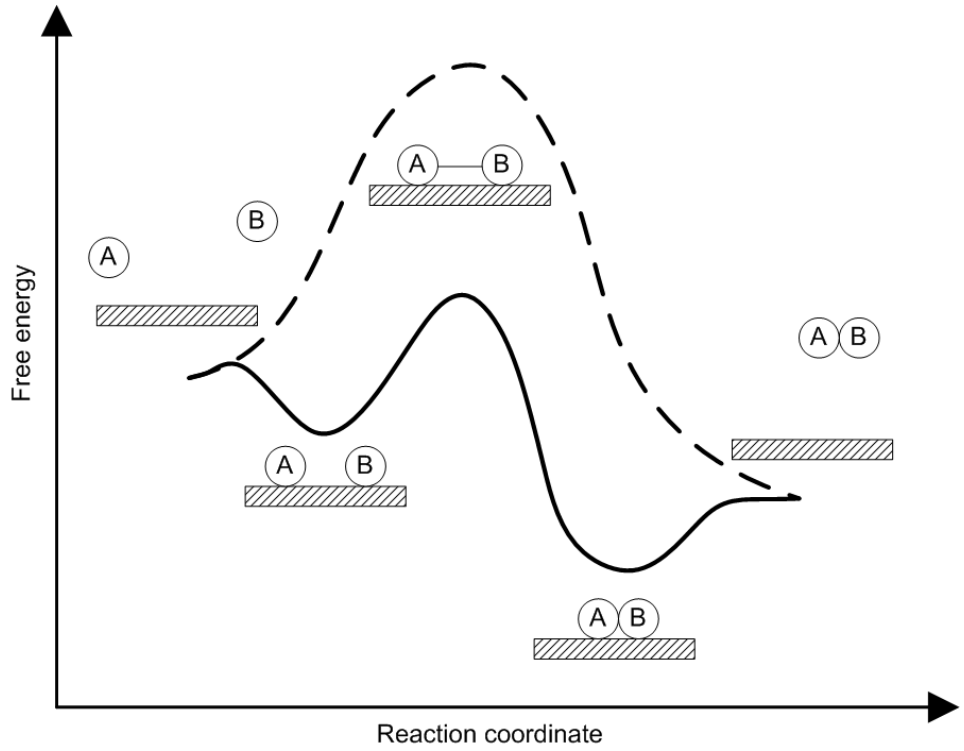

Figure 2.1: Simplified energy diagram for a catalyzed (solid line) and a non-catalyzed reaction (dashed line). The catalyst provides a reaction pathway with a lower energy barrier.

The word comes from the Greek *katalysi* which is a combination of *kato* meaning down and *lyo* meaning to break. This word was chosen as all the first identified catalyzed reactions were decomposition processes.

The purpose of a catalyst is to accelerate a reaction. Reactants are bonded to the catalyst and are allowed to react to form products. After reaction the products detach from the catalyst surface and a new cycle can begin. Hence the atoms in the reactants are the same as in the products and the catalyst is left unchanged after the reaction. Fig. 2.1 shows a simplified energy diagram for a chemical reaction. Without the catalyst, the dashed line, the energy barrier going from reactants to products is large. The catalyst provides a lower energy pathway for the reaction, the solid line. Reactant molecules adsorb on the surface of the catalyst lowering their potential energy, a bond is formed between the reactants and the product is formed. Last, the product is released from the unchanged catalyst surface and the catalyst is ready for the next cycle. The number of reactant molecules reacted per active site per second is known as the turn-over frequency.

Catalysts can take many shapes. Often the catalyst material is pressed

into pellets with dimensions from mm to cm. Catalysts can also be monoliths where the active phases are present on the surface of the monolith. Such systems are often used in the catalytic converters in automobiles and for gas cleaning in power plants.

The catalyst used in this study is a supported catalyst. The supported catalyst consists of metal nanoparticles dispersed on a support, often an oxide. The smaller the particles the higher the relative active surface area. The main purpose of the support is to stabilize the metal particles and maintain a high degree of catalytically active metal surface area.

2.2 Steam Reforming Catalysis

Steam reforming is the term used for converting hydrocarbons into a mixture of carbon monoxide, carbon dioxide, and hydrogen, this mixture is known as *syngas*, short for synthesis gas. The basic reactions in steam reforming are [4]

$$\mathrm{C}_n\mathrm{H}_m + n\mathrm{H_2O} \rightarrow n\mathrm{CO} + \left(n + \frac{m}{2}\right)\mathrm{H}_2 \quad -\Delta H^0_{298} < 0 \tag{2.1}$$

$$\mathrm{CO} + \mathrm{H_2O} \rightleftharpoons \mathrm{CO_2} + \mathrm{H_2} \quad -\Delta H^0_{298} = 41.2 kJmol^{-1} \tag{2.2}$$

$$\mathrm{CO} + 3\mathrm{H_2} \rightleftharpoons \mathrm{CH_4} + \mathrm{H_2O} \quad -\Delta H^0_{298} = 206.2 kJmol^{-1}. \tag{2.3}$$

Eqn. 2.2 is also known as the water-gas shift reaction. The most common feedstock for the steam-reforming process is natural gas consisting mainly of CH_4 or naphta (light petroleum distillate) [5].

The steam-reforming process was developed in the beginning of the 20th century to produce hydrogen for ammonia plants. Later on the process was used as hydrogen was needed to synthesize liquid fuels in the Fischer-Tropsch process. Steam reforming is also used in other processes such as methanol synthesis where syngas is converted to methanol over a copper/zinc oxide catalyst and for hydrotreating processes in refineries. Tables 2.1 and 2.2 show the production of hydrogen and ammonia, processes where steam reforming/syngas is used. The numbers in the table show the significance of the process.

Many late transition metals are active in the steam-reforming reaction. Pd, Pt, Ru, Rh, Ir, Fe, and Co can be used, but are either economically not feasible or they oxidize under reaction conditions. Most often a steam reforming catalyst consists of nickel supported on either alumina (Al_2O_3) or magnesium aluminum spinel ($MgAl_2O_4$).

Recently the energetics of the individual steps of the steam-reforming process were calculated by Bengaard [8]. The elementary steps of the steam reforming reaction are

	1997	1998	1999	2000	2001	2002	2003	2004
Europe	1883	2124	2252	2196	5553	7519	8962	4511[1]
USA	14895	15631	12856	13139	13451	13564	14385	17698[2]

Table 2.1: Hydrogen production in Europe, USA over the last eight years [1]. [1]Germany, France and U.K. only, [2]preliminary data. Data in thousands of metric tons.

	1995	1998	2000	2001	2002	2003	2004
World	95000	104000	108000	105000	109000	110000	170000

Table 2.2: Worldwide ammonia production over the last 10 years [6, 7].Data in thousands of metric tons.

$$\mathrm{CH_4} + 2* \rightleftharpoons *\mathrm{CH_3} + *\mathrm{H} \quad (2.4)$$
$$*\mathrm{CH_3} + * \rightleftharpoons *\mathrm{CH_2} + *\mathrm{H} \quad (2.5)$$
$$*\mathrm{CH_2} + * \rightleftharpoons *\mathrm{CH} + *\mathrm{H} \quad (2.6)$$
$$*\mathrm{CH} + * \rightleftharpoons *\mathrm{C} + *\mathrm{H} \quad (2.7)$$
$$\mathrm{H_2O} + 2* \rightleftharpoons *\mathrm{H} + *\mathrm{OH} \quad (2.8)$$
$$*\mathrm{OH} + * \rightleftharpoons *\mathrm{O} + *\mathrm{H} \quad (2.9)$$
$$*\mathrm{C} + *\mathrm{O} \rightleftharpoons *\mathrm{CO} + * \quad (2.10)$$
$$*\mathrm{CO} \rightleftharpoons \mathrm{CO} + * \quad (2.11)$$
$$2 * \mathrm{H} \rightleftharpoons \mathrm{H_2} + 2* \quad (2.12)$$

where * represents a surface site. Fig. 2.2 shows the energy diagram of the stable intermediate species relative to CH_4 and H_2O in the gas phase on steps and on a perfect terrace. The steps have been modeled by a (211) facet and the perfect terrace by a close-packed (111) facet. The figure shows that steps are more active for CH_4 decomposition and C bonding as the energy on the step is always below that on the terrace. This is a generally observed trend for catalysts, e.g. in the case of ammonia synthesis over a ruthenium catalyst. On the ruthenium catalyst, five-fold coordinated B_5 type sites are believed to be the most active for the decomposition of di-nitrogen which is the rate limiting step in ammonia synthesis [9, 10]. Reaction 2.8 plays a vital role in the Sehested model described in Chapter 4. The detailed insight into the reaction mechanism as shown by Fig. 2.2, was provided by an interplay between several techniques. In this case thermogravimetric analysis (TGA) and extended x-ray absorption fine structure (EXAFS) on the experimental side and density functional theory and Monte Carlo simulations

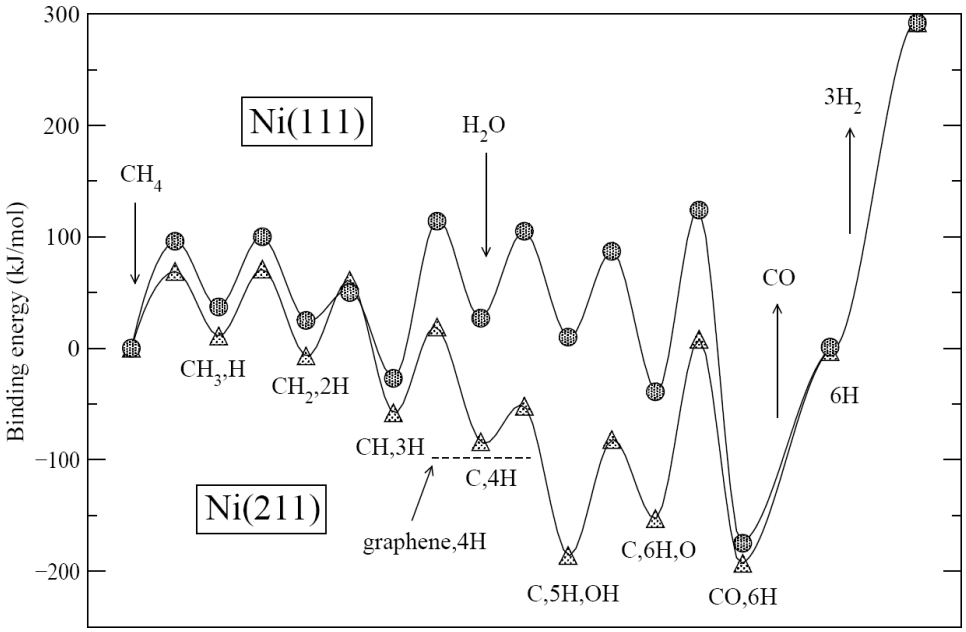

Figure 2.2: Potential energies of the stable intermediate CH_x species on the (211) and the (111) surfaces of nickel [8, 12].

on the theoretical side [8], provided details about the individual steps of the steam reforming reaction. This in turn, lead to the formulation of the model described by Sehested *et al.* [11].

Typically a steam reformer consists of arrays of vertical tubes loaded with catalyst pellets. The reactor tubes are typical 70-160mm in diameter and made from high alloy nickel chromium steel. A steam reforming reformer may contain as many as 400 tubes. Usually the tubes are heated externally to the operating temperatures which can be as high as 1300K.

Even though the nickel-based steam-reforming catalyst is very robust, it still faces challenges. Carbon formation and sulfur contamination are among the worst deactivation processes. Carbon filaments are formed mainly when the oxidation potential decreases, i.e. when the H_2O:C ratio decreases [8]. The filaments can disintegrate the catalyst pellets and the catalyst becomes inactive. When no heat is removed by the reaction, the reactor tubes become hot and melt due to the external heating. Sulfur contamination is the result of sulfur compounds in the feedstock. Sulfur adsorbs on the active sites of the catalyst and blocks them from the reactants resulting in reduced catalytic activity. Sulfur contamination is probably the most severe deactivation mechanism of nickel-based steam-reforming catalysts. A third deactivation mechanism for the catalyst is metal sintering. When the reformer is operated at high temperatures, the nickel becomes mobile resulting in the growth of metal particles. The driving force behind the growth is the minimization

of the surface energy of the metal particles as described in Chapter 4. The main problem in the growth can be summarized as

$$\frac{S}{V} \propto \frac{1}{d}. \tag{2.13}$$

The volume, V, of active metal in the catalyst is constant. Thus the optimal catalytically active surface area, S, is obtained by minimizing the particle diameter, d. As the particles grow, active metal surface area is lost and the number of active sites decreases and the catalyst looses activity.

In general, one of the challenges in producing a highly active catalyst is to deposit the metal on the support in small particles to achieve the highest possible metal surface area from as small as possible an amount of metal and having the particles remain stable. As the prices for many of the metals used in catalysis is increasing researchers are trying to optimize the surface area to volume ratio.

Chapter 3

Electron Microscopy

A vast amount of experimental techniques have been used for studying heterogeneous catalysts. For obtaining direct local information, a method like electron microscopy is needed. However, microscopy techniques that have provided sufficient resolution (TEM, STM) have all operated in high or ultra high vacuum (UHV). UHV instruments are great for obtaining atomic information and the big advantage is that surfaces are easier to keep free of contaminants. Samples can be treated in a reactor setup and transferred inertly to a microscopy facility for observations. Techniques that can operate *in situ*, like XRD or EXAFS, while great for obtaining average values quick, do not provide direct information on individual catalyst particles like the local information obtained from microscopies. The advent of *in situ* electron microscopy added the aspect of exposing the samples to reactive environments while observing the evolution in the sample. However as of yet, *in situ* transmission electron microscopes operate at reduced pressures compared to samples treated in microreactors. This gap is known as *the pressure gap*. Also there are limitations to the duration of experiments. For a review of recent achievements in catalysis using electron microscopy, see [13].

3.1 Electron Microscopy

In microscopy, the resolution of the instrument is a function of the wavelength of the probing entities. In an optical microscope the probing entities are photons, thus resolution of an optical microscope is limited by the wavelength of the photons used, in the case of visible light the wavelength is λ=400-700nm. The resolution, r_R, can be determined by the Rayleigh formula [14]

$$r_R = \frac{0.61\lambda}{\mu \sin \beta} \tag{3.1}$$

where μ is the refractive index of the viewing medium and β is the semiangle of collection. By decreasing the wavelength, λ, the resolution of a microscope

can be improved, at least in theory, infinitely. However, problems arise for the focusing of high-energy photons like x-rays. By using electrons instead of photons, the probing entities are charged particles which can be accelerated to high energies and short wavelengths and focused using electro-magnets. Typical wavelengths encountered in a transmission electron microscope are 0.00251nm for a 200kV instrument and 0.00197nm for a 300kV instrument.

3.2 Transmission Electron Microscopy

The transmission electron microscope, *TEM*, has since its invention in 1932 by Knoll and Ruska, been an important instrument for studies of catalysts. A transmission electron microscope is in many ways analogous to an optical microscope, the main difference being that electrons are used in stead of photons. A sample is illuminated by a broad beam of electrons, which after passage of the sample are projected into a two-dimensional image. This is where the similarities to optical microscopes stop. The lenses in the electron microscope are electromagnetic, hence it is possible to adjust their strength by changing the current through the coils without moving them as in an optical microscope. The complex lens system in an electron microscope is susceptible to many kinds of deterioration of the image quality. Even slight vibrations in the vicinity of the microscope can decrease the resolution and the quality of the images. Variations in the power sources give rise to changes in the lens strengths and decrease the microscope resolution. Often electron microscopes are placed in an isolated room or on dampened platforms to minimize the influence of external sources to optimize the resolution and performance.

To obtain the highest possible resolution, coherent and monochromatic electron sources are used. The word monochromatic is adopted from optical microscopy and describes the energy spread of the electrons emanating from the source. In the first electron microscopes, tungsten filaments were used as electron emitters, later LaB_6 was used as emitters due to higher brightness and smaller energy spread [14,15]. Over the last decade field emission sources have become more common and are now the defacto standard for high resolution electron microscopy, both in scanning electron microscopy [15] as described in Section 3.3 and in transmission electron microscopy [14]. The main advantage of the field emission gun is the small energy spread of the electrons and the high brightness compared to tungsten and LaB_6 type filaments. The major drawback of using field emission guns, or *FEG's*, is that they are very sensitive to the operating conditions and require UHV conditions. Hence even minor failures in the vacuum system can cause long periods of inoperability of the electron microscope. However an FEG emitter is a good starting point if lattices in catalytically interesting metals like Ni and Cu are to be resolved [16].

In an electromagnetic lens, a magnetic field is produced by a current running through a coil in the lens. Thus the strength of the magnetic field can be controlled by changing the current through the coil. The variable field strength is a major advantage over optical lenses.

When the electrons pass through the electromagnetic lens, they experience a force, $\mathbf{F}$, determined by

$$\mathbf{F} = -e(\mathbf{E} + \mathbf{v} \times \mathbf{B}) \tag{3.2}$$

known as the Lorentz force. Here $\mathbf{E}$ is the electric field strength, $\mathbf{B}$ is the magnetic field strength, $\mathbf{v}$ is the velocity of the electrons and e is the electron charge. Unfortunately the magnetic field in the electromagnetic lens is not uniform. The result of the inhomogeneity is that electrons entering the lens at different angles are acted on differently as shown in Fig. 3.1. The result is that a single point, P, is projected into a disk of finite diameter at P'. This effect is known as *spherical aberration* and is the main factor influencing the resolution of the instrument. The minimum radius of the disk, known as *the disk of least confusion*, is given by

$$r_{sph} = C_s \beta^3 \tag{3.3}$$

where C_s is known as the *spherical aberration coefficient* and β is the collection semiangle, see Fig. 3.1.

Fig. 3.2 shows one of the transmission electron microscopes installed at Haldor Topsøe A/S (HTAS) in Lyngby, Denmark. The vertical column houses the electron source, the sample, and the electron optical system for forming images. The column is ca. 1.5m high from the top, at the electron source, to the bottom, at the viewing screen. The microscope is equipped with a gas inlet system and differential pumping described in Section 3.2.2.

A transmission electron microscope can project two different images onto the viewing screen. A diffraction pattern which is an image of the focal plane of the objective lens, the plane of the objective aperture in Fig. 3.3. This can also be considered as an image in reciprocal space. The microscope can also project an image in direct space onto the viewing screen. The ray trace of the electrons in the two different modes are shown schematically in Fig. 3.3. As shown in the figure, switching between diffraction mode and imaging mode is done by changing the strength of the intermediate lens.

Three distinct kinds of contrast are observed in the TEM: 1) mass-thickness, 2) diffraction contrast, and 3) phase contrast. Mass-thickness contrast is a result of incoherent scattering of electrons, or Rutherford scattering. The incoherent scattering is a function of the atomic number Z and the thickness of the sample. Hence, denser regions or regions containing heavier elements, scatter the electron beam stronger, as illustrated in Fig. 3.4. The electron beam coming from denser or heavier regions will thus appear darker in the image while electrons emanating from the lighter or less

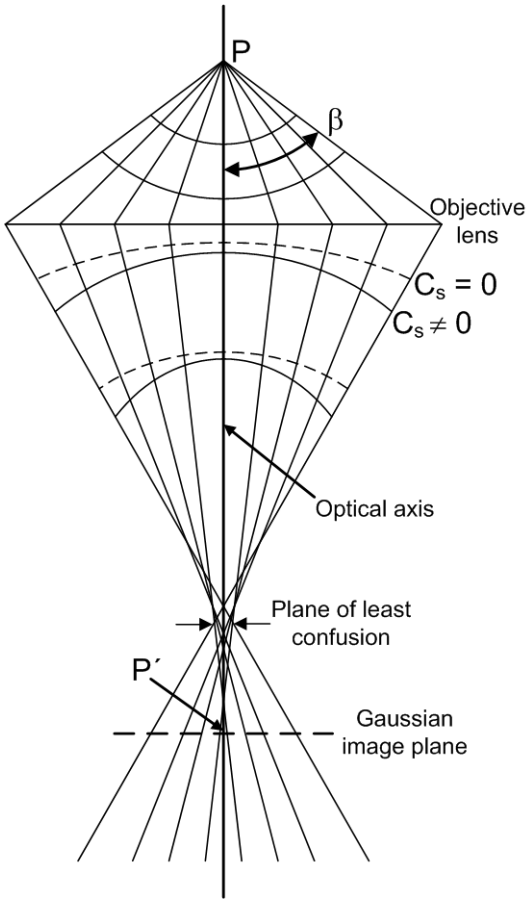

Figure 3.1: Electron ray paths through the objective lens. Electrons entering the lens at a high angle are focused at a different point than electron entering the lens at a low angle resulting in a point P being imaged as a disk at P'. The wave front is shown for different values of the spherical aberration coefficient, C_s.

dense regions will appear bright in the image. By varying the size of the objective aperture the operator can determine which electrons are included in the image and hence enhance the mass-thickness contrast.

Diffraction contrast is a result of coherent Bragg scattering of the incoming electrons by the lattice planes. Each set of lattice planes scatters the incoming electrons to specific angles determined by the crystal structure. Hence, by moving the position of the aperture so it is centered around a certain diffracted beam, images of a specific set of planes can be formed.

Phase contrast is used to form lattice fringe images where the atomic lattice of the sample is resolved in the image. It is a result of phase differences of the electrons scattered through the sample. From phase contrast

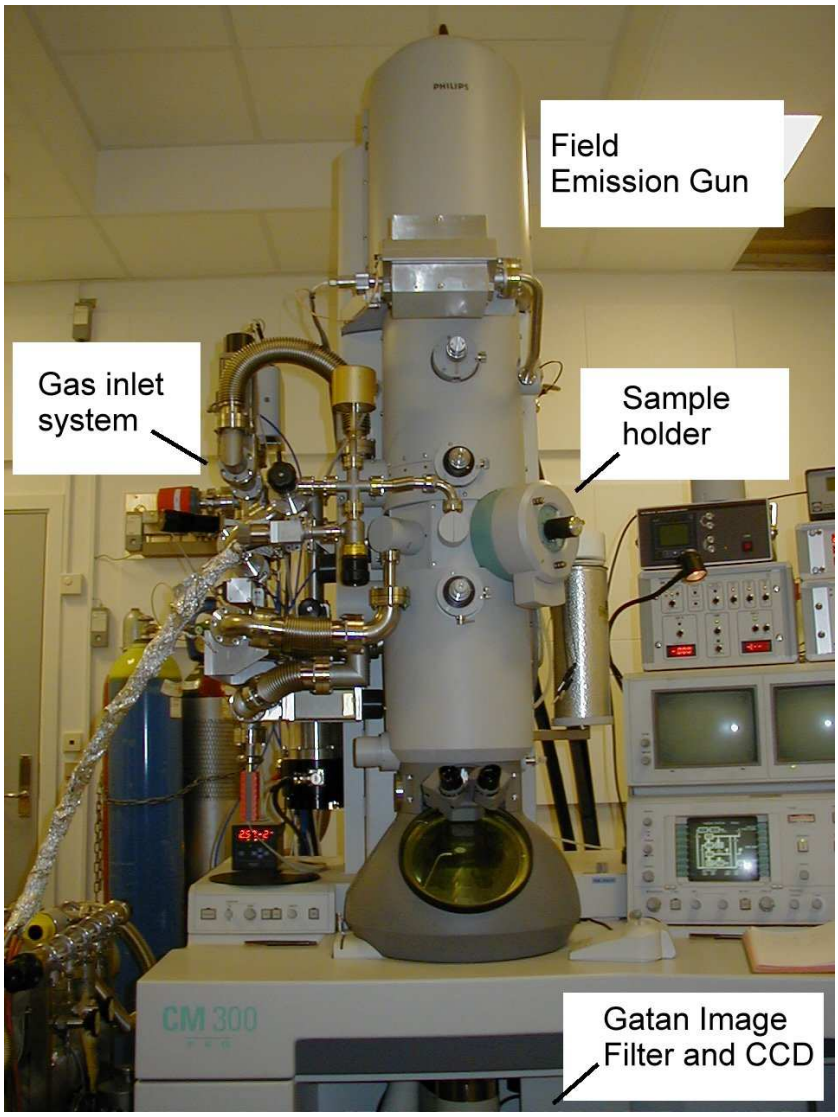

Figure 3.2: Philips CM-300FEG *in situ* TEM. The microscope installed at HTAS.

images the plane spacing and the angle between planes can be determined giving information of the detailed atomic configuration of the sample. For thin specimens consisting of low or medium weight molecules and neglecting Fresnel diffraction within the specimen, the complex exit wave, ψ_e, can be written as

$$\psi_e(x, y) = \exp(-i\sigma\phi_p(x, y)) \tag{3.4}$$

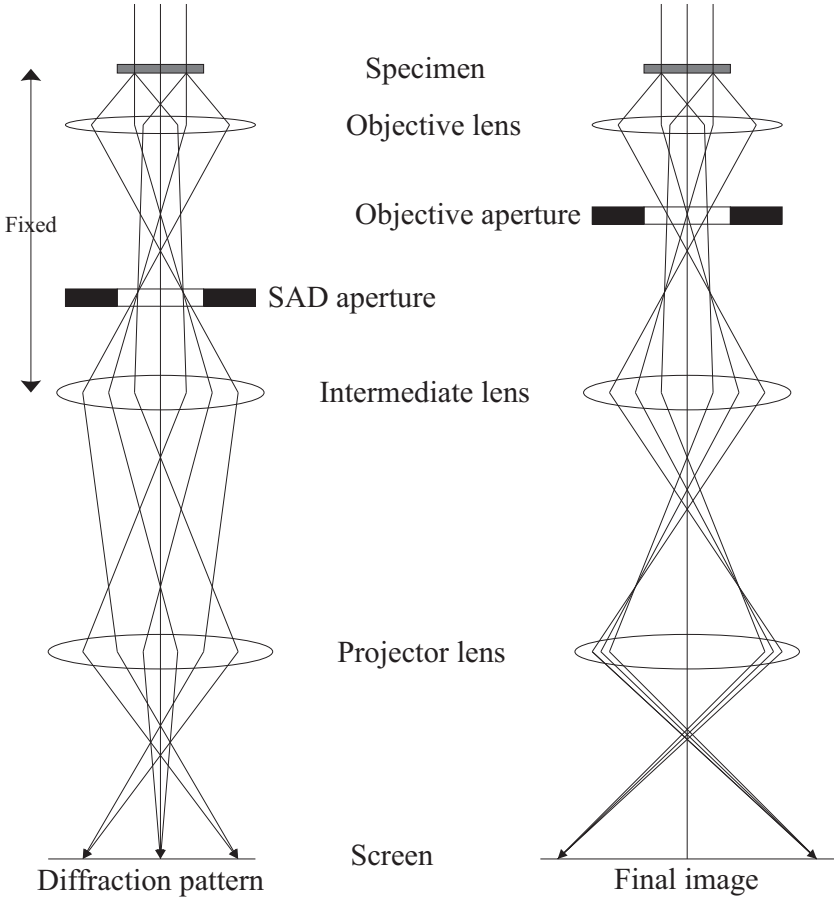

Figure 3.3: Trace of the electrons in a transmission electron microscope as they pass through the column. The left sketch shows the ray trace when the microscope is in diffraction mode and the right image when it is in image mode [17].

with

$$\sigma = \frac{2\pi m e \lambda}{h^2} \tag{3.5}$$

where ϕ_p is the projected specimen potential, m is the electron mass, e the electron charge and h the Planck constant. Approximating the exponential function to first order is known as the *weak phase approximation*. This approximation is valid for specimens of thickness smaller than $\sim 0.5nm$. For thicker more practical samples the *multislice model* can be used. Here the weak phase approximation is used for thin slices of the sample. Introducing the contrast transfer function, χ, as described below, the complex image amplitude, ψ_i, becomes

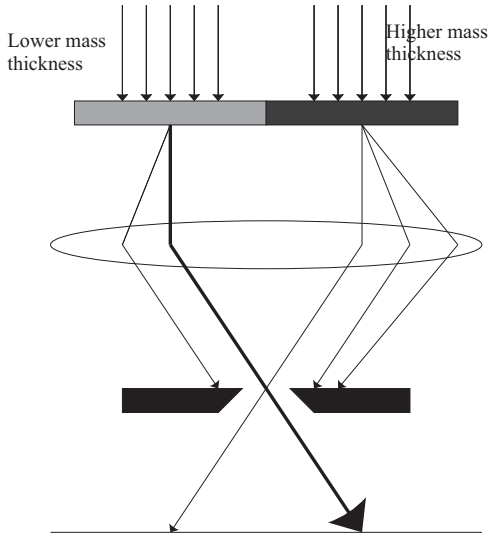

Figure 3.4: Sketch of mass-thickness contrast. The denser regions diffract the primary electron beam stronger (shown by light arrows) than the lighter regions (shown by a dense arrow). Hence the dense regions appear dark in the images while the light regions appear bright [17].

$$\psi_i(x,y) = 1 - i\sigma\phi_p(-x,-y) * \mathcal{F}[\exp i\chi(u,v)P(u,v)] \tag{3.6}$$

and the image intensity is given as

$$I = \psi_i(x,y)\psi_i^*(x,y) \approx 1 + 2\sigma\phi_p(-x,-y) * \mathcal{F}[\sin\chi(u,v)P(u,v)] \tag{3.7}$$

where (u,v) are coordinates in the back focal plane, the plane of the objective aperture in Fig. 3.3, (x,y) coordinates in the image plane, $P(x,y)$ is the objective aperture function [1], $*$ denotes convolution, $\mathcal{F}$ Fourier transformation, and χ is the contrast transfer function, or CTF [18]. The contrast transfer function describes the performance of the imaging optics of the transmission electron microscope. It is determined largely by three different parameters: 1) the energy of the electrons, 2) the monochromaticity of the electron source, and 3) the quality of the electron lens measured as the spherical aberration coefficient and the chromatic aberration coefficient. Fig. 3.5 shows a one-dimensional projection of the CTF of the Philips CM-300 in situ microscope [2]. The dampening of the CTF is caused by the temporal and spatial envelopes. The temporal envelope is due to chromatic aberrations, focal and

[1] $P(x,y)$=1 in the opening of the aperture, 0 elsewhere.

[2] The CTF was drawn using CTFExplorer by Max V. Sidorov (www.maxsidorov.com/ctfexplorer).

energy spread, instabilities in the high tension and lens current. The spatial envelope is due to finite convergence of the incident electron beam. In terms of the CTF, the point resolution is defined as the first crossover at $\Delta f =$ Scherzer defocus (described below). The information limit is the minimum distance that can be transferred from the sample to the image. For the CM-300, these two values are 0.20nm and 0.14nm respectively. The sign of the CTF shows whether atoms will appear bright or dark in the image. If the CTF is positive, atoms will appear bright on a dark background, when it is negative, atoms will appear dark on a bright background. Hence one has to be careful when interpreting contrast in images with resolution between the point resolution and the information limit.

From Fig. 3.5 it is observed that the contrast transfer function contains zeros. The optimal contrast transfer function is the one with the fewest zeros and a constant value of the contrast transfer function over a broad region. This is obtained at a special value of the microscope defocus called the *Scherzer defocus*

$$\Delta f_{sch} = -1.2\sqrt{C_s\lambda}. \tag{3.8}$$

The contrast transfer function drawn in Fig. 3.5 is drawn at Scherzer defocus. The point resolution in phase microscopy is determined by the first crossover of the contrast transfer function as indicated on the figure and given by

$$r_{sch} = 0.66(C_s\lambda^3)^{1/4} \tag{3.9}$$

The experimental resolution of the transmission electron microscope can be determined using a Young fringe experiment. For this test, a sample that diffracts at several angles is needed, usually a grid with crystalline gold particles on an amorphous carbon support film is used. An image is recorded with the specimen shifted through a distance d during acquisition [14]. Thus every feature in the sample appears twice in the transmitted beam giving rise to Young's interference fringes in the Fourier transform of the image with a spacing $\Delta q = 1/d$. The Young's fringes are visible to the information limit of the microscope as shown in Fig. 3.6. The Young fringes are visible to Δq corresponding to ca. 0.14nm. The image for the resolution test was acquired in 5mbar nitrogen at room temperature. Reflections corresponding to 0.12nm are also observed, but are not found symmetrically around the Fourier transform. This can be due to electrical fields near the microscope or mechanical vibrations of the sample.

To ensure that the distances measured in the TEM micrographs are correct, the magnification can be calibrated using known standards. In most cases gold particles dispersed on an amorphous carbon film are used for this purpose. With a (111) lattice spacing of 0.24nm, gold is well-suited for TEM calibration.

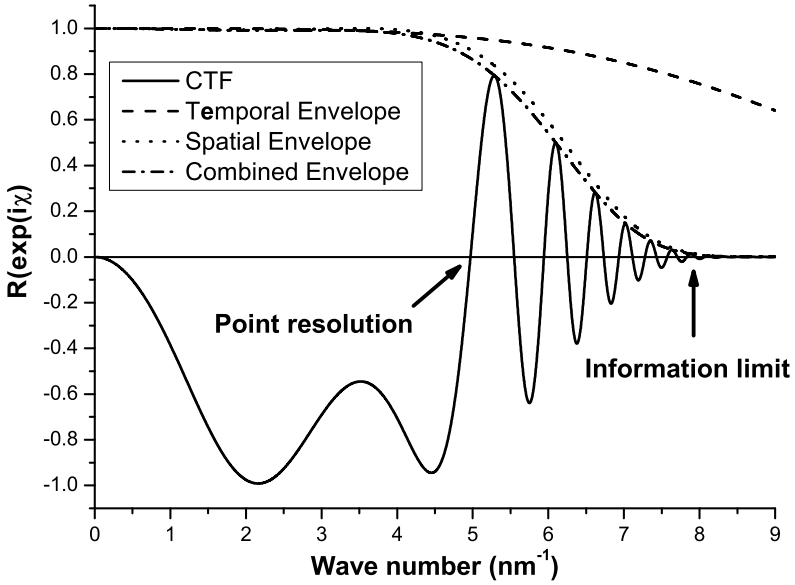

Figure 3.5: Contrast transfer function for the Philips CM-300 transmission electron microscope at Scherzer defocus. The values used are V=300keV, C_s=1.4mm, C_c=1.4mm (chromatic aberration coefficient), energy spread=0.6eV. The point resolution is around 0.20nm. The information limit is the point where contrast is still transferred through the microscope, i.e. the point where the amplitude of the CTF reaches zero. From the figure this point is found at ca. 0.12nm. The theoretically determined value for the information limit is slightly better than that observed experimentally.

In a modern TEM, image acquisition is done using CCD's. A modern CCD provides the necessary sensitivity and dynamic range to record images at a high sampling rate. Modern computers provide the speed to store the large amounts of data acquired, ca. 1Mb/image, when recording at high sampling rates, here 2frames/s. The CM-300 at HTAS has two cameras mounted. Directly under the viewing chamber a Gatan Image Filter (GIF) is mounted. The GIF is used for recording high resolution images. Further, the GIF contains a spectrometer to record electron energy-loss spectra, see Section 3.2.1. On an off-axis port a highly sensitive CCD camera from Tvips GmbH is mounted which allows for image acquisition at video rate (25 frames/s in the PAL system). Images and movies are saved using DigitalMicrograph from Gatan or EMMenu from Tvips GmbH.

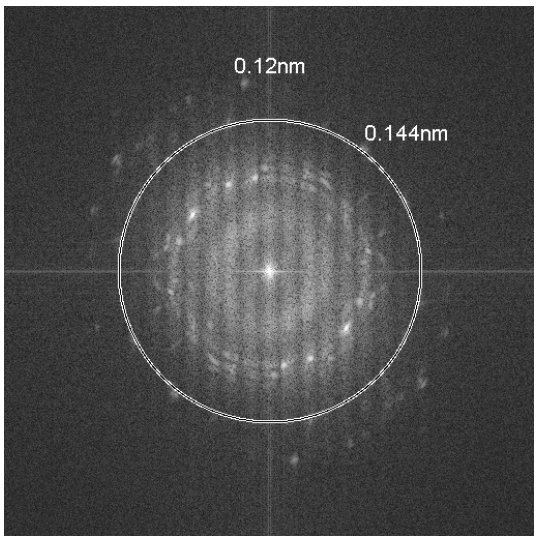

Figure 3.6: Young fringe Fourier transform. The figure shows the Fourier transform of an image obtained using a Philips CM-300 operating in in situ mode. The image was acquired in 5mbar nitrogen at room temperature [16]. Spots are symmetrically resolved to ca. 0.14nm. Spots representing smaller lattice spacings are observed but these are not found symmetrically. The dark rings in the image represents cross-overs of the CTF. The outermost spots labeled in the image are the (220) and (311) diffractions of gold.

3.2.1 Electron energy-loss spectroscopy - EELS

Electron energy-loss spectroscopy, *EELS*, is the analysis of the energy distribution of the electrons emanating from the sample. When the primary electrons traverse the sample, most of the electrons scatter elastically. However, a small amount of electrons scatter inelastically and lose an amount of energy characteristic of the elements present in the sample. They excite electrons in the sample to higher energy levels and the energy required is taken from the primary electrons. Hence, the energy of the electrons emanating from the sample are distributed according to the elements in the sample. The specific energy-loss is characteristic for the chemical environment in the sample. Therefore EELS can detect if a metal is present as an oxide or in metallic form. By guiding the electrons through a spectrometer they can be separated in energy and the energy-loss spectrum recorded.

Fig. 3.7 shows the two different parts of an electron energy-loss spectrum: the low loss and the core loss. The spectrum is shown as-acquired, i.e. without any post-processing. The low loss part is dominated by the zero-loss peak and the plasmon peak. The zero-loss peak shows the electrons that went unaffected through the sample and hence lost no energy. The plasmon

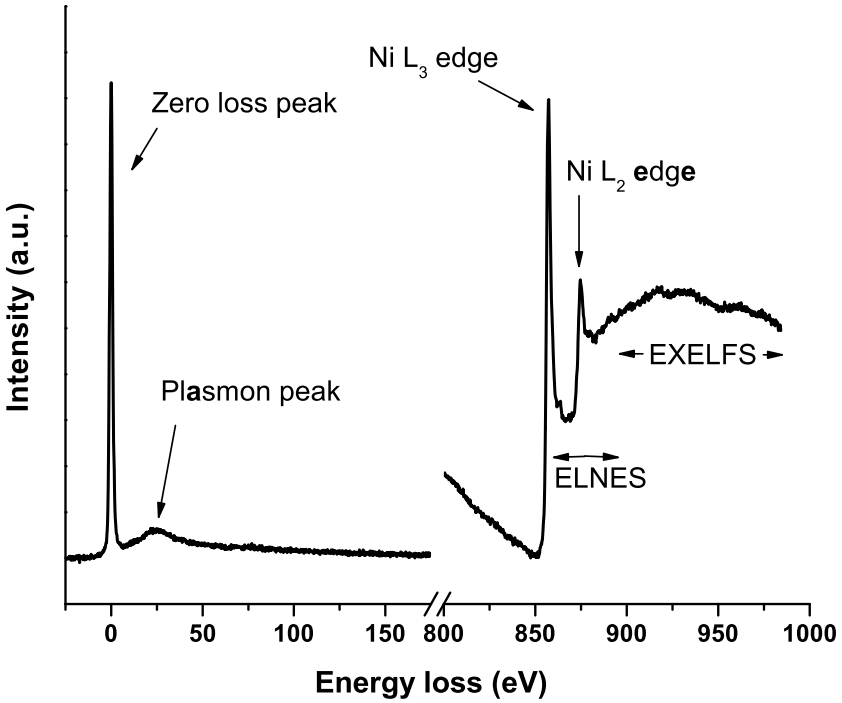

Figure 3.7: Electron energy-loss spectrum for nickel oxide showing the low-loss part and the core-loss part of the spectrum including the ELNES (energy-loss near edge structure) and EXELFS (extended energy-loss fine structure) regions. The two parts of the spectrum were acquired independently, but from the same region under the same conditions.

peak is a result of the electrons that excited a plasmon while traversing the sample. In metals the plasmons occur in the free electron gas. The valence electrons in a solid oxide can be thought of as a set of coupled oscillators. Excitation of these oscillators are similar to plasmons in metals. The second part of the spectrum is related to primary electrons interacting with core electrons in the sample. The sharp peaks are caused by core electrons being excited to the continuum or to unoccupied states. The ELNES (energy-loss near edge structure) region of the spectrum reflects the chemical environment and the local bonding geometry in the sample.

When high-energy primary electrons traverse the sample, there is a finite probability of exciting the electrons in the sample. The probability decreases with increasing energy-loss, hence at higher energy-losses the signal-to-noise ratio also decreases and longer acquisition times are needed as higher energy-

losses are measured. The intensity, I, in the spectrum as a function of energy, E, and angle, θ,is given by Fermi's golden rule [19, 20]

$$I(E,\theta) \propto \frac{4\gamma^2}{a_0^2 q^4} \left| \int \psi_i (\mathbf{q}\cdot\mathbf{r}) \psi_f^* d^3\mathbf{r} \right|^2 \rho(E). \tag{3.10}$$

where γ is the relativistic factor, a_0 is the Bohr radius and $\mathbf{q}$ the scattering vector. The term in the brackets is the transition matrix and ρ is the density of electron states (DOS). In the transition matrix, ψ_i is the initial core state and ψ_f is an unoccupied final state.

The transition matrix determines the basic shape of the spectrum and varies slowly with energy. As the energy-loss increases, the overlap between initial and final states decreases and the matrix elements become smaller. The strength of the matrix term is governed by the dipole selection rule: $\Delta l = \pm 1$. The density of states term in Eqn. 3.10 varies more strongly within the first few eV of the ionization edge and thus dominates the shape of the spectrum in this region, known as the ELNES. The core-level states are highly localized at the site of the excited atom. Thus there can be significant differences in the ELNES according to the chemical environment in the sample.

The basic shape of the L-edge in nickel is a rounded peak with a delayed maximum. Superimposed on this peak are sharp peaks corresponding to the L_3 and L_2 transitions (transitions from the $2p$ to the $3d$ level). A small peak corresponding to the L_1 is also present, but with low intensity. These peaks are known as *white lines* and are determined by the density of electronic states [20].

Electron energy-loss spectra are recorded using a magnetic prism. The prism is mounted below the viewing chamber as shown on Fig. 3.10. The electrons entering the prism are guided through a drift tube inside a magnetic prism and dispersed in energy by the Lorentz force as sketched in Fig. 3.8. By applying a potential to the drift tube the energy window can be selected. After dispersion the electrons are guided through a set of lenses for focusing in the direction perpendicular to the dispersion direction. In the GIF spectrometer used in this study, the energy-loss spectrum is recorded on a CCD.

3.2.2 In situ Transmission Electron Microscopy

One of the major drawbacks of conventional transmission electron microscopy is that the electron source requires UHV conditions. Further, any interaction of the electrons either before traversing the sample or after passage, degrades the image quality. Industrial catalysts operate at high pressures and high temperatures which do not comply with electron microscopy. So if observations under reaction conditions are desired, modifications to the microscope are needed. The pioneering work on catalysts using TEM at

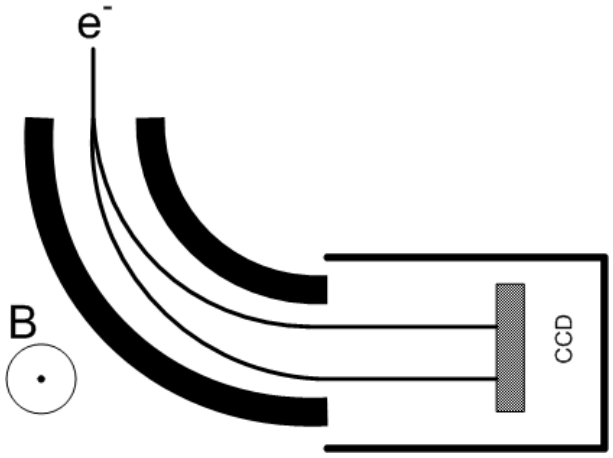

Figure 3.8: Electron energy-loss spectrometer. The electrons pass through the prism and are dispersed in energy. After dispersion the electrons are detected on the CCD.

elevated pressures was done in the late 60'ies by Hashimoto *et al.* [21] and later in the 70'ies by Baker and co-workers [22] with a resolution of around 2nm. They published excellent work on catalyst particle behavior [23] and on carbonaceous deposits [24]. In the 90'ies an improved version of the in situ TEM was designed and built at DuPont by Boyes and Gai [25], with a resolution around 0.23nm. In 1999 the in situ TEM was installed at HTAS with a resolution limit of ca. 0.14nm, capable of resolving the atomic lattice of the catalytically interesting transition metals. The design of the Topsøe in situ TEM is based on the differential pumping design of Boyes and Gai [25].

The importance of bringing down the resolution in transmission electron microscopes is illustrated in Fig. 3.9. The image shows a nickel particle on a magnesium aluminum spinel support at ca. 723K in 2.5mbar hydrogen. All the low-index planes are resolved in the Ni particle and the interface between the particle and the support is distinguishable, see Table 3.1 for lattice spacings in nickel. An important observation in Fig. 3.9 is that the Wulff point is above the particle-support interface. The Wulff point is the point that corresponds to the center of a cluster of equilibrium shape determined by the surface free energy floating freely in space [26, 27]. High resolution images like Fig. 3.9 allow for calculation of the position of this point.

Fig. 3.10 shows the design of the in situ TEM at HTAS. The gas is introduced through a needle valve into the in situ cell through the gap between the pole pieces to a maximum pressure of approx. 10mbar. An extra in situ aperture is placed between the cell and the final condenser lens to

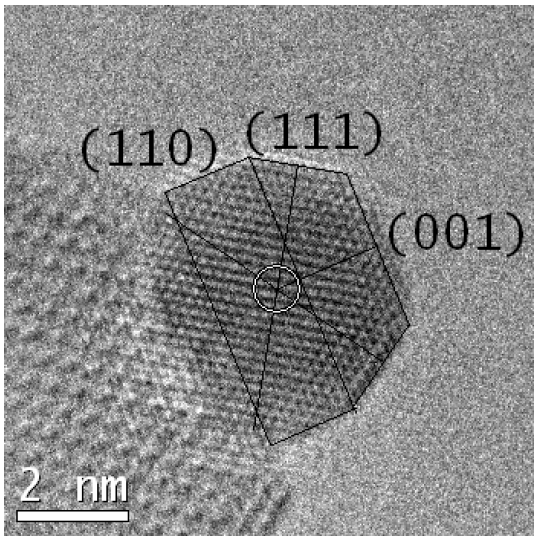

Figure 3.9: High resolution TEM image of a nickel particle on magnesium aluminum spinel support. The black lines indicate the Wulff construction around the particle. The image shows that the Wulff point of the Ni particle is above the particle-support interface. See Chapter 5 for a discussion on the particle-support interaction.

Crystal plane	Spacing (nm)
(022)	0.1246
(002)	0.1762
(111)	0.2035

Table 3.1: Plane spacing in metallic nickel.

confine the gas to a thin region around the sample. The first step of the differential pumping system of the TEM column is a molecular drag pump (MDP) pumping the column down to approx. 10^{-3}mbar. The port of the MDP is mounted just above the in situ aperture. The second step is a turbo molecular pump (TMP) with the port mounted just above the final condenser aperture evacuating the column to approx. 10^{-6}mbar. The last step of the differential pumping system is an ion getter pump with the port mounted above the first condenser lens. The IGP evacuates the column to approx. 10^{-8}mbar. In this way the gas in the in situ cell is pumped out of the column in three extra steps. The differential pumping system plus the standard mounted IGP's keep the FEG electron source at UHV.

Between the in situ cell and the viewing chamber the vacuum is maintained in a two step differential pumping system. The first step under the in

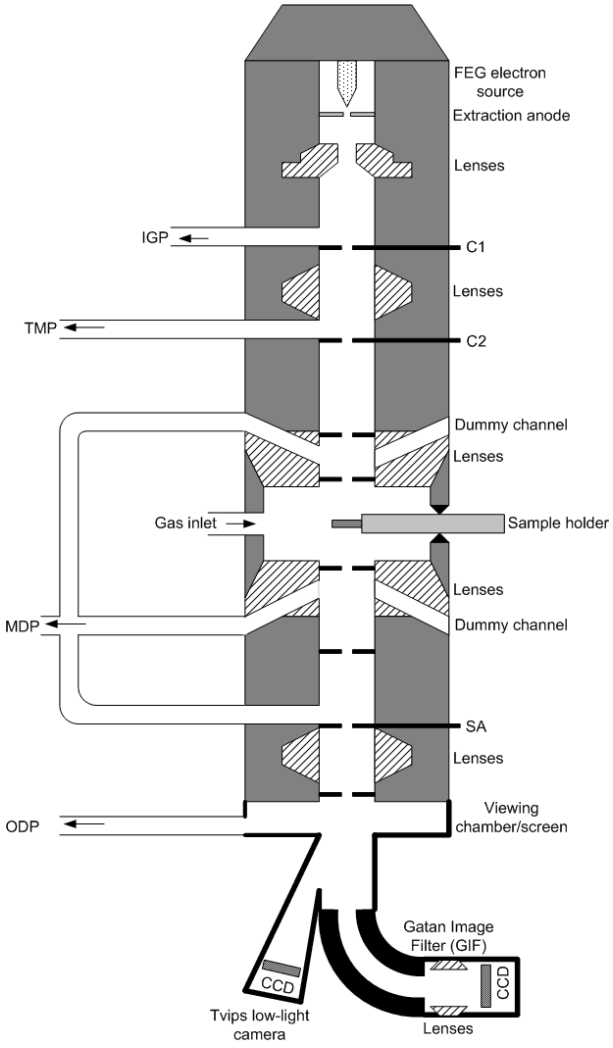

Figure 3.10: Schematic of the in situ microscope showing the mounting of the apertures and the image collection equipment. The low-light camera is mounted on an off-axis port. The ports for the different steps of the differential pumping system are shown. MDP is a molecular drag pump, TMP is a turbo molecular pump, and IGP is an ion getter pump. Dummy channels have been drilled in the pole pieces to make the lens symmetrical.

situ cell is evacuated by the same MDP that evacuates the region around the in situ cell. The viewing chamber is evacuated by the standard oil diffusion pump (ODP) of the TEM column, see Fig. 3.10.

The pressure limit of the in situ TEM depends on which gases are used and whether or not online observation is needed. When recording images,

the pressure limits in the in situ cell is ∼10mbar, slightly higher when using heavier molecules like O_2, CO_2, and CH_4 than when using e.g. H_2 due to the higher diffusivity through the column of the lighter molecules and the lower pumping efficiency of the pumps for H_2.

3.2.3 Sample Holders

Two different sample holders were used for the work presented in this thesis. Doing TEM at elevated temperatures in an oxidizing atmosphere is far from a standard situation, hence standard sample holders on the market are not directly applicable. For the experiments done under reducing conditions in pure hydrogen, a regular Philips PW6592 heating stage was used. This kind of stage provides high stability at temperatures up to ca. 1250K due to a 3-point suspension of the heating cup. However the heating filament in the stage burns out in less than 15 minutes when using it in a slightly oxidizing environment at high temperature. For the experiments done in oxidizing environments, a Gatan 928 heating stage was used. The Gatan heating stage is resistant to filament oxidation and can reach temperatures around 1073K in oxidizing environments depending on the atmosphere and pressure in the in situ cell. However the Gatan 928 stage is not as stable as the Philips PW6592 due to a 2-point suspension of the sample mounting cup and a water cooling system operating when the stage temperature is above 773K. The water flows through the stage giving rise to vibrations in the stage. For both holders, the temperature is measured on the outside of the sample mounting cup using a Pt-Rh thermocouple.

For both stages the maximum temperature is limited by the flow and composition of the gas in the in situ cell. The thermal conductivity of H_2 is higher than that of e.g. O_2 or H_2O. Thus when operating in pure hydrogen a higher heating current is needed to reach a certain temperature than when operating in atmospheres containing O_2 or H_2O at the same total pressure. Table 3.2 shows the thermal conductivities of some of the gases that have been used in the in situ TEM. The thermal conductivity of H_2 is ca. 10 times higher than that of H_2O which is also reflected by the heating currents needed when heating either stage in these gases. For this reason the pressure of H_2 has to be low when operating at high temperatures.

3.2.4 Applications of In Situ TEM

The differences between exposing catalyst samples to UHV conditions as opposed to gaseous atmospheres of different composition are illustrated by the following examples.

Many industrial catalysts contain small amounts of materials other than the catalytically active metal. These materials are known as *promoters*. Promoters, when added in small amounts, significantly enhance the activity

Gas	Thermal conductivity (mW/m·K)
H_2	186.9
H_2O	18.7
O_2	26.3
CO	25.0
CO_2	16.8
CH_4	34.1
C_3H_8	18.0

Table 3.2: Thermal conductivities for gases that have been used in the in situ transmission electron microscope. All values are at 1bar, except H_2 and CO where low pressure limits are given. The difference between low pressure values and values at 1bar are generally less than 1% [28].

and/or selectivity of the catalyst. Promoters are distinguished as structural and electronic in nature. The role of a structural promoter is to create more active sites on the catalyst surface. The electronic promoter enhances the turn over frequency of the individual active sites. A structural promoter might thus be difficult to observe using TEM as it is most likely integrated into the metal particles, whereas the electronic promoter may be present as separate phases on the metal particle surface.

A highly active boron nitride supported and barium promoted ruthenium catalyst for ammonia synthesis [29] was imaged under vacuum and under hydrogen/nitrogen. The small amount of barium acts as a promoter [30]. Fig. 3.11 shows conventional as well as in situ TEM micrographs of the ruthenium particles supported on boron nitride. In vacuum, the ruthenium particles are covered by a shell of the boron nitride support material, Fig. 3.11(a) and 3.11(b). This cannot be the active state of the catalyst as reactants are not able to reach the active sites on the surface of the catalyst. The surface features of the metal particles are hidden beneath the boron nitride shell making observation of the metal particle surface difficult. When exposing the catalyst to an environment mimicking that in an ammonia reactor, 3:1 H_2/N_2, at a pressure compatible with the in situ TEM, ca. 5.2mbar, and keeping the catalyst at ca. 825K, the shells on the surface of the metal particles are not present, Fig. 3.11(c) and 3.11(d) [31]. The surface of the ruthenium particles contained species different from the metal. The TEM observations in conjunction with electron energy-loss spectroscopy showed that this layer consisted of a barium phase. These observations led to the conclusion that the barium promoter was of an electronic nature [31]. The observed barium containing surface layer on the ruthenium particles is just 1 atomic layer thick.

When the atmosphere over a catalyst particle changes, the distribution

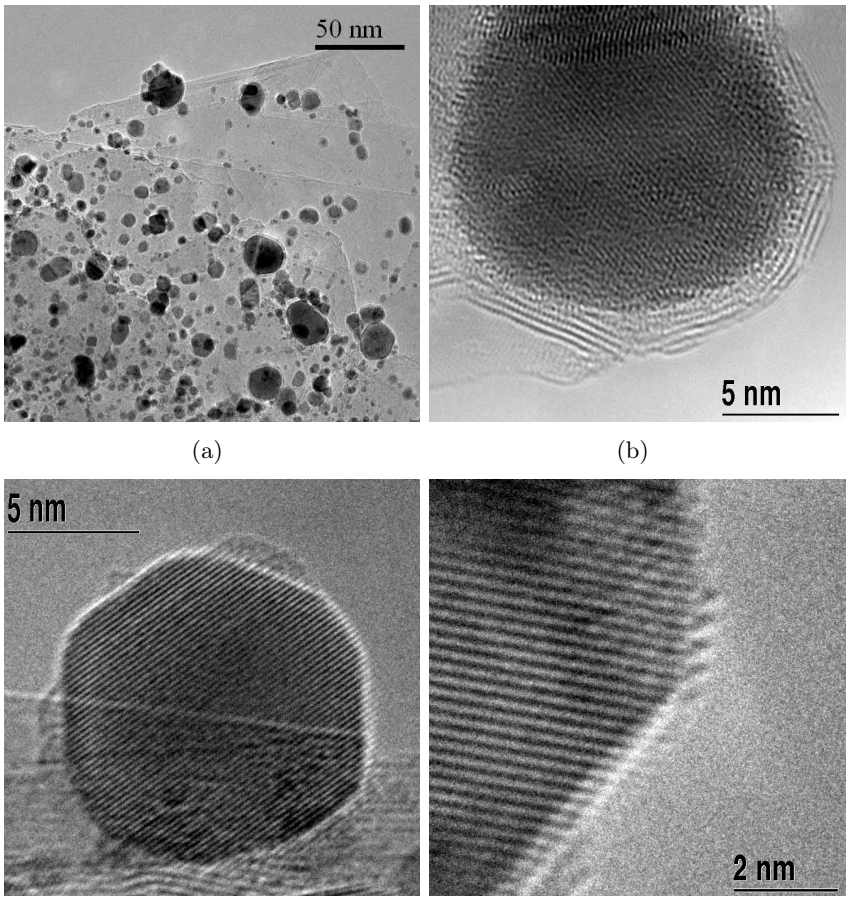

Figure 3.11: High resolution transmission electron micrographs of ruthenium on boron nitride. When the catalyst is exposed to UHV conditions, 3.11(a) and 3.11(b), the ruthenium particles are covered by a shell of boron nitride. When they are heated in 3:1 H_2/N_2 the shell disappears and the surface features can be seen, 3.11(c) and 3.11(d).

of the adsorbed species changes. This can change the fractional distribution of the exposed crystal facets. As the turn-over frequency of sites on different crystallographic surfaces is different the overall activity changes as the distribution among the crystal facets changes.

When a copper/zinc oxide support is exposed to environments of different reduction potentials relevant for methanol synthesis, the shape of the copper particles changes. These changes are seen in Fig. 3.12. When changing from a dry reducing environment like hydrogen to a wet environment, the copper particles expose less of the close-packed surfaces and more of the more open

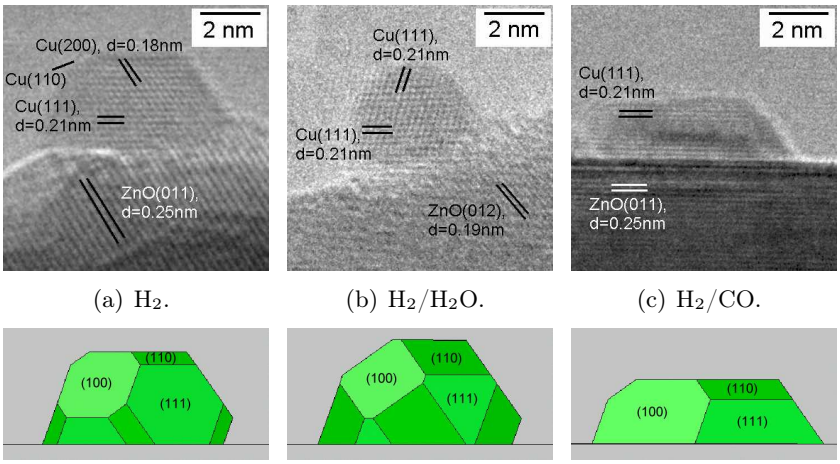

(a) H_2. (b) H_2/H_2O. (c) H_2/CO.

(d) Wulff construction of 3.12(a). (e) Wulff construction of 3.12(b). (f) Wulff construction of 3.12(c).

Figure 3.12: High-resolution TEM images and Wulff constructions of a Cu/ZnO catalyst showing morphological changes of copper particles as a function of atmosphere [33].

surfaces. The result of changing to an environment more reducing than H_2 causes the particle to wet the surface of the support more, i.e. have a large interface to the support material. Such phenomena cannot be observed in a conventional TEM. The observed changes in particle morphology can be compared to Cu-Cu coordination numbers obtained from in situ EXAFS data and catalytic activity of a similar methanol catalyst exposed to a dry and a wet synthesis gas respectively [32]. The variation in the catalytic activity of the catalyst correlated well with the variation in coordination coordination number. This is in agreement with the variation in morphology of the copper particles observed in the in situ TEM data [16, 33].

The examples mentioned above show that catalyst structures are very sensitive to reaction conditions. The working state of the catalyst may look very different than the state that is observed in vacuum.

3.3 Scanning Electron Microscopy

Whereas images in the transmission electron microscopes are formed from electrons that pass through the sample, they are formed from electrons coming back from the sample in the scanning electron microscope (SEM). A beam of electrons, typically with a primary energy between 1-30keV, is raster scanned across the sample. From the electron source, electrons are passed through a set of condenser lenses, as in the TEM. The beam is then passed

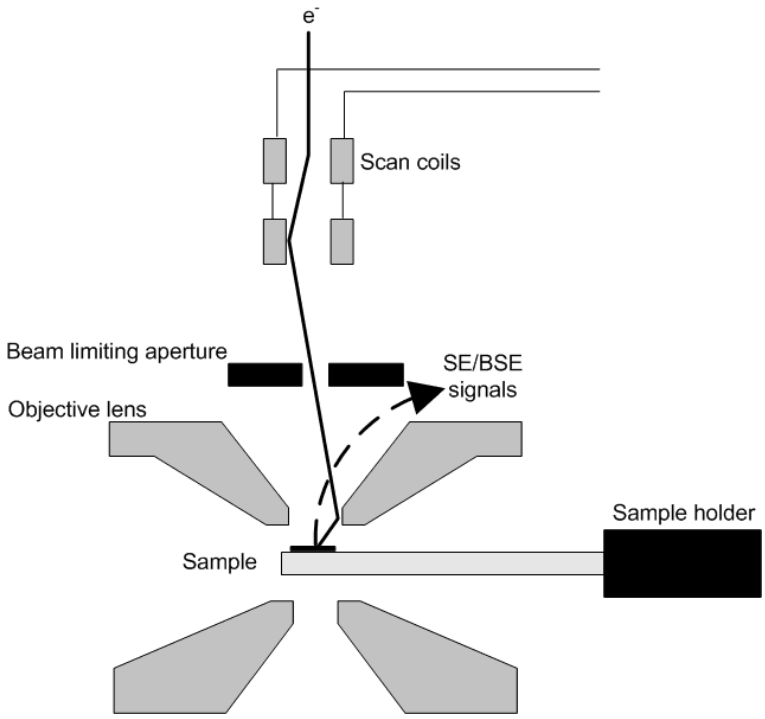

Figure 3.13: Illumination system in a scanning electron microscope. A set of scan coils controls the position of the electron beam on the sample. The objective lens focuses the beam onto a spot on the sample. The sketch is based on the lens configuration of the Hitachi S-5200 microscope.

through a set of scan coils that determines the position of the beam on the sample. After the scan coils a final beam limiting aperture limits the convergence of the beam and it is passed into the objective lens that focuses the beam onto a spot on the sample. Fig. 3.13 shows the path of the electrons as they pass through the lens system of the SEM.

When primary electrons interact with the sample, the primary electrons cause either *secondary electrons* (SE's) or *backscattered* (BSE's) to be emitted from the sample. The secondary electrons are a result of inelastic interactions of the primary electrons with the sample causing electrons to be emitted. The secondary electrons are usually emitted from the sample with energy less than ca. 50eV [15]. The other possibility is that the primary electrons are backscattered from the sample. The energy distribution of the backscattered electrons has a peak just below the primary electron energy and a tail towards zero. As the secondary electrons are lower in energy than the backscattered electrons they can be separated from the high energy backscattered electrons with an electric field. Because of the low energy

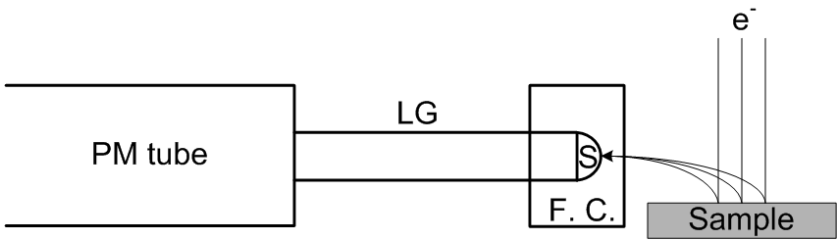

Figure 3.14: Everhart-Thonley detector. PM tube is the photomultiplier tube, LG the light guide, S the scintillator, and F. C. the Faraday cage. The sketch is drawn with positive bias voltage on the Faraday cage.

of the secondary electrons they only escape from the topmost layers of the sample and hence carry information from this layer. A secondary electron image thus gives information about the topography of the sample. The higher energy backscattered electrons can escape from deeper in the sample. The number of backscattered electrons depends on the atomic number of the sample. Hence a backscatter electron image gives information about the composition of the sample.

Most commonly an Everhart-Thornley detector (E-T detector) is used to detect the electron signals in the scanning electron microscope. The E-T detector consists of a Faraday cage covering a scintillator, a light guide and a photomultiplier. The Faraday cage is placed outside the detector and either a negative or a positive bias voltage can be applied to it. When a negative bias voltage is applied, all secondary electrons are rejected and hence only the backscatter signal is detected. When a positive bias voltage is applied to the Faraday cage, the secondary electrons are attracted to the detector. The positive bias voltage causes the trajectory of electrons emitted from the sample over a large solid angle to be deviated towards the detector. In the detector the electrons are accelerated to the scintillator where they induce light emission. The light is guided to the photomultiplier tube amplifying the signal and converting it into an electric current which can be read out on a screen. The backscattered electrons can also be detected using a solid state detector, e.g. a YAG detector, above the sample [15]. Such a detector provides higher geometric efficiency than a negatively biased E-T detector.

Figure 3.15 shows trajectories of primary electrons as they traverse the sample. The blue traces are electrons scattered in the sample and never reach the surface. The red traces show electrons that are either backscattered or escape from the surface after undergoing elastic or inelastic scattering in the sample.

The number of electrons generated by each primary electron is characterized by the backscatter and secondary electron coefficients, η and δ. The

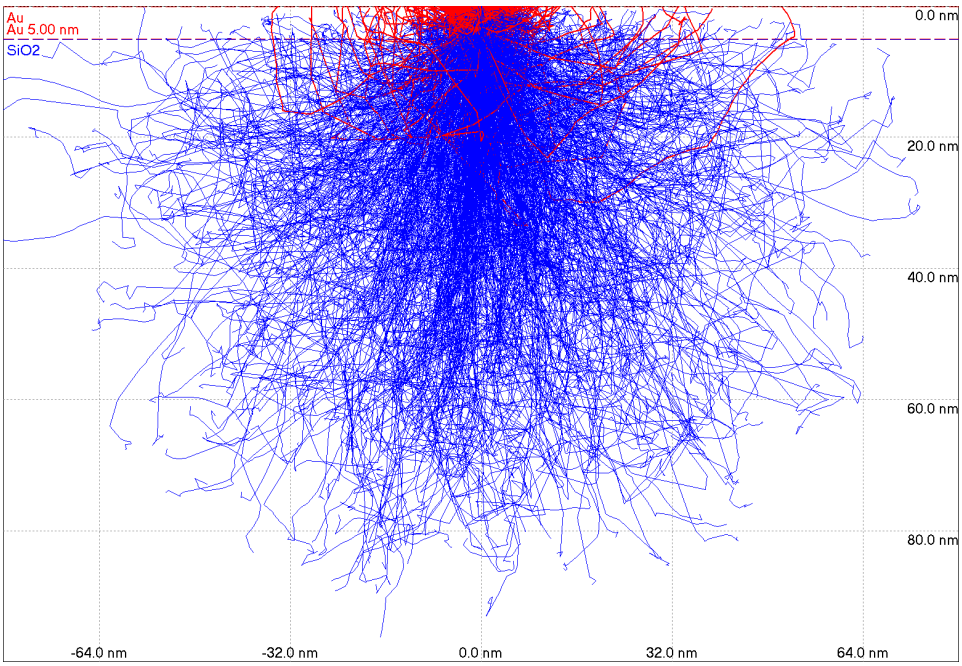

Figure 3.15: SEM interaction volume. The figure shows the traces of the electrons as they traverse the sample. The red traces show electrons that escape the surface of the sample and can be detected. The blue traces show electrons that do not escape the sample. The simulation was done using the Casino program [34] with a primary electron energy of 2kV.

backscatter coefficient is a function of primarily the energy of the primary electrons, E, and the atomic number, Z, of the sample. The dependence can be described as [35]

$$\eta(Z, E) = E^m C \tag{3.11}$$

where

$$m = 0.1382 - \left(\frac{0.9211}{\sqrt{Z}}\right) \tag{3.12}$$

and

$$C = 0.1904 - 0.2235(\ln Z) + 0.1292(\ln Z)^2 - 0.01491(\ln Z)^3. \tag{3.13}$$

The backscatter coefficient can be simulated by a Monte Carlo code like Casino [36]. Fig. 3.16 shows the simulated backscatter coefficients for a 5nm thick layer of gold on silicon dioxide (SiO_2) as a function of acceleration

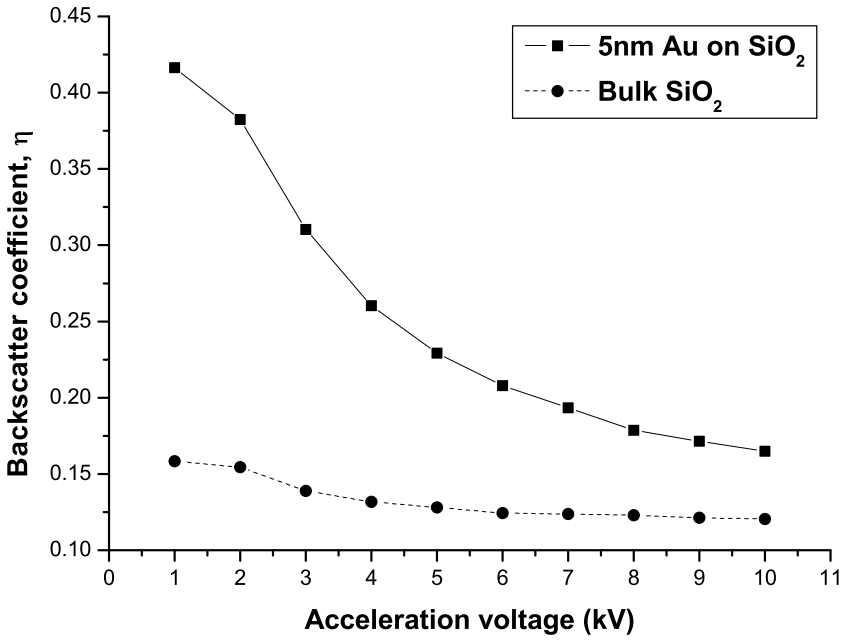

Figure 3.16: Backscatter coefficient as a function of acceleration voltage for a 5nm layer of gold on silicon dioxide and for clean silicon dioxide. The difference between the curves decreases as the acceleration voltage increases. The calculations were done using a beam diameter of 2nm.

voltage. For comparison the simulated backscatter coefficient for a clean slab of silicon dioxide is also shown. At low voltage there is a clear difference between the two backscatter coefficients, but as the voltage increases and the electrons penetrate deeper into the sample, the difference is evened out. Hence if gold particles of diameter 5nm on a silicon dioxide surface are to be detected, it is important to keep the acceleration voltage low.

The secondary electron coefficient is more illusive. It cannot be easily simulated or calculated, but several authors have listed experimentally determined values, see e.g. [37]. Generally the secondary coefficient increases with decreasing acceleration voltage [15].

Even when keeping the energy of the primary electrons low, metal oxides are still difficult to image. Different methods of imaging the sample can be used to further optimize the image quality. A scanning image can be acquired in two different ways. Either by scanning the electron beam slowly across the surface of the sample in a single pass (slow-scan), or by scanning the beam several times over the sample rapidly and adding the images (fast-

scan). The slow-scan method gives a sharp image and sample drift is usually not an issue. The downside is a relatively long dwell time in each pixel which can cause severe charging and beam damage to the sample. The fast-scan method gives a short dwell time in each pixel limiting charging problems and beam damage. The downside is that even a little drift in the sample will cause the image to be fuzzy as non-aligned images are layered.

Recent breakthroughs in scanning electron microscopy have made this technique more applicable for characterizing metal particles used in heterogeneous catalysis [15]. Improved lens technologies and field emission electron sources have increased the resolution of these instruments to the sub-nanometer regime and significantly improved the resolution at low voltages minimizing charging issues and optimizing imaging of the outermost layers of samples.

Figs. 3.17 and 3.18 illustrates the capabilities of a state-of-the-art scanning electron microscope, the Hitachi S-5200, with a resolution of 0.5nm at 30kV, but more important it is 1.7nm at 1kV. The figures show secondary electron images of mesoporous SBA-15 silica. Optimizing the parameters mentioned above is important when imaging nano-particles on oxide materials. Usually oxides are insulators or at best semiconductors. This makes this group of materials prone to charging problems in scanning electron microscopy. Hence they are best viewed at low voltages. At 1kV, the pores of SBA-15 are clearly visible and small gold clusters on the surface of the SBA-15 particles are observed. When increasing the voltage to 30kV, more gold clusters become visible as the electron beam penetrates deeper into the sample. In Fig. 3.18, there is a clear difference in the focus quality of the individual gold particles. Particles present deeper in the pore structure are more fuzzy as the electrons are scattered more as the pass through the SBA-15 material. This kind of resolution makes modern SEMs capable of analyzing metal particles in catalytic systems. Comparing Figs. 3.17 and 3.18, shows that there is a trade off between lateral and surface topographical resolution when changing the acceleration voltage. The lateral resolution of an SEM still increases with increasing voltage, but as the electrons penetrate deeper into the sample, the surface features vanish.

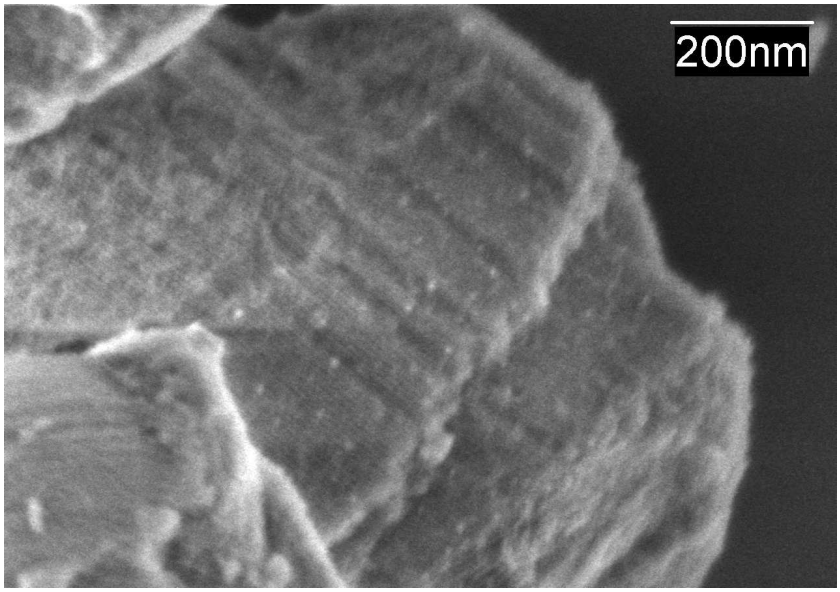

Figure 3.17: High-resolution secondary electron SEM image of Au on/in SBA-15 imaged at 1kV. The pores in SBA-15 are easily observed and the small gold clusters clearly visible. See text for further details.

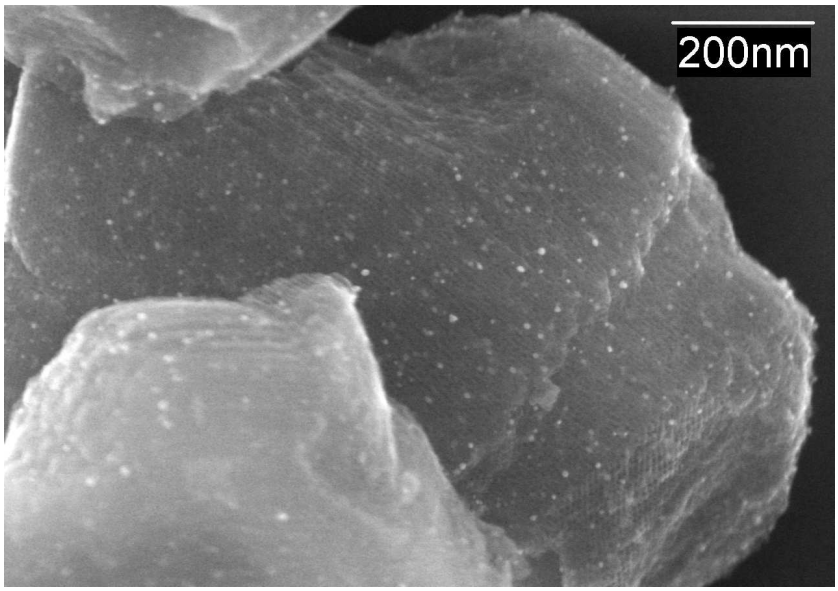

Figure 3.18: High-resolution secondary electron SEM image of Au on/in SBA-15 imaged at 30kV. The pores in SBA-15 are only vaguely observed. The small gold clusters are clearly visible at different focus reflecting the depth of the gold clusters in the SBA-15 particle. See text for further details.

Chapter 4

Sintering of Supported Metal Nano-particles

4.1 Introduction

The growth of supported metal nano-particles and the resulting loss of surface area is referred to as *sintering*. Sintering, or thermal deactivation, is a severe mechanism of deactivation in all high temperature processes, such as close-coupled automotive exhaust catalysts, where the catalytic converter has been brought close to the engine to achieve faster light-off due to the higher temperature. Sintering also represents a significant deactivation mechanism in catalytic reforming of petroleum-based hydrocarbons [38,39]. In steam reforming of methane, where temperatures in some parts of the reactor reach more than 1300K, sintering is an important deactivation mechanism. As the atmosphere in a steam-reforming reactor contains water vapor, the process is further enhanced [40,41]. A fundamental understanding of catalyst sintering is of paramount importance because of the drastic economic consequences related to the failure of industrial catalysts.

The deactivation routes of supported catalysts can in principal be divided into 4 groups: 1) poisoning, 2) fouling, 3) volatilization, and 4) sintering [39]. The first group can be described as chemical deactivation, the second as mechanical deactivation, and the last two groups as thermal deactivation. In this study only the sintering part of the thermal deactivation will be studied. Sintering is a complicated process influenced by numerous parameters, e.g. temperature, surrounding atmosphere, support morphology, and catalyst composition. Most important are the temperature and the atmosphere. Sintering of nickel-based catalysts have been studied by several groups [4, 11, 41–48] highlighting different aspects of the sintering process. However, sintering is an issue for all catalysts, although it occurs to different extents.

In a modern steam-reforming reactor, oxide supported Ni-based catalysts

are commonly used [4]. At the high temperatures encountered in the reactor, sintering represents an important route of catalyst deactivation. Further, the environment in the steam-reformer contains water vapor which has been shown to increase the sintering rate [11, 39, 41, 49]. A fundamental understanding of the mechanism underlying sintering is important if new and more sintering resistant catalysts are to be developed. The latter is true for all supported metal catalysts.

4.2 Mechanisms for Particle Growth

Two mechanisms of particle growth have attracted the most attention. The first is growth by interparticle transport, or Ostwald ripening, the other is particle migration and coalescence. The driving force for both of these mechanisms is the minimization of the total surface energy of the system. Both mechanisms involve migration of atomic species on the surface of the metal particles. In the Ostwald ripening regime the atomic species overcome the energy barrier $H_e - H_s - H_{m,s}$, see Fig. 4.1, and migrate from the particle onto the support where the diffusion barrier is $H_{m,s}$. In the particle migration regime, the atomic species stay on the surface of the metal particles where the energy barrier for migration is $H_{m,c}$. As more bonds have to be broken to get from the metal particle onto the support, energy barrier $H_e - H_s$ in Fig. 4.1, than in the case of diffusion on the surface of the metal particle, Ostwald ripening requires more energy, i.e. higher temperature, than particle migration and coalescence. The two mechanisms are outlined below.

4.2.1 Sintering by Ostwald Ripening

Consider an ensemble of metal particles on a support. The metal particles can wet the support and make a contact angle, θ, defined by

$$\gamma_s = \gamma_{ms} + \gamma_m \cos\theta \tag{4.1}$$

where γ_s is the surface free energy of the support, γ_{ms} the surface free energy of the support-metal interface, and γ_m the surface free energy of the metal particles, see Fig. 4.2. The difference in the chemical potential of the particles within the distribution will determine the net rate of mass transport. The chemical potential, μ, can be expressed by the Gibbs-Thompson equation [50]

$$\mu = \mu_0 + \frac{2\gamma_m \Omega}{r} \tag{4.2}$$

where μ_0 is the chemical potential of an infinitely large particle, Ω is the atomic volume, and r is the radius of curvature of the particle, see Fig. 4.2. As the chemical potential varies as $1/r$ the net mass transport will be from the small particles to the large particles.

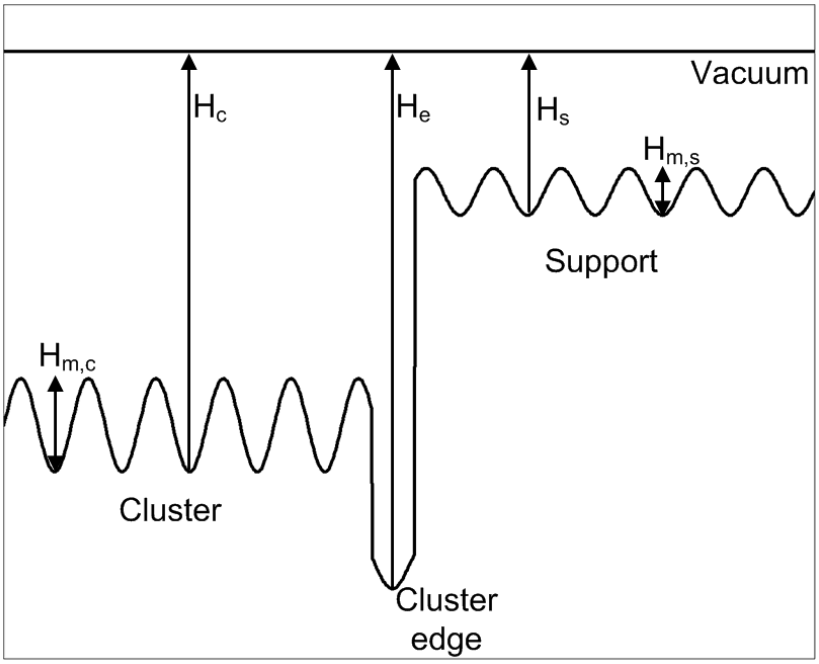

Figure 4.1: Energy landscape on the surface of a catalyst. The terms used on the figure are: H_c, binding energy on cluster, terrace, H_e, binding energy at cluster edge and H_s, binding energy on the support. In particle migration and coalescence, atomic species migrate on the surface of the metal particles with an energy barrier of migration $H_{m,c}$. In Ostwald ripening, the migrating species can overcome the energy barrier $H_e - H_s - H_{m,s}$ and migrate onto the support where the energy barrier of migration is $H_{m,s}$.

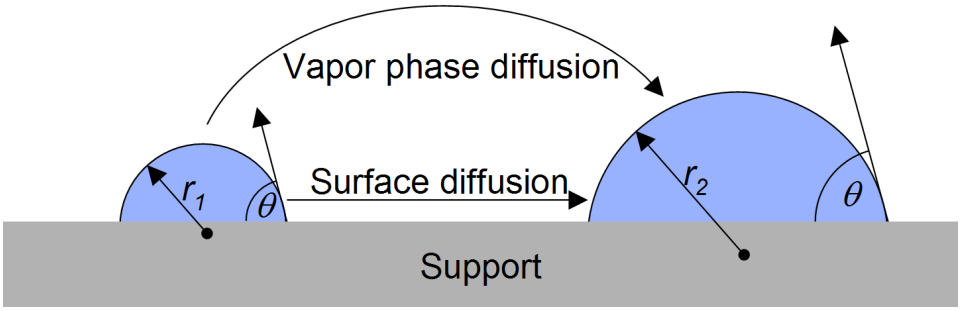

Figure 4.2: Schematic of sintering by Ostwald ripening. Mass is transported from the small particle ($r = r_1$) to the large particle ($r = r_2$) either through diffusion on the surface of the support or through diffusion through the vapor phase. θ is the contact angle between the particles and the support.

Two processes determine the rate of sintering by Ostwald ripening: 1) the detachment of the mass transporting species from the smaller particles, and 2) the diffusion of the mass transporting particles, either on the surface of the support or through the vapor phase. The former is known as interface control, the latter as diffusion control. Transport through the support seems unlikely.

In both cases, interface control and diffusion control, the particle size distribution function is a product of a time dependent term and a $\tilde{d} = d/\bar{d}$ term, where d is the particle diameter and $\bar{d}$ is an experimentally determined average diameter. In the case of diffusion control, the particle size distribution function, f_d, is given by [51, 52]

$$f_d(t, \tilde{d}) = \frac{c_d \phi_d(\tilde{d})}{(1 + t/t_d)} \tag{4.3}$$

where c_d is a normalization constant, t is time, t_d is a characteristic time, and ϕ_d is a size dependent self-similar distribution function. In the case of interface control, the distribution function, f_i, is given by [51, 52]

$$f_i(t, \tilde{d}) = \frac{c_i \phi_i(\tilde{d})}{(1 + t/t_i)} \tag{4.4}$$

where the terms are analogous to the definitions in Eqn. 4.3.

Chakraverty [51] also determined the shape of the distribution function. In both cases, diffusion control and interface control, the shape of the distribution function has a tail on the small diameter side and a sharp cutoff at large diameters. More recently, Finsy [53] presented a theoretical derivation of the shape of the particle size distribution. Assuming that 1) the particles are fixed in space, 2) the system is infinitely dilute, 3) the concentration of atoms diffusing on the surface is the same outside 2 radii from the particles, and 4) species are transported by diffusion between particles, the shape of the time-independent particle size distribution function from an ensemble sintered via Ostwald ripening, ϕ_{O-R}, is given by

$$\phi_{O-R}(\tilde{d}) = \frac{81 e \tilde{d}^2 \exp(1/(2\tilde{d}/3 - 1))}{\sqrt[3]{32}(\tilde{d} + 3)^{7/3}(1.5 - \tilde{d})^{11/3}}. \tag{4.5}$$

The change in the average size of the particle size distribution function with time can also be calculated from the Chakraverty theory. For diffusion control and interface control these are given as

$$\left(\frac{\bar{d}(t)}{\bar{d}(0)}\right)_d = (1 + c_d t)^{1/4} \tag{4.6}$$

$$\left(\frac{\bar{d}(t)}{\bar{d}(0)}\right)_i = (1 + c_i t)^{1/2}. \tag{4.7}$$

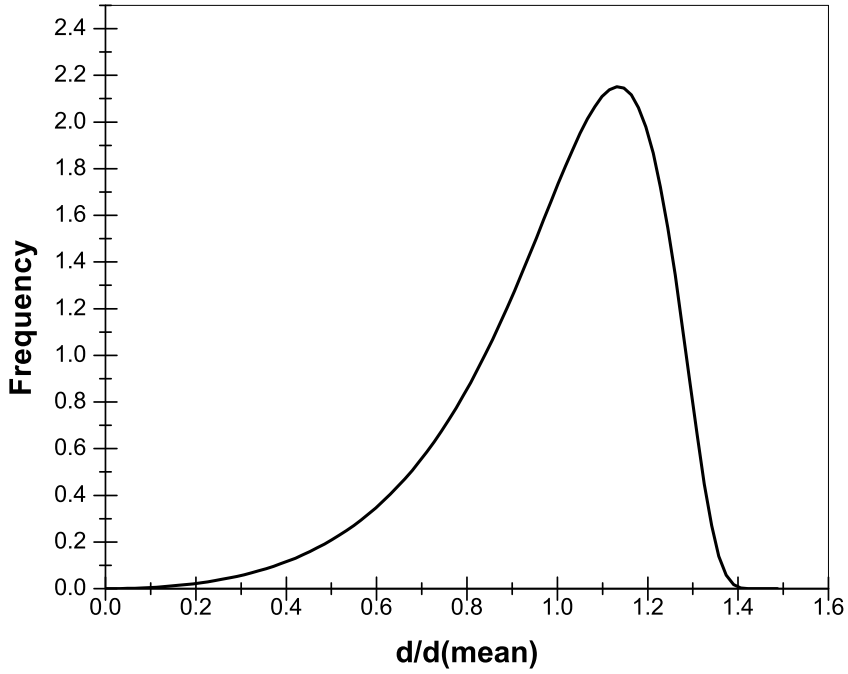

Figure 4.3: Theoretical model of a particle size distribution after sintering by Ostwald ripening [53]. The most prominent characteristics are that the distribution has a tail on the small diameter side of the peak and a sharp cut-off at larger diameters.

For both cases of Ostwald ripening, the tail on the small diameter side of the peak is a result of the continuous supply of small particles since particles below a certain critical radius will be decreasing in size. Computer simulations by De Smet *et al.* [54] showed that for particles that grew by Ostwald ripening, the particle size distribution evolved from having a sharp peak into a distribution of the form shown in Fig. 4.3 with a tail to the small diameter side. However experiments could not prove a distribution of this form [55]. Even though the particle size distribution evolved from a log-normal type distribution into a distribution having a sharper peak, the tail towards the small diameter side was not observed. Sault and Tikare [56] developed a Monte Carlo model for catalyst sintering. Their model shows that the particle size distribution develops bimodality which is explained by some particles coalescing and hence increasing their size. Running the simulation further, the two peaks are combined into one broad distribution which is attributed to sintering by Ostwald ripening. The model has no a priori assumptions on

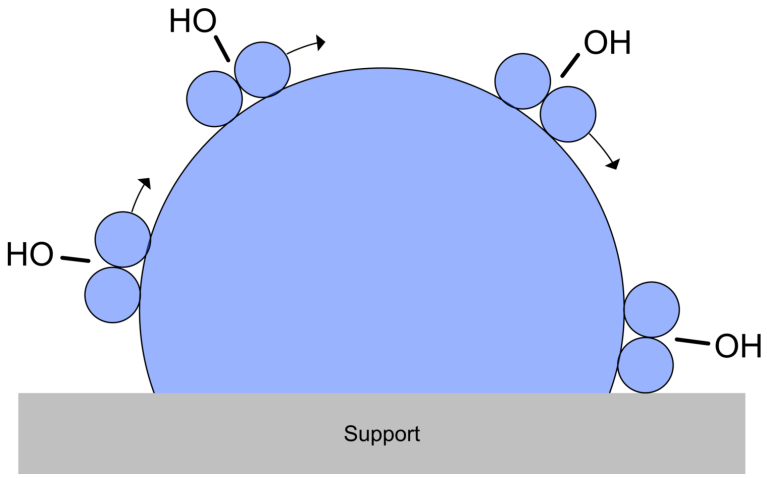

Figure 4.4: Schematic of the particle migration process. Species can move on the surface of the metal particle. When they gather on one side of the particle, the metal particle moves one atomic diameter. The OH group is explained in Section 4.3.2

mechanism, i.e. Ostwald ripening or particle migration. Zinke-Allmang *et al.* [57] have experimnetally shown particle size distributions with a tail on the small diameter side of the peak for Ge on Si. Rosenfeld *et al.* [58] also experimentally found distributions skewed to the small diameter side for Ag islands on Ag. The main differences in both these cases are that the supports are not an oxide and they were flat as opposed to the high surface area oxide supports usually used in catalysis. Wynblatt and Gjostein [42] elegantly show that the diameter of the particles that neither grow nor shrink when sintering by Ostwald ripening, d^*, is equal to the mean particle diameter $\bar{d}$. Hence over time the mean diameter will increase, but there will still be small particles present in the distribution.

4.2.2 Sintering by Particle Migration and Coalescence

Atoms on the surface of metal particles are not stable entities. When they move around the surface they cause the metal particle to move. Provided that the diffusion of the surface atoms is fast, i.e. $\sqrt{D_s t}$, where D_s the diffusion coefficient of the surface atoms, is comparable to the diameter of the metal particle, the movement of the surface atoms will cause the metal particle to move in a Brownian type motion. When two moving metal particles meet each other on a substrate, they can coalesce and become one particle. Fig. 4.4 schematically shows species moving on the surface metal particle.

Assuming that particles are spherical and do not wet the substrate, and that surface diffusion is the dominant transport mechanism [59], the the-

ory of Gruber [60] derived from the migration of bubbles in solids can be used to describe the migration of supported particles. The particle diffusion coefficient, D_p, in the Gruber model is given by

$$D_p = 0.301 D_s \left(\frac{a}{d/2}\right)^4. \tag{4.8}$$

where 0.301 is a geometric constant related to the FCC lattice, D_s is the surface diffusion coefficient on the particle, a is the atomic diameter and d is the particle diameter. Eqn 4.8 shows that the particle diffusion is strongly dependent on the particle diameter. The displacement, X_c of a metal particle undergoing random walk is

$$X_c = 2\sqrt{D_p t}. \tag{4.9}$$

The surface diffusion coefficient can be found from

$$D_s = D_0 \exp\left(\frac{-Q}{RT}\right) \tag{4.10}$$

where D_0 a constant [61], Q is the activation energy for surface diffusion, R is the gas constant and T is the temperature.

Fig. 4.5 shows the diffusion coefficients of nickel particles of different diameters as a function of temperature. The curves were calculated using Eqns. 4.8 and 4.10 with D_0=300cm^2/s, Q=159kJ/mol, a=0.23nm as given in [43].

Other expressions for the metal particle diffusion coefficient have been proposed for facetted crystals. Willertz and Shewmon [62] proposed the particle diffusion coefficient to be related to the particle diameter by

$$D_p = \frac{D_s d}{2\alpha_s} \exp(-g\pi d\gamma_e/kT) \tag{4.11}$$

where α_s is the distance the surface species move in each jump, g is the ratio of the facet diameter to the particle radius, γ_e is the edge energy of a monatomic pillbox and k is the Boltzmann constant. Other investigators also derived expressions for the particle diffusion coefficient showing an exponential decay with radius [63]. In this work the expression of Gruber, Eqn. 4.8, will be used.

The actual coalescence events were studied by Nichols and Mullins [64, 65]. The coalescence event was split into three steps: 1) the formation of a neck between the two coalescing particles and the initiation of mass transport, 2) neck elimination where the resulting particle is elongated, and 3) complete coalescence where the particle retains its equilibrium shape. The relaxation time for each of these steps is proportional to R_0^4/B where R_0 is the initial unperturbed particle radius and B is given by

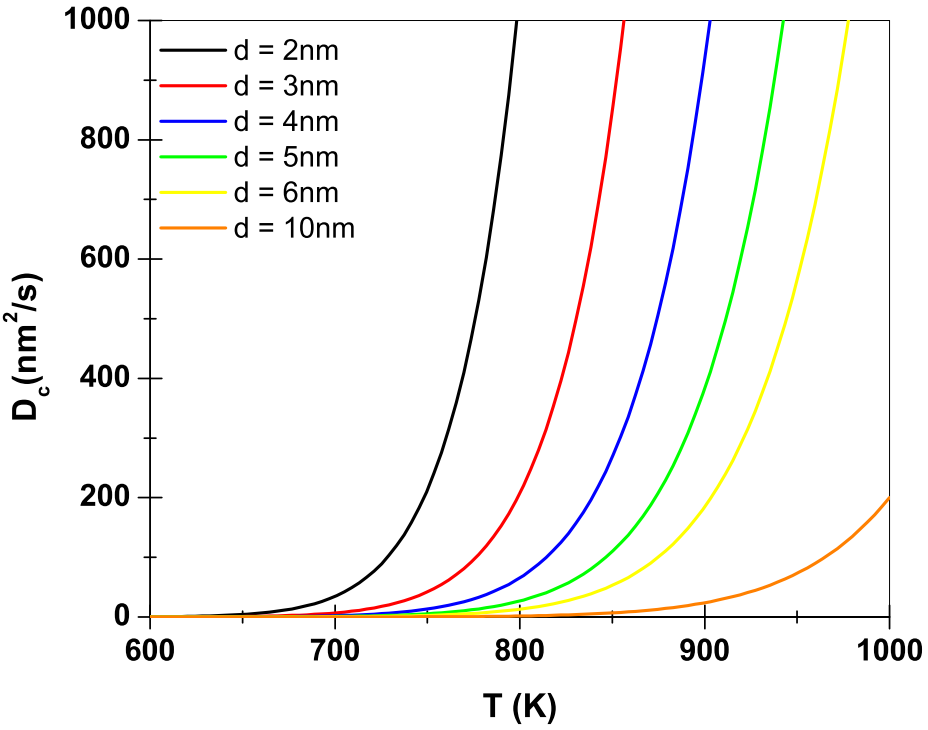

Figure 4.5: Calculated diffusion coefficients of nickel particles as function of temperature and size using $D_0 = 300cm^2/s$, Q=159kJ/mol, $a = 0.23nm$ [43].

$$B = \frac{D_s N_0 \gamma_0 \Omega^2}{kT} \tag{4.12}$$

where N_0 is the number of surface sites, Ω is the atomic volume and γ_0 is the average surface free energy. Wynblatt and Gjostein [42] give the relaxation times for complete coalescence of platinum particles, and find that particles 5nm in diameter coalesce completely in ca. 10^{-3}s at 873K and even faster at higher temperatures. This coalescence time is fast, making migration the rate determining step.

Another model, the binary collision model, was developed by Ruckenstein and Pulvermacher [66,67]. In the binary collision model, either the migration or the coalescence step can be rate limiting. More recently, Yacaman *et al.* [68] gave an account of the coalescence process attributing importance to the properties of the surface layers of the particles. The melting point of the metal particles increases with particle diameter, thus the smaller the particles the faster the coalescence event is expected to be in agreement with the authors mentioned above [42].

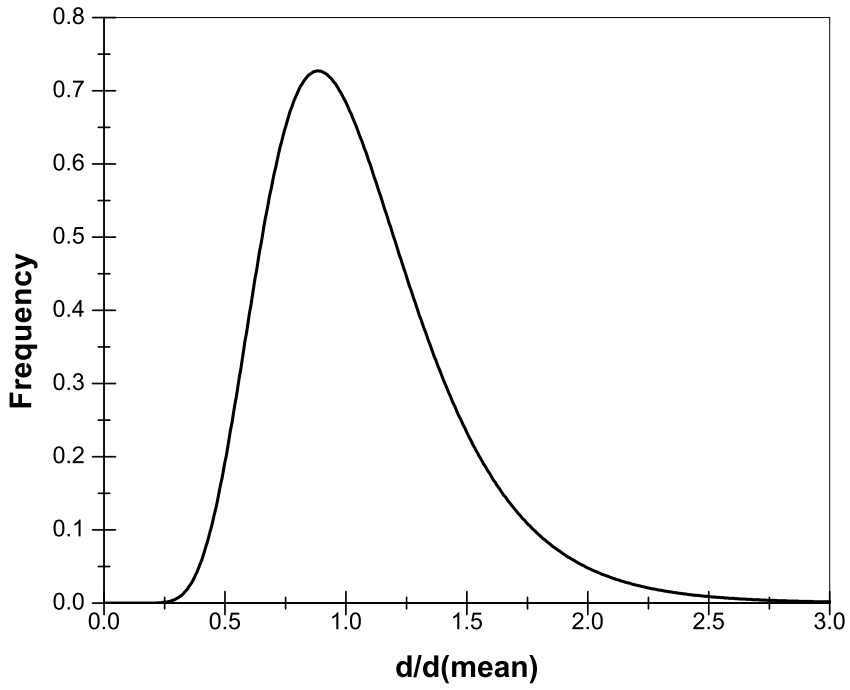

Figure 4.6: Theoretical model of a PSD after sintering by particle migration and coalescence. The most prominent characteristic is that the distribution has a tail on the large diameter side of the peak and has no specific cut-off.

The particle size distribution for an ensemble of particles sintered by particle migration and coalescence can in most cases be fitted by a log-normal distribution function, f_{L-N} of the form [69]

$$f_{L-N}(x) = y_0 + \frac{A}{\sqrt{2\pi}wx} \exp \frac{\left[\ln \frac{x}{x_c}\right]}{2w^2} \tag{4.13}$$

where y_0 is the offset, A the amplitude, w the width, and x_c is the center of the peak. The main characteristic of the log-normal distribution is the tail on the large diameter side of the peak, see Fig. 4.6.

4.3 Models for the Evolution of Metal Particles

This section describes different models for particle growth. Different models for the sintering of supported metal catalysts have been proposed. Power law expressions are general models that fit well with a multitude of systems.

These models are based on classical empirical analysis of sintering data. The Sehested model is used only for nickel-based steam-reforming catalysts, but the ideas may be used for other systems as well. The Sehested model is based on density functional calculations, micro-kinetics and experimental data. Below more details on the models are given.

4.3.1 Power Law Expressions

Different types of power law expressions have been developed to account for sintering of supported metal catalysts. The power law models express the exposed active metal area as the *dispersion* instead of the metal particle diameter. However, both terms are a measure of the exposed metal surface area. The dispersion of the catalyst is the fraction of metal atoms on the surface of the metal particles, i.e. it is a function of the diameter of the metal particles. In the simple power law expression, the change in dispersion with time is given by [70]

$$-\frac{d(D(t)/D_0)}{dt} = k_s \left(\frac{D(t)}{D_0}\right)^n \tag{4.14}$$

where $D(t)$ is the dispersion as a function of time, D_0 is the initial dispersion, k_s is the sintering rate constant and n is the sintering order. The sintering order may vary from 2-15 [70]. The sintering order varies as a function of temperature, atmosphere, and sintering mechanism [39]. It has been suggested that the sintering order could be used to determine the order of the processes involved, e.g. atom emission and capture. Sintering orders of 3-4 have been proposed to be suggestive for Ostwald ripening and sintering orders of 8-15 of particle migration and coalescence.

The general power law expression [71] is a modification to the simple power law expression that includes a term, D_{eq}/D_0, accounting for the observed asymptotic approach of the dispersion

$$-\frac{d(D/D_0)}{dt} = k_s \left(\frac{D}{D_0} - \frac{D_{eq}}{D_0}\right)^m. \tag{4.15}$$

where D_{eq} is the dispersion at infinite time and m is the sintering order. The general power law expression fits well with experimental data, but lacks reference to specific parameters pertaining to atmosphere, support and loading.

In the late 70'ies, it was heavily debated whether or not a sintering mechanism could be inferred from the shape of the particle size distribution after sintering. Chakraverty [51] derived a model for the grain size distribution in thin films. The model assumed surface diffusion and interface control. According to the model, particle size distributions should develop a tail on the small diameter side of the peak. The model was later improved by Wynblatt and Gjostein [42]. However, the model has been criticized because it is not in agreement with the experimental findings. More recently, Fuentes and

Salinas-Rodriguez [72] presented a model showing that particles sintered by Ostwald ripening evolve into a particle size distribution of the log-normal type.

Wanke [73, 74] argued that the distribution after sintering is a strong function of the initial distribution. Hence if the initial distribution is log-normal, the distribution after sintering also tends to be log-normal. Wanke further argues that the initial particle distribution is not only a function of the reduction temperature, but also of the impregnation method.

In a recent study, Datye *et al.* [75] show data for Pd and Pt catalysts sintered under conditions that should favor Ostwald ripening and particle migration and coalescence respectively. In the case of Pd, the Ostwald ripening mechanism is invoked due to the high vapor pressure of Pd at 1173K [76]. For the Pt particles, the vapor pressure is low [76], and the small Pt particles, <5nm, should be mobile at 973K [42]. In their study, all particle size distributions could be well fitted with a log-normal distribution with a tail extending to large diameters. This supports the conclusion that it is not definitive to deduce a sintering mechanism from the shape of the PSD alone.

4.3.2 The Sehested Model

The sintering model proposed by Sehested *et al.* [11, 49] for nickel-based steam reforming catalysts assumes that metal particles sinter by particle migration and coalescence. The model is based on the rate of collision between particles as determined by Ruckenstein and Pulvermacher [67], and assumes that the initial particle size distribution has a log-normal shape. Using these assumptions, the rate of collision per gram of catalyst is given by

$$\Phi(s^{-1}g^{-1}) = c_{cat} \int_{-\infty}^{\infty} \Phi_j(s^{-1}) f_{L-N}(d_j) \mathrm{d}ln\left(\frac{d_j}{\bar{d}}\right) \tag{4.16}$$

$$= const.c_{cat}c_{car}D(\bar{d^n}) \tag{4.17}$$

where c_{cat} is the number of particles per gram of catalyst, Φ_j is the collision rate of particles with diameter d_j, f_{L-N} is the log-normal distribution function, c_{car} is the number of particles per support surface area, D is the diffusion constant and $\bar{d}$ is the average particle diameter. Using numerical integration, it can be shown that the increase in average particle diameter due to one collision in an ensemble consisting of N particles, is given by [49]

$$\Delta(\bar{d}) = const.\frac{\bar{d}}{N-1} \approx const.\frac{\bar{d}}{N}. \tag{4.18}$$

By substituting N with c_{cat} in Eqn. 4.18, the average increase in the average particle diameter is obtained. Using Eqn. 4.17 and 4.18, the increase in average diameter as a function of time per gram of catalyst can be determined

$$\frac{\mathrm{d}(\bar{d})}{\mathrm{d}t} = \Phi\Delta(\bar{d}) = const.\frac{\bar{d}}{c_{cat}}c_{cat}c_{car}D(\bar{d}^n). \tag{4.19}$$

With

$$c_{cat} = const.\frac{X}{\rho\bar{d}^3} \tag{4.20}$$

$$c_{car} = const.\frac{X}{\rho(1-X)A\bar{d}^3} \tag{4.21}$$

where A is the surface area per gram of support, ρ the density of the metal, and X is the fractional metal loading, Eqn. 4.19 can be written as

$$\frac{\mathrm{d}(\bar{d})}{\mathrm{d}t} = const.\frac{D(\bar{d}^n)X}{\rho(1-X)A\bar{d}^2}. \tag{4.22}$$

Particle diffusion is assumed to be described by the Gruber model, Eqn. 4.8 [60]. In a non-interacting atmosphere, ad-atoms are responsible for the surface mass transport. Eqn. 4.8 is thus modified to take the form

$$D_{particle}^{ad-atom} = 4.818D_{ad-atom}\left(\frac{a^4}{\bar{d}^4}\right)K_1{}^1 \tag{4.23}$$

where K_1 is the equilibrium constant for the formation of ad-atoms. The activation energy for this process is given as 111kJ/mol [12].

By inserting Eqn. 4.23 in Eqn. 4.22 and integrating over time, an expression for the mean particle diameter is obtained

$$\frac{\bar{d}_{\mathrm{Ni}}}{\bar{d}_0} = \left(const.\frac{K_1D_{\mathrm{Ni}}Xt}{\bar{d}_0^7(1-X_{\mathrm{Ni}})A} + 1\right)^{1/7} \tag{4.24}$$

where $\bar{d}_0$ is the initial mean particle diameter, D_{Ni} is the diffusion coefficient of the nickel particles, and *const* a time independent constant not necessarily the same in Eqns. 4.17 - 4.24.

More recently DFT calculations have shown that it is more likely that the mass transporting surface species are Ni_2-OH dimers [11]. The activation energy of forming a nickel dimer bonded to an OH radical is 54kJ/mol, significantly lower than the activation energy of forming the ad-atom. However, the activation energy for diffusion of the ad-atom is 16kJ/mol lower than for the dimer. In H_2O containing environments the number of mobile species increases leading to an increased sintering rate. Ni_2-OH complexes are formed by the reaction

$$2_{*\mathrm{Ni}(111)} + \mathrm{H_2O}(g) + 2\mathrm{Ni}_{bulk} \rightleftharpoons \mathrm{Ni_2} - \mathrm{OH}(2_{*\mathrm{Ni}(111)}) + 0.5\mathrm{H_2}(g) \tag{4.25}$$

[1]Note that the radius in Eqn. 4.8 has been changed to diameter in Eqn. 4.23, thus changing the prefactor.

where *Ni(111) is a surface site on the (111) facet of nickel. The equilibrium constant for the formation of the complexes is

$$K_2 = \frac{\theta_{\mathrm{Ni_2-OH}}}{(1-2\theta_{\mathrm{Ni_2-OH}})}\frac{\sqrt{P_{\mathrm{H_2}}}}{P_{\mathrm{H_2O}}} \tag{4.26}$$

where $\theta_{\mathrm{Ni_2-OH}}$ is the coverage of Ni_2-OH and P_{H_2} and P_{H_2O} are the pressures of hydrogen and water respectively. Assuming the coverage of Ni_2-OH is low, Eqn. 4.26 can be expressed as

$$\theta_{\mathrm{Ni_2-OH}} \approx K_2\frac{P_{\mathrm{H_2O}}}{\sqrt{P_{\mathrm{H_2}}}}. \tag{4.27}$$

Following Gruber and Sehested, the metal particle diffusivity where the dominant mass transporting specie is Ni_2-OH is given by

$$D_{particle}^{OH-dimer} = 9.632 D_{OH-dimer}\left(\frac{a_0^4}{d^4}\right)K_2\frac{P_{\mathrm{H_2O}}}{\sqrt{P_{\mathrm{H_2}}}} \tag{4.28}$$

and the analogue of Eqn. 4.24 with Ni_2-OH dimers as mass transporting specie becomes

$$\frac{\bar{d}_{\mathrm{Ni}}}{\bar{d}_0} = \left(const.\frac{K_2 D_{OH-dimer} X_{\mathrm{Ni}}\tau}{\bar{d}_0^7(1-X_{\mathrm{Ni}})A}\left(\frac{P_{\mathrm{H_2O}}}{\sqrt{P_{\mathrm{H_2}}}}\right)+1\right)^{1/7} \tag{4.29}$$

where τ is the sintering time. For fitting purposes, the constants *const.*, K_2, and $D_{OH-dimer}$ are combined into one constant C, so Eqn. 4.29 takes the form

$$\frac{\bar{d}_{\mathrm{Ni}}}{\bar{d}_0} = \left(\frac{C X_{\mathrm{Ni}}\tau}{\bar{d}_0^7(1-X_{\mathrm{Ni}})A}\left(\frac{P_{\mathrm{H_2O}}}{\sqrt{P_{\mathrm{H_2}}}}\right)+1\right)^{1/7}. \tag{4.30}$$

The novelty in Eqn. 4.30 is that the partial pressures of water vapor and hydrogen are now directly included in the expression. This gives the equation more predictive power to describe what goes on in the reactor. An approach similar to that used by Sehested *et al.* could prove useful in predicting sintering rates for other systems than the nickel based steam reforming catalyst.

The increased sintering rate of Ni-based catalysts in environments containing even small amounts of H_2O, $< 3\%$, have been proven in reactor experiments [39]. Increased sintering rates by adsorption of species from the surrounding atmosphere have been observed for Cu systems where Cu_3S_3 complexes on the surface of Cu particles move mass [77], and on Pt where Pt-H is believed to be the mass transporting specie [78].

As Eqn. 4.30 directly contains the pressure factors, it provides a route for comparing the low pressure in situ TEM data to the ambient pressure

reactor data as in e.g. [79]. However, as the ambient experiments were carried out with a catalyst of higher loading than the catalyst used in the in situ TEM study, the initial particle diameters were larger. Further, the sintering periods in the ambient pressure experiments were much longer than experimentally feasible for in situ TEM experiments. These facts may result in discrepancies between the obtained mean particle diameters.

Chapter 5

In Situ TEM Studies of Supported Metal Catalysts

Many attempts have been made to understand the microscopic details of catalyst sintering. Most of the previous studies have involved the use of transmission electron microscopy [80], chemisorption techniques [49] and more recently, scanning tunneling microscopy [81, 82]. Common to most of these techniques is that they involve measurements of the catalyst before and after reaction. Techniques like X-ray diffraction and extended X-ray absorption fine structure have been used as in situ techniques to study sintering, but these techniques give averages over the entire sample rather than focus on local phenomena and particle size distributions. To observe the sintering mechanism of metal individual particles in complex systems like industrially relevant catalysts under reactive gases, in situ TEM is well-suited.

Previous in situ TEM studies by Baker *et al.* have shown good agreement with the Gruber formula for iron particles larger than d=20nm on a graphite support [83]. More recently Jak *et al.* have shown that defects have a significant influence on the diffusion of small palladium particles on a TiO_2 support using STM. Later a similar effect was observed by Wallace *et al.* for Au on TiO_2 and mixed SiO_2-TiO_2 [84] also using STM. Recent in situ TEM studies of palladium particles on an alumina support by Liu *et al.* showed that palladium particles sinter by particle migration and coalescence, but that such sintering was not significant at temperatures below 973K [85]. The earlier results show rather complex interaction between metal particles and support, well-suited for in situ TEM studies.

In this work, a nickel-based steam-reforming catalyst has been studied as the particles grow at elevated temperature in a reactive gas. The aim of the experiments is by direct observation in the in situ TEM to examine the predictions from Gruber's formula [60], i.e. the random walk motion of the metal particles and the d^{-4} scaling of the particle diffusion coefficient. The Gruber formula has been carried on into the formula presented by Sehested *et*

al. [11] describing the specific sintering of Ni-based steam-reforming catalysts in industrial steam reforming reactors. Hence analyzing the in situ TEM data in terms of the Sehested equation, will shed light on the representability of the in situ TEM observations as representative for sintering of an industrial steam-reforming catalyst. The evolution of the particle size distribution is also studied as it has been suggested to be representative of the sintering mechanism.

5.1 Catalyst Preparation

A low surface area $MgAl_2O_4$ carrier ($5m^2/g$ by BET) was used to prepare a 1wt% $Ni/MgAl_2O_4$ catalyst for in situ transmission electron microscopy studies. The catalyst was prepared by wet impregnation with a nickel formiate precursor. After impregnation the catalyst was calcined converting the nickel precursor to nickel oxide. A low surface area carrier was chosen to ease the TEM observations of individual metal particles and sintering events, and to minimize the influence of support morphology. Primarily flat regions were chosen for observations to further minimize the influence of support morphology.

Earlier it has been shown that average particle size depends only weakly on the nickel loading. Hence the results obtained using a 1wt% $Ni/MgAl_2O_4$ should be applicable to all $Ni/MgAl_2O_4$ catalysts. Sehested *et al.* showed that over a 5-fold variation in metal loading, the average particle diameters fell within a narrow range of 27-37nm [41] after sintering for more than 700 hours. Further, sintering of the $MgAl_2O_4$ support should be limited due to the low surface area of the support. The low surface area of the support material also minimized the effect of the pore sizes of the support. When using a crushed low surface area support, almost only plates are observed. The metal particles are thus allowed to grow freely in a 2-dimensional environment, without interactions with other plates. Pore geometry has been suggested to have a significant influence on the sintering of supported metal particles [42]. Metal particles in pores have a higher coordination to the support and can become trapped on the support. Similar effects have been suggested at the intersections of support plates.

Fig. 5.1 shows a secondary electron SEM image of the catalyst sample, before crushing, used for the in situ TEM studies. The support consists of large platelets of $MgAl_2O_4$ of μm dimensions along with smaller agglomerates. The image also shows the porous system of the support.

After crushing the catalyst sample to the state in which it was deposited, it was tested with XRD to determine which phases were present. Fig. 5.2 shows the x-ray diffraction spectrum. Analysis of the spectrum using X'pert HighScore from PANalytical B. V. shows that the sample is more than 98% $MgAl_2O_4$. The sample contains small amounts of α-Al_2O_3. The low amount

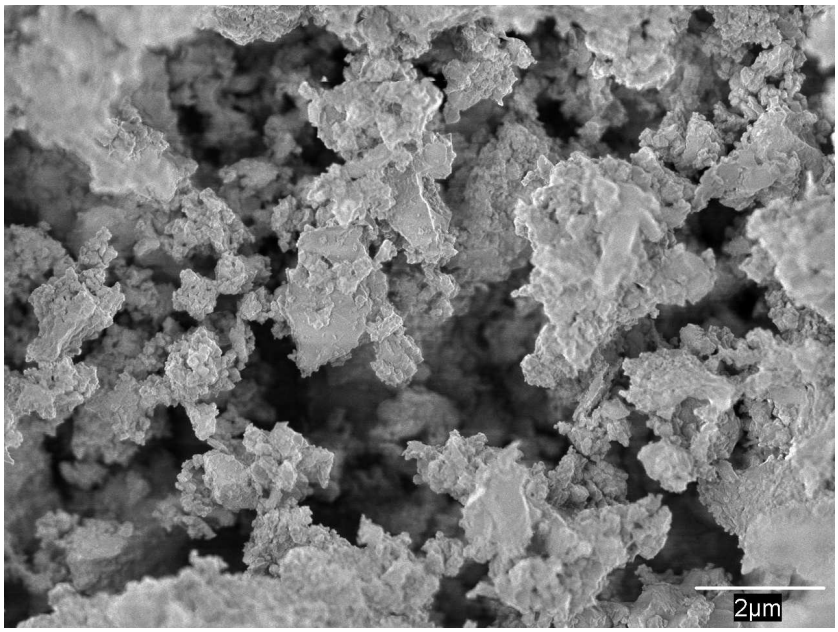

Figure 5.1: SE scanning electron micrograph of the catalyst used for the in situ studies. The high temperature calcination has resulted in large platelets of $MgAl_2O_4$.

of nickel oxide is not observed by XRD.

5.2 In Situ TEM Experiments

The in situ TEM studies were carried out on the catalyst described in Section 5.1. For the in situ TEM studies, the Philips CM-300 FEG TEM described in Chapter 3 was used [31]. All images and movies were acquired using the low-light camera from Tvips GmbH to minimize electron beam exposure of the sample [86] while optimizing the sampling rate.

The catalysts were sintered in a simulated reaction environment containing only H_2O and H_2. The model that will be used later only includes these gases and including hydrocarbons would unnecessarily increase the complexity. The effect of hydrocarbons in the atmosphere will not be discussed here. Further, the atmosphere and temperature in a steam reforming reactor change through the bed. Hence in an industrial reactor, the sintering rate will be different through the bed. In the current experiments, isothermal sintering is assumed due to the small dimensions of the TEM grid and the small amount of catalyst used.

To minimize the influence of contaminants in the H_2, Alphagaz 2 with low levels of contaminants from Air Liquide was used, see Table 5.1. The H_2O

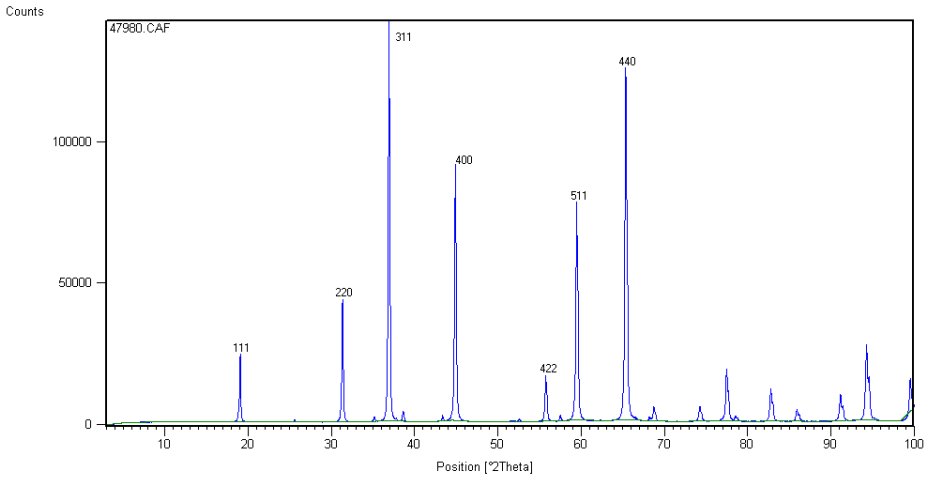

Figure 5.2: XRD spectrum of the 1wt%Ni/$MgAl_2O_4$ sample used in the in situ TEM studies.

supply on the in situ system was cleaned by consecutive freeze/pump/thaw cycles. The H_2O container was frozen by submerging it in liquid nitrogen. After ca. 10 minutes all the water in the container was frozen and the container could be evacuated without removing the H_2O. As the iced melted, the container was closed and all the ice left to melt. When all ice was melted the procedure was repeated. The cleanliness of the gases was monitored online using mass spectroscopy. When introducing the hydrogen for the reduction period, there was a peak in the H_2O signal after which the signal fell again. As the H_2O signal falls off again right after H_2 introduction, this could mean that the contamination comes from a previous experiment. During all in situ experiments the mass spectrometer was running to monitor the gas cleanliness online. Fig 5.3 shows a mass spectrum from a typical in situ TEM experiment. The first ca. 0.25 hours show the background in the in situ cell. At ca. 0.25 hours the sample holder is inserted into the microscope giving an increase in all the components present in the ambient atmosphere. At ca. 0.75 hours, hydrogen is introduced and the reduction period is started. At ca. 3.7 hours, the hydrogen pressure is decreased and at ca. 4 hours H_2O is introduced. After H_2O introduction, slight variations in all masses are observed when the pressures are adjusted. The in situ experiments are conducted in the period from ca. 4-9.5 hours with constant ion currents from all masses. After the experiment, the in situ cell is evacuated (9.5-10 hours) after which the microscope is switched back into high vacuum mode giving the peak at ca 10 hours.

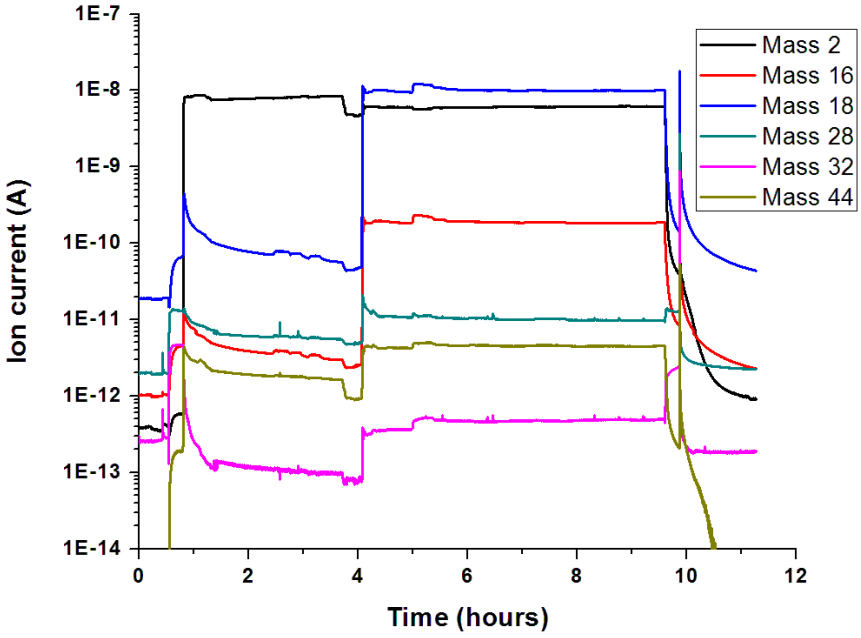

Figure 5.3: Mass spectrum from a typical in situ TEM experiment.

	H_2O	O_2	C_nH_m	CO	CO_2
Mass	18	32	16(CH_4)	28	44
Alphagaz 2 (in ppm)	<0.5	<0.1	<0.1	<0.1	<0.1
H_2O	-	-	-	<0.1	<0.1

Table 5.1: Data for Alphagaz from Air Liquide and from the purified water.

5.2.1 The Experiments

Three kinds of in situ TEM experiments were carried out. In two sets of experiments the sample was treated in the microscope without the electron beam on, and in one set of online experiments the electron beam was on at all times.

The first set of experiments, the parameter experiments, were designed to investigate the influence of various parameters on the sintering rate, i.e. partial pressures of water vapor and hydrogen, and the effects of temperature. The aim was to study how these parameters affect the mean particle diameter and the particle size distribution. The results of these experiments will be discussed in the context of the Sehested formula to determine how well

treatments in the in situ TEM emulate the industrial reactor environment. As the electron beam was on the sample only during the short period of image acquisition the effects of the beam are expected to be minimal.

The second set of experiments, offline sintering experiments, focused on changes in mean particle diameter and particle size distribution after a fixed sintering time. From these experiments the amount of sintering can be determined without the influence of the electron beam. The experiments were carried out in atmospheres similar to those used for the online experiments described below. These experiments were also designed to show if the observations in the third set of experiments were in agreement with data obtained without the presence of the electron beam and if the development in the particle size distributions could be explained based on the observation in the online experiments described below. The results can also be compared with the results of the first set of experiments where the electron beam was on the sample only during the intervals of image acquisition.

The third set of experiments involved online monitoring of particle mobility. Here the movement of the particles was monitored as they were exposed to the operating conditions. From these experiments, the reliability of the sintering mechanisms proposed based on particle size distributions can be studied, and in the case of particle migration and coalescence, diffusion rates of the metal particles can be estimated.

For all experiments, the sample was crushed using a mortar and pestle and dispersed in dry form on a stainless steel TEM grid. Stainless steel grids were used as they were expected to be most resistant to oxidation under the extreme operating conditions. After mounting the sample in the TEM holder, the holder was inserted in the TEM, and hydrogen was introduced into the in situ chamber. After a stable pressure of 3mbar hydrogen was reached, the temperature was ramped up to 773K at ca. 50K/min. 773K was chosen as the reduction temperature based on the literature [11, 49].

To get an estimate of the reduction period needed to reduce the NiO precursor to metallic Ni, electron energy-loss spectroscopy (EELS) of a 22wt% $Ni/MgAl_2O_4$ sample was used to monitor the oxidation state of Ni in the sample during the reduction period. A 22wt% Ni sample was chosen over the 1wt% Ni sample for the EELS measurements because the intensity of the Ni edges are higher and therefore shorter acquisition times were needed to acquire good statistics in the spectrum.

Electron energy-loss spectra were acquired for metallic Ni (ion thinned Ni foil, Goodfellow) and NiO (Sigma-Aldrich) as references. Both Ni foil and NiO powder were 99.99% purity. The electron energy-loss spectra were recorded in image mode, meaning that the microscope was set to show an image in the viewing screen. The spectra for the NiO reference and the fresh catalyst were acquired in UHV at ca. 300K. Spectra of the catalyst were also acquired as a function of time exposed to the reduction environment. The energy-loss spectrum of the reduced catalyst shown in Fig. 5.4 is acquired

30 minutes after the sample reached 773K ramped up at 50K/min in 3mbar hydrogen. The spectrum of the Ni reference was acquired after 30minutes of exposure to the reduction environment.

The background was subtracted from the spectra using a power-law extrapolation of an energy window approximately 20eV wide in the region approx. 10eV in front of the nickel L_3 edge. After background subtraction, the spectra were corrected for multiple scattering using the Fourier-ratio method [20] and the energy-loss was calibrated at the onset of the L_3 edge and the energy dispersion on the difference between the L_3 and the L_2 edges. The spectra were all normalized in intensity at 889eV which is in the region past the Ni L_2. The intensity in the background subtracted L_3 edge was integrated 1eV on each side of the maximum value to obtain the total number of counts in the edge.

The oxidation state of nickel in the catalyst was estimated based on the ratio of the integrated intensity of the Ni L_3 peak for the catalyst and for the metallic nickel reference. The intensity in the Ni L_3 edge decreases as the sample reaches the metallic state due to the change in the chemical environment, see Fig. 5.4 [87]. In relation to Eqn. 3.10, the change in the chemical environment results in a more well defined density of final states for the oxide, the last term in Eqn. 3.10. The valence states are more discrete in the oxide than in the metal. This gives rise to well defined peaks in the energy-loss spectrum known as *white lines*. For the as-prepared catalyst, Ni is present as NiO, the EELS spectrum of the catalyst matches closely that of the NiO reference. In the reduced state, the EELS spectrum of the catalyst matches closely that of the metallic Ni reference.

Fig. 5.5 shows the intensity of the integrated L_3 edge in the catalyst normalized to the value found for the metallic Ni reference vs. time. t=0 minutes is the time that the sample holder reached the reduction temperature (773K). The final oxidation state of Ni is obtained after ca. 25 minutes of reduction after which the $L_3(cat.)/L_3(ref.)$ intensity ratio reaches that of the nickel reference. Richardson and Crump estimate that 50-60% of Ni is reduced when reducing a 17wt% Ni/SiO_2 catalyst in pure hydrogen [43], but their reduction temperature, 653K, is somewhat lower than used for the present studies. The $L_3(cat.)/L_3(ref.)$ ratio of the reduced catalyst reaches a value close to 1 so an almost complete reduction of the catalyst is expected. All particle sizes and mean diameters are determined at least 1 hour after 773K was reached. The difference between the catalyst and reference spectra are most probably due to differences in sample thickness.

The EELS measurements show that a 22wt% $Ni/MgAl_2O_4$ catalyst is reduced to the metallic state after 25 minutes in hydrogen at 773K. Hence it is concluded that the 1wt% $Ni/MgAl_2O_4$ catalyst is reduced and the particles monitored are metallic nickel. High-resolution TEM images also confirm that the nickel particles are metallic. The image shown in Fig. 3.9 is acquired under conditions similar to those where the energy-loss spectra were acquired

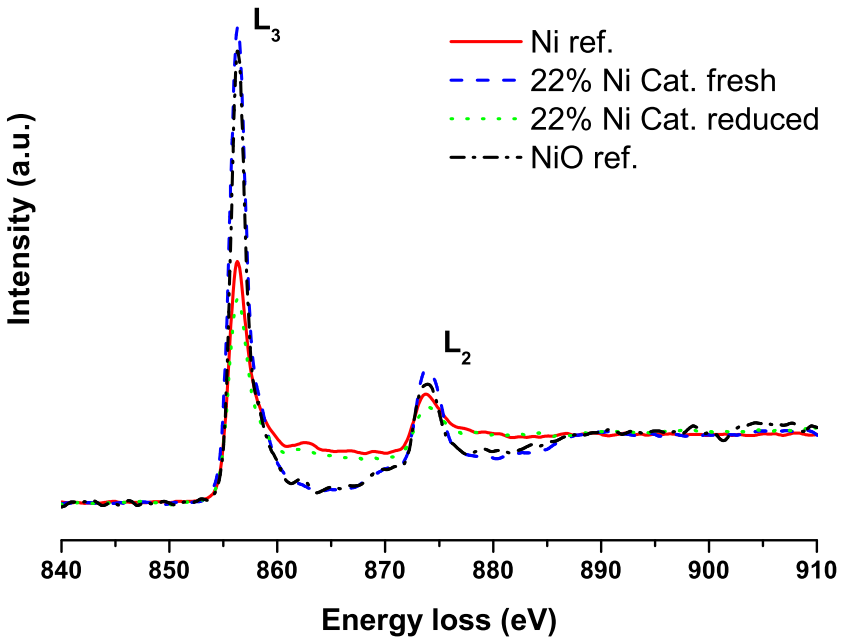

Figure 5.4: EELS data for nickel and nickel oxide references and the 22wt% Ni catalyst before and after reduction. In the fresh state the EELS spectrum of the catalyst matches that of the NiO reference and in the reduced state, that of the metallic Ni foil reference. All spectra have been subtracted for background and scaled to the intensity at 889 eV.

under and the lattice spacings match those of metallic nickel. Treatment in pure hydrogen does not significantly affect the mean particle diameter, see Table 5.3. Even at 1023K, the mean particle diameter is close to the diameter obtained after the reduction period. Therefore reducing the sample further at 773K will not change the results of the experiments. Even in the presence of water vapor at 773K the mean particle diameter remains almost constant, see Table 5.3. After reduction, the mean Ni particle diameter was in several experiments shown to be ca. 3.2 ± 0.2nm, and this number is used as d_0 in the calculation in Section 5.4.1.

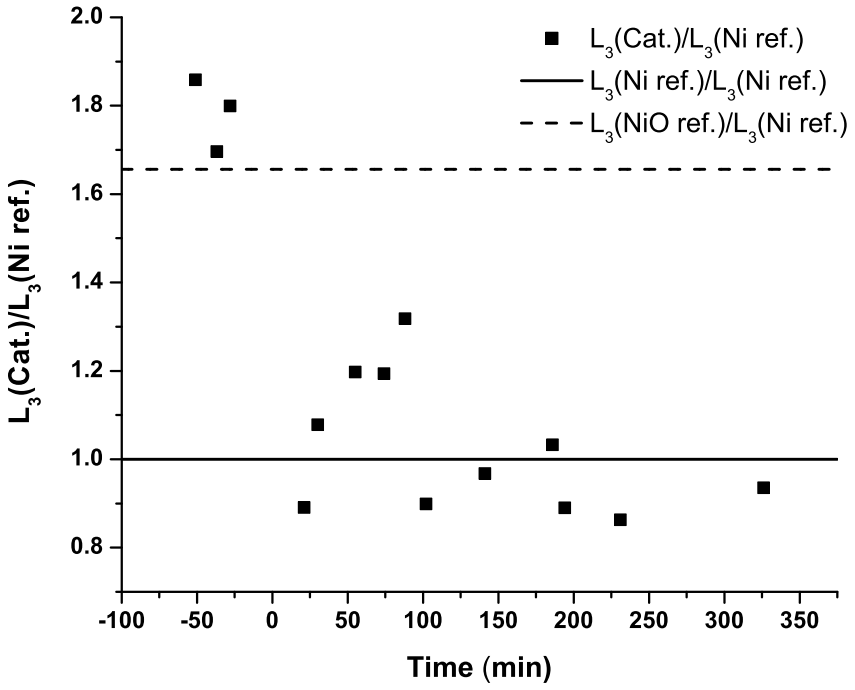

Figure 5.5: Peak intensity ratio vs. time. The final oxidation state of Ni is the same 25 minutes after the reduction was started as it is after more than 5 hours of reduction. In the intermediate period, no significant change in the ratio is observed.

5.3 Parameter Experiments

The parameter experiments were designed to give an indication of the rate of sintering under a given set of operating conditions (partial pressures of H_2 and H_2O, total pressure, and temperature). Different combinations of partial pressures and temperatures were chosen to investigate the effect of the individual parameters. The combinations of environments were chosen based on the environment encountered in a steam reforming reactor. The main factors influencing the sintering of steam reforming catalysts are the partial pressures of water and hydrogen and the temperature in the reactor. Hence variations in these parameters from a mild set of conditions, low partial pressure of water and low temperature, to a severe set of conditions, relatively high partial pressure of water and high temperature, allows for comparison with the Sehested formula over a wide range.

After sample mounting and reduction treatment as described in Section

5.2, the hydrogen pressure was decreased to the hydrogen partial pressure in the sintering environment while keeping the temperature constant at 773K. When temperature and total pressure were again stable, H_2O was introduced while keeping the temperature constant at 773K. After the sintering partial pressures were adjusted and stabilized the temperature was ramped up at ca. 50K/min to the sintering temperature. During the temperature ramp, the sample was highly mobile due to drift in the sample, the TEM grid, and the sample stage. The drift is due to the difference in the thermal expansion coefficients of these parts. This period is referred to as the transient period. In this period the sample is too mobile to image even at short acquisition times (<100ms). Time t=0 was chosen as the time when the temperature reached the sintering temperature, not the time when the sample was stable. After the drift had reached an acceptable level for image acquisition, ca. 20 images were acquired. After a certain time interval another 20 images were acquired, and so on. Between consecutive image series the valve to the electron gun was closed and the sample was not exposed to the electron beam. Each image series was acquired on different areas of the samples, i.e. areas without prior exposure to the electron beam. The particle size distributions, Figs. 5.6 and 5.7, and mean particle diameters were then determined from each set of images as described below. The time stamp, i.e. the time used to log the mean diameter in Figs. 5.8 and 5.9, for each set of images was determined as the middle of the period over which the images were acquired. This period where the images were acquired, is in every case shorter than the time interval between consecutive image sets.

Particles were counted and measured using Image-Pro Plus from Media Cybernetics. Particle outlines were determined and from these the particle diameters where extracted approximating the particles as spheres. This approach seems reasonable since the Wulff point of the nickel particles is most often found to be above the surface of the support, see e.g. Fig. 3.9. This was also the conclusion of Hummelshøj for a variety of metal oxide supports including $MgAl_2O_4$ [88]. The measured particle diameters were put into bins 1nm wide for the particle size distributions. More than ca. 300 particles were counted and measured for every set of images. As the basic shape of the particle size distributions is discernible in all cases, this amount of particles seems enough for convergence of the particle size distribution. Some particles may not have complete spherical geometry, but are assigned a diameter of an approximating sphere. Assuming that the nickel particles are spheres is justified by the small difference in surface energies of the low-index facets, see Table 5.2.

Figs. 5.6 and 5.7 show the particle size distributions when sintering in 5% H_2O in H_2 at 873K and 973K obtained from such images. The particle size distribution at 873K does not change significantly with time. Only a small increase in the number of particles at the far right of the distribution is observed. However the full-width-at-half-maximum is unchanged over 433

Facet	Surface energy (J/m^2)
(111)	1.952
(110)	2.237
(100)	2.166

Table 5.2: Surface energy for nickel [89].

minutes of sintering. The distribution stays centered at around 2.5nm. Also the upper limit of the size distribution stays at around 10nm over the period. From Fig. 5.8 it is seen that the mean particle diameter changes by only about 20% over ca. 420 minutes and that at 873K the influence of 5% water vapor in the atmosphere is almost insignificant for the first 7 hours of sintering.

The shape of the PSD's obtained at 973K changes significantly, and the mean particle diameter increases ca. 120% after 7 hours of sintering. Whereas the initial distribution is a sharp peak around ca. 2.5nm the distribution becomes increasingly wider and more ragged, after 423 minutes under the sintering conditions, the full-width-at-half maximum has doubled, see Fig. 5.7. The increase in mean particle diameter when sintering in 5% H_2O in H_2 is also reflected in Fig. 5.9 showing the mean particle diameter as a function of time with and without H_2O in the atmosphere. An important observation however is that the lower limit of the PSD does not change. Therefore small particles are present throughout the sintering period. Contrary to sintering experiments carried out at 873K, the upper limit of the distribution changes to around 14nm, so larger particles are formed while still maintaining a significant population of small particles. Hence a large fraction of particles does not participate in the initial sintering. For the experiments including H_2O in the atmosphere, the experimental data has been fitted using the model of Sehested [11]

$$\frac{\bar{d}}{\bar{d}_0} = \left[\left(\frac{C \cdot X \cdot t}{\bar{d}_0^7 (1-X) A} \right) \left(\frac{P_{H_2O}}{\sqrt{P_{H_2}}} \right) + 1 \right]^{1/7} \tag{5.1}$$

as explained in Chapter 4. The values of the constant C are given in Appendix A.

An increase in particle diameter is also observed for the experiments carried out in pure H_2. The reason for this can be impurities in the gas or other processes than assumed in Eqn. 5.1.

5.4 Offline in situ TEM Experiments

The offline experiments were treatments of the catalyst sample in the in situ TEM over a 5 hour period without exposure to the electron beam. Sample

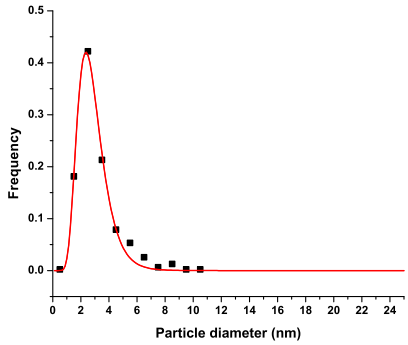

(a) PSD after reduction.

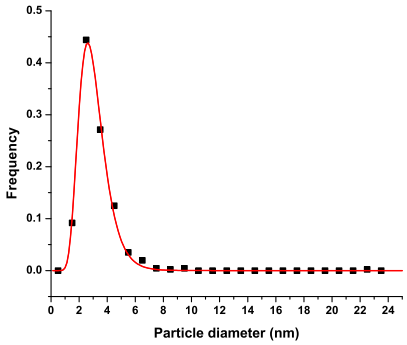

(b) PSD after 65 minutes of exposure.

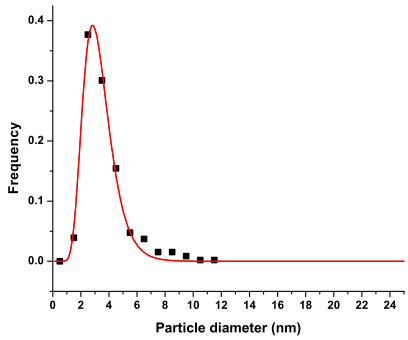

(c) PSD after 147 minutes of exposure.

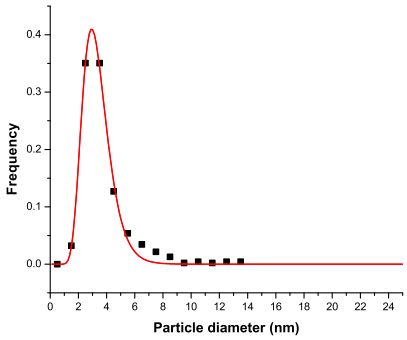

(d) PSD after 253 minutes of exposure.

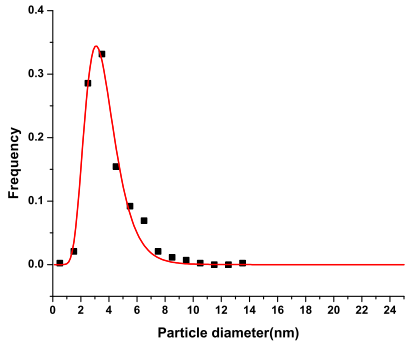

(e) PSD after 339 minutes of exposure.

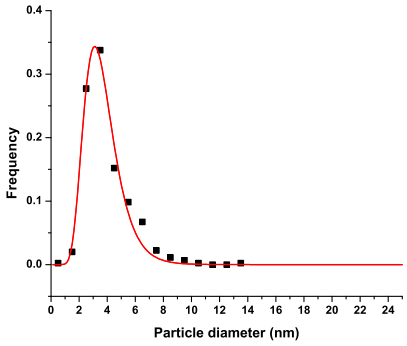

(f) PSD after 433 minutes of exposure.

Figure 5.6: Particle size distributions at 873K in 5% H_2O/H_2, total pressure is 1.5mbar, as a function of exposure time to H_2O/H_2. The parameters of the log-normal fits are given in Table A.1.

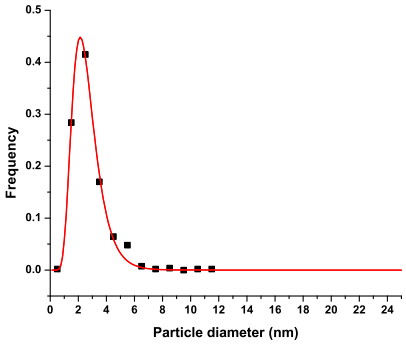

(a) PSD after reduction.

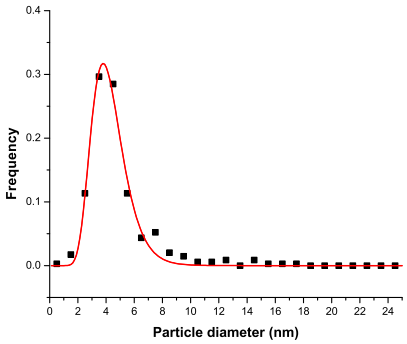

(b) PSD after 110 minutes of exposure.

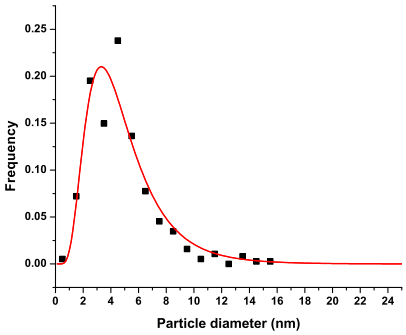

(c) PSD after 177 minutes of exposure.

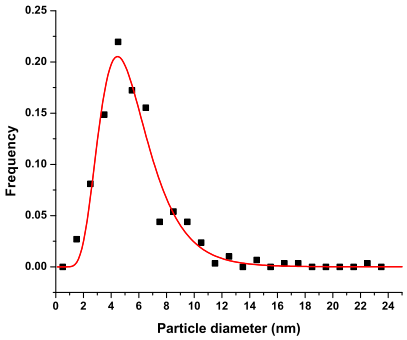

(d) PSD after 252 minutes of exposure.

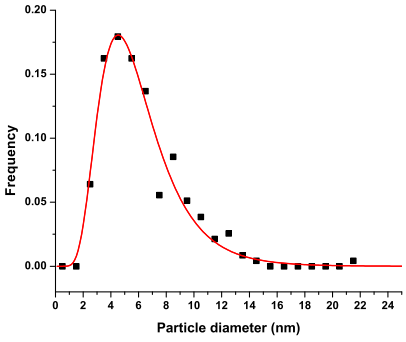

(e) PSD after 328 minutes of exposure.

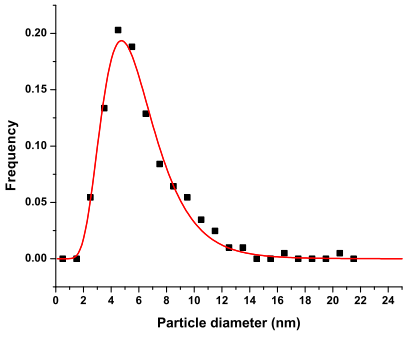

(f) PSD after 423 minutes of exposure.

Figure 5.7: Particle size distributions at 973K in 5% H_2O/H_2, total pressure is 1.5mbar, as a function of exposure time H_2O/H_2. The parameters of the log-normal fits are given in Table A.2.

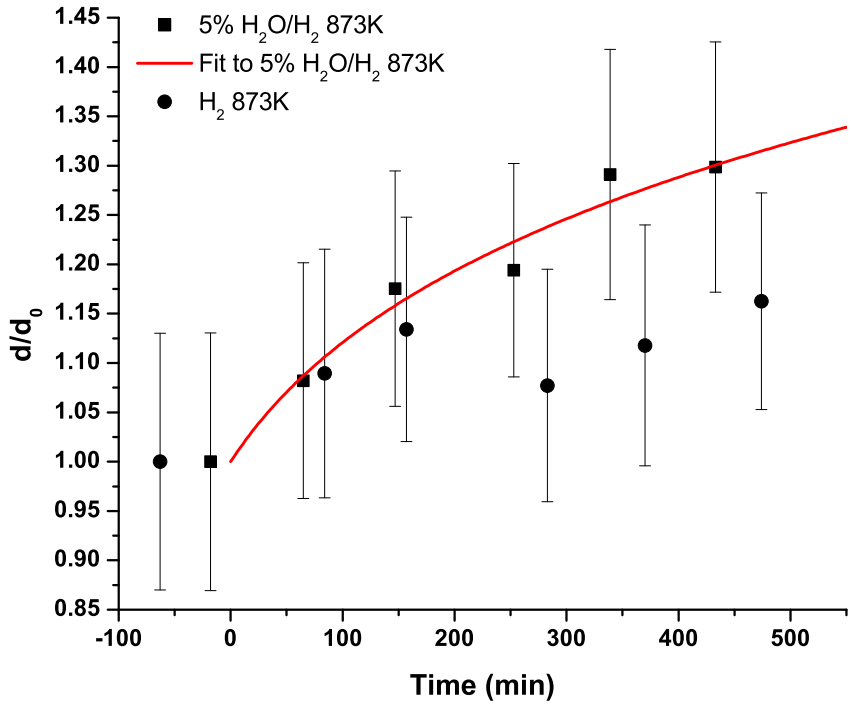

Figure 5.8: Normalized mean particle diameter vs. time at 873K for two different gas compositions. The vertical lines indicate the width of the distributions. The solid line shows the fit using Eqn. 5.1 for the experiment done in 5% H_2O in H_2 in the in situ TEM. The value of the constant C obtained from this fit is found in Table A.3.

preparation and reduction procedure was the same as outlined above. After the reduction period, a series of images were acquired to determine PSD's and mean particle diameter. After acquisition of the initial image series, the hydrogen pressure was decreased at constant temperature and water vapor was introduced, still at constant temperature. After stabilization the temperature was ramped up to the sintering temperature at ca. 50K/min. When the sintering temperature was reached, the sample was left in the TEM for a period of 5 hours without exposure to the electron beam. After the 5 hour sintering treatment a final set of images was acquired to determine the final particle size distributions and mean particle diameters. The measured diameters have been put into bins 1nm wide.

Experiments were carried out at three different temperatures in three different environments. Since no significant sintering occurred at 1023K in

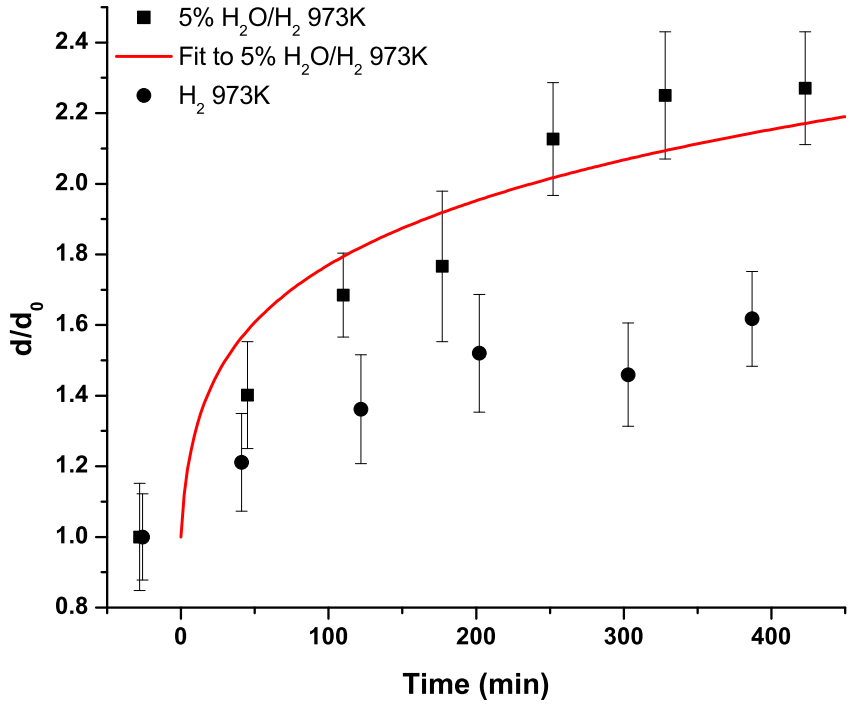

Figure 5.9: Normalized mean particle diameter vs. time at 973K for two different gas compositions. The vertical lines indicate the width of the distributions. The solid line shows the fit using Eqn. 5.1 for the experiment done in 5% H_2O in H_2 in the in situ TEM. The value of the constant C obtained from this fit is found in Table A.3.

pure H_2, see Table 5.3 and Figs. 5.10 and 5.12, no experiments were carried out at lower temperatures in pure hydrogen since even less sintering was to be expected. At 1023K in 9:1 H_2O/H_2, the stainless steel TEM grids started oxidizing already from the beginning of the experiment and long whiskers of Fe_xO_y were formed. These whiskers made it impossible to distinguish the catalyst material from the oxidized grid and no meaningful particle size distributions could be determined. Hence this experiment was not carried out either. The conditions under which particle size distributions and mean particle diameters were successfully determined are shown in Table 5.3 together with the mean particle diameter after reduction (before sintering) and after reduction and sintering.

Figs. 5.8 and 5.9 show that not much sintering occurs in pure hydrogen, not even when the temperature was increased to 1023K. However, when wa-

	T=773K	T=923K	T=1023K
0:1 P_{tot}=2mbar	B: N/A A: N/A	B: N/A A: N/A	B: 3(1) A: 4(2)
1:1 P_{tot}=4mbar	B: N/A A: 4(3)	B: 3(1) A: 4(2)	B: 3(1) A: 10(5)
9:1 P_{tot}=10mbar	B: N/A A: 4(2)	B: 3(2) A: 6(3)	B: N/A A: N/A

Table 5.3: Mean particle diameters (number averaged) from the offline experiments after 5 hours of sintering. The first column shows the ratio of H_2O to H_2 and the total pressure. B and A designates mean particle diameter Before and After sintering. The standard deviations of the distributions are given in parenthesis. In all cases the mean particle diameter after the reduction period is close to 3nm.

ter vapor was added to the atmosphere, the sintering increased significantly, see Table 5.3 as described in [11, 39]. Not just the mere presence of water vapor effects the sintering, but also the partial pressure. Particles were observed to grow to larger diameters when a higher partial pressure of water is present in the sintering atmosphere, as is seen in Table 5.3. This is also predicted by the formula of Sehested *et al.* [11] and has been reported earlier by Bartholomew [39]. At low temperatures, ca. 773K, no significant sintering was observed after 5 hours. A similar result was observed after 50 hours of sintering by Sehested *et al.* [11] who observed a mere 17% increase in mean particle diameter for a 9.5wt% Ni/Al_2O_3 catalyst after 50 hours at 773K in 1:1 H_2O/H_2 at 1bar total pressure. Comparing the present in situ TEM results under a 1:1 steam to hydrogen ratio at 923K with the results in [11], the same degree of sintering was not observed. Where Sehested *et al.* observed a 71% increase in mean diameter, the in situ TEM observations showed only a 40% increase in mean particle diameter. However there is a big difference in the sintering time, metal loading and initial nickel particle diameter. The particles both before (the value of $\bar{d}_0$ in Eqn. 5.1) and after sintering are much larger in the work of Sehested *et al.* [11]. Thus each system will produce different values of C in Eqn. 5.1. Particle diameters derived for the in situ TEM experiments using values of C determined from high pressure experiments are expected to be to small as the initial particle diameters in the in situ TEM experiments are much smaller than in the high-pressure experiments. The mean particle diameters determined from TEM images are number averaged mean particle diameters whereas the data reported by Sehested *et al.* are determined using sulfur adsorption giving surface averaged mean particle diameters. These two averages are given by

$$\bar{d}_n = \frac{\sum n_i d_i}{N} \tag{5.2}$$

$$\bar{d}_s = \frac{\sum n_i d_i^3}{\sum n_i d_i^2} \tag{5.3}$$

Due to the assumptions behind the Sehested formula, the distribution stays log-normal, the formula can be used for both types of averages. The only difference is a change in the value of *const*. When comparing the surface averaged diameters, the increase in mean particle diameter when sintering in 1:1 steam to hydrogen ratio at 923K is 37%. This suggests either a total pressure dependence (Sehested *et al.* carried out their experiments at 1bar total pressure, the in situ TEM experiments were carried out at 4mbar total pressure), or that a steady state was not reached after 5 hours of sintering in the in situ TEM. Longer sintering experiments at low pressure could clarify this. Still, the trends in the change of the particle diameters as function of temperature and atmosphere show agreement with the Sehested model.

The shape of the Particle Size Distributions (PSD's) have in all cases been fitted to a log-normal distribution of the form

$$y = y_0 + \frac{A}{\sqrt{2\pi}wx} \exp \frac{\left[\ln \frac{x}{x_c}\right]}{2w^2} \tag{5.4}$$

with y_0 fixed at 0. A, w, and x_c are all allowed to vary until chi-square was minimized using simplex iterations in Origin from OriginLab Corporation. The values for each fit can be found in Appendix A. Fixing y_0 is justified since particles do not grow to infinite sizes. The particle size distribution has a tail on the large diameter side of the peak, both before and after sintering, consistent with the log-normal distribution as also assumed by the model of Sehested [11], see Figs. 5.11, 5.12, 5.14, 5.16, and 5.18. Figs. 5.10, 5.13, 5.15, and 5.17 show characteristic TEM images of the catalyst before and after sintering. Size distributions of Ni-based catalysts, and catalysts based on other metals, are most often found to approximate a log-normal distribution when reduced and sintered, see e.g. [41, 90]. The appearance of large particles can be the result of a few large mobile particles coalescing with other particles to form even larger particles. Thus a large number of particles may initially be immobile and not migrate. These particles only participate in the sintering events when encountered by larger migrating particles. This is contrary to earlier models where small particles are assumed to be more mobile than larger particles and hence more prone to sintering. After reaching a certain critical diameter, as a result of sintering, particles become effectively immobile [43, 50]. For the PSD's, the smallest particles measured are around 1nm, which is well below the peak in the distributions. Few features smaller than 1nm are observed on the surface of the support.

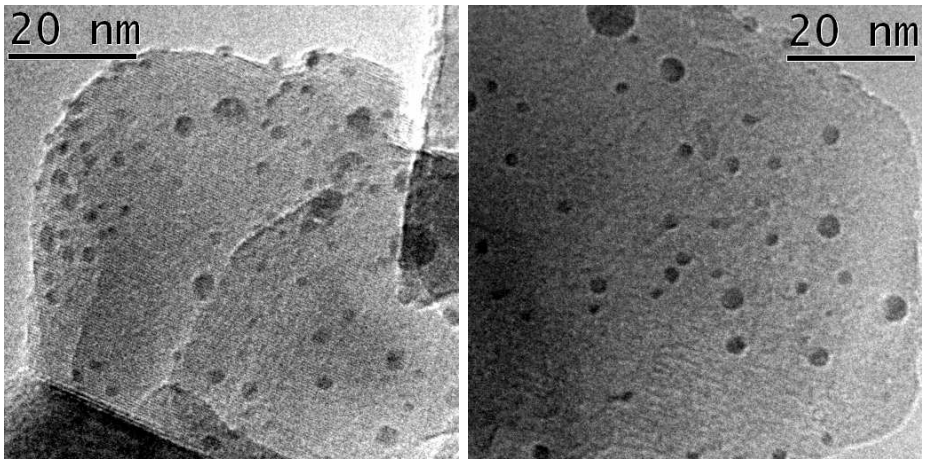

(a) Characteristic image after reduction in H_2 at 773K.

(b) Characteristic image after sintering in pure hydrogen for 5 hours at 1023K.

Figure 5.10: Representative images of $Ni/MgAl_2O_4$ from the offline experiment carried out at 1023K.

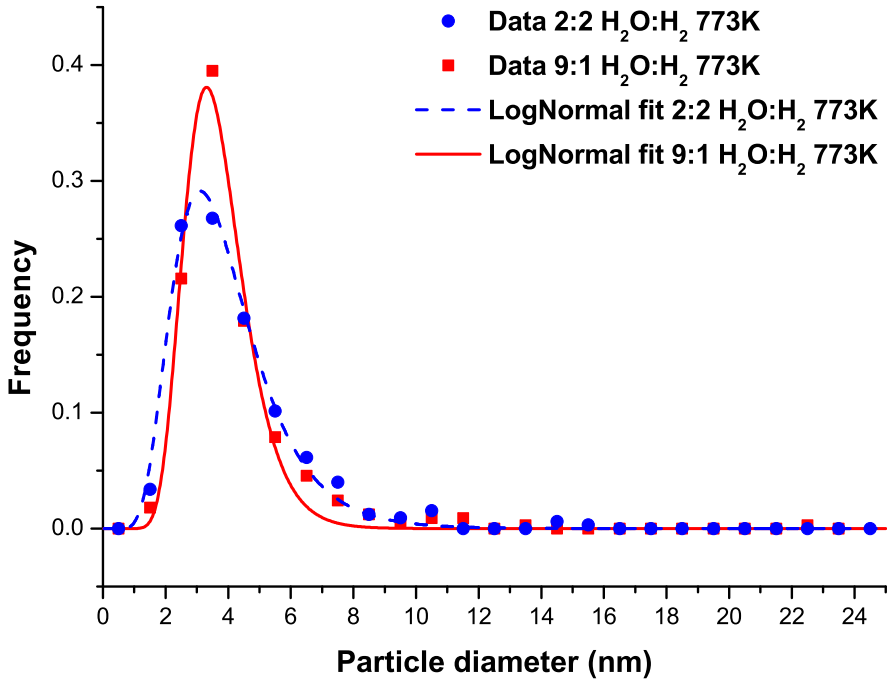

Figure 5.11: Particle size distributions of $Ni/MgAl_2O_4$ after 5 hours of sintering at 773K in 2mbar H_2/2mbar H_2O and at 773K in 9mbar H_2/1mbar H_2O. Log-normal fitting parameters are found in Table A.4

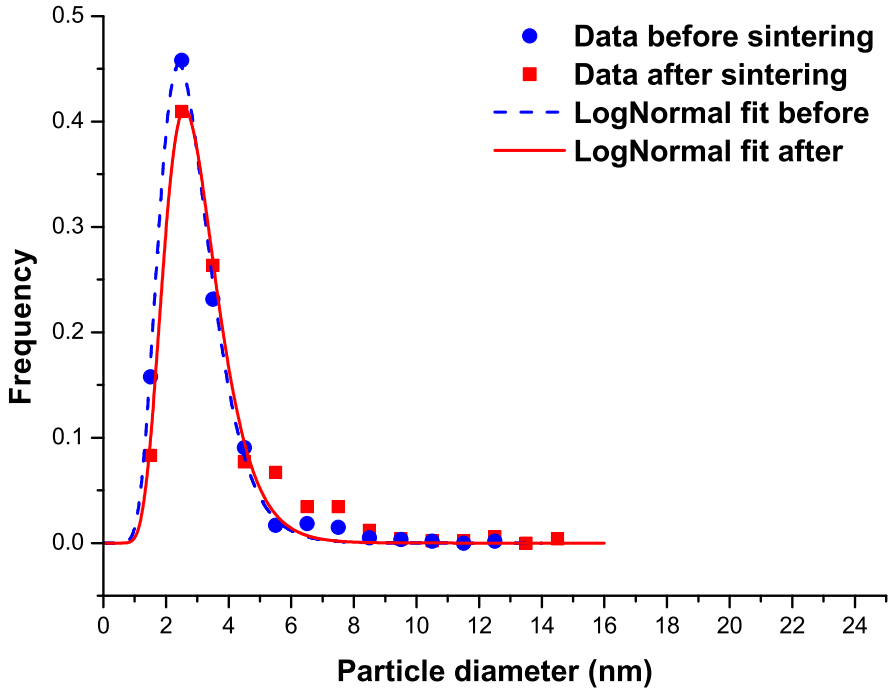

Figure 5.12: Particle size distributions of $Ni/MgAl_2O_4$ after reduction at 773K before and after sintering in 2mbar H_2 at 1023K for 5 hours corresponding to the images in Fig. 5.10. Log-normal fitting parameters are found in Table A.5.

5.4.1 Calculations of Particle Density and Coalescence Frequency

To estimate if the sintering events observed in the online in situ TEM experiments described in section 5.5 can account for the change in mean particle diameter found in the offline experiments, an estimate of how many events are expected over the duration of each experiment needs to be calculated. Given the surface area of the carrier and the metal loading, an estimate of the metal particle density can be obtained using the mean particle diameter of the reduced catalyst particles and assuming that the surface area of the support is constant. For the catalyst used in these experiments the BET surface area of the carrier is $5m^2/g$, and the metal loading is 1 wt% nickel. Hence the nickel mass per surface area is

$$\frac{1}{5m^2/g_{car}} \cdot 1 \times 10^{-2} g_{\mathrm{Ni}}/g_{car} = 2 \times 10^{-3} g_{\mathrm{Ni}}/m^2_{car} \tag{5.5}$$

where the subscript *car* refers to the carrier or support. The volume of nickel

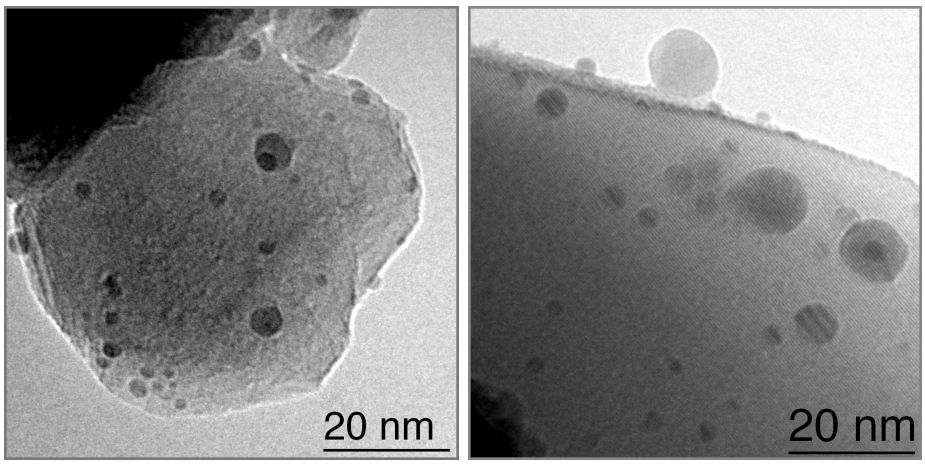

(a) Characteristic image after reduction at 773K.

(b) Characteristic image after sintering in 2mbar water vapor and 2mbar H_2 at 923K for 5 hours.

Figure 5.13: Representative TEM images of $Ni/MgAl_2O_4$ from the offline experiment carried out at 923K in 2mbar H_2O and 2mbar H_2.

per surface area is

$$\frac{2 \times 10^{-3} g_{\mathrm{Ni}}/m_{car}^2}{9 \times 10^{6} g_{\mathrm{Ni}}/m_{\mathrm{Ni}}^3} = 2.25 \cdot 10^{-10} m_{\mathrm{Ni}}^3/m_{car}^2. \tag{5.6}$$

Measurements have shown that the mean particle size after reduction for 1 hour at 773K is ca. 3.2nm, see Table 5.3. Hence it is assumed that all experiments start with a mean Ni particle diameter of 3.2nm. The volume of a non-wetting particle with a diameter of 3.2nm is

$$V = \frac{4}{3} \cdot \pi \cdot (1.6nm)^3 = 17.16nm^3 \tag{5.7}$$

and the number density of Ni particles, under the assumption mentioned above, is

$$\begin{aligned} \frac{2.25 \cdot 10^{-10} m_{\mathrm{Ni}}^3 \cdot 10^{27} nm^3/m^2}{17.16 nm_{\mathrm{Ni}}^3} &= 1.31 \cdot 10^{16} particles/m_{car}^2 \\ &= 1.31 \cdot 10^{-2} particles/nm_{car}^2. \end{aligned} \tag{5.8}$$

All PSD's were done from images acquired at 110kx magnification. At this magnification the area imaged is approx. 6000nm^2. Since in TEM, both sides of the support are always observed, the total area sampled is 12000nm^2. The number of particles in an image acquired at this magnification is

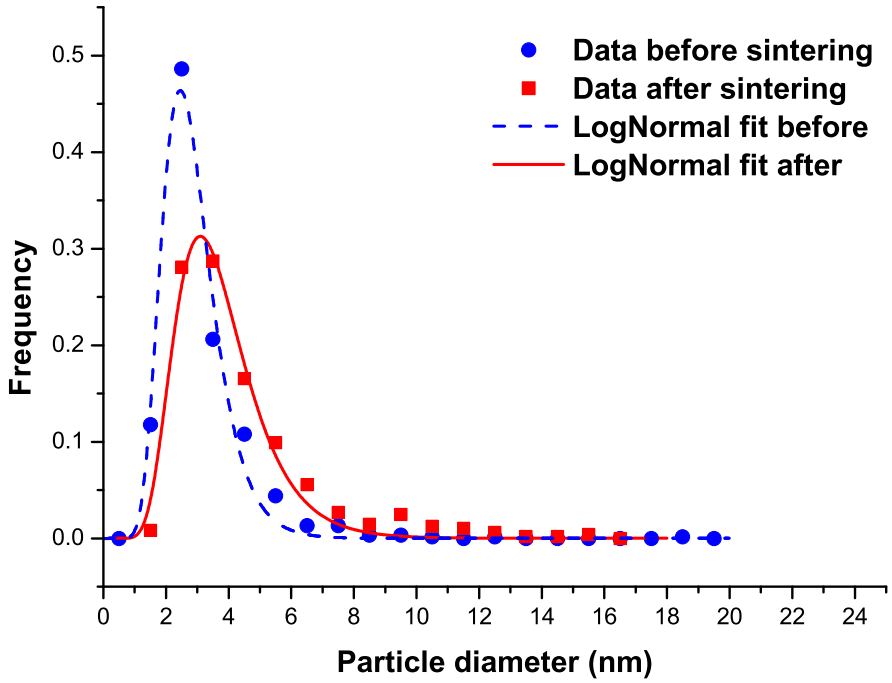

Figure 5.14: Particle size distributions of $Ni/MgAl_2O_4$ after reduction at 773K before and after sintering in 2mbar H_2O and 2mbar H_2 at 923K for 5 hours corresponding to the images in Fig. 5.13. Log-normal fitting parameters are found in Table A.6.

$$\begin{aligned} N(3.2nm, 110kX) &= 1.31 \cdot 10^{-2} particles/nm^2(car) \cdot 12000 nm^2(car)/image \\ &= 157 particles/image. \end{aligned} \quad (5.9)$$

This number might seem high based on the images of the freshly reduced catalyst. When determining the total amount of nickel over the images analyzed, the amount of nickel is lower than expected, but within a factor of two of the amount expected. One reason can be that for this calculation the average diameter has been used, not taking into account that some particles are considerably larger than average and hence consuming significantly more metal. In all of the images acquired, some empty regions are included making the imaged catalyst area smaller than the frame area. Also some support plate overlapping is unavoidable making particle counting in these regions difficult. Another possibility is that the nickel precursor is not uniformly distributed.

For the in situ TEM experiment carried out over 5 hours at 923K in 1mbar H_2 and 9mbar H_2O, the mean particle diameter changed from 3.2nm

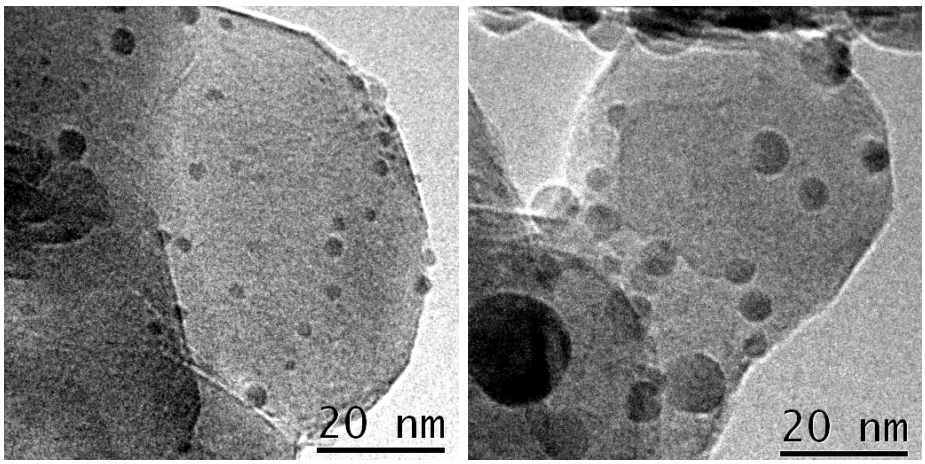

(a) Characteristic image after reduction at 773K.

(b) Characteristic image after sintering in 9mbar H_2O and 1mbar H_2 at 923K for 5 hours.

Figure 5.15: Representative TEM images of $Ni/MgAl_2O_4$ from the offline experiment carried out in 9mbar H_2O and 1mbar H_2 at 923K.

to 6.4nm. The number of 3.2nm diameter particles needed to form one 6.4nm particle is

$$\frac{(6.4nm)^3}{(3.2nm)^3} = 8particles. \tag{5.10}$$

Hence the 157 3.2nm particles become roughly 20 6.4nm particles after sintering for 5 hours. Assuming that all sintering events are coalescence events, and that particles coalesce one at a time with particles of the same size, there will be roughly 140 sintering events in a 110kx image over 5 hours. The frequency is then

$$\frac{140events}{5h \cdot 60min/h \cdot 60s/min} \approx 8 \times 10^{-3} events/s \tag{5.11}$$

or less than one coalescence event every 2 minutes in a movie acquired at 110kx. 2 minutes is roughly the duration of a typical in situ TEM movie.

5.5 Online Experiments

Classical diffusion theory predicts that particles undergo a random walk as a result of diffusion of atoms on the surface of the individual particles, with a particle diffusion coefficient that is strongly dependent on particle diameter. By examining the diffusion of bubbles in solids, Gruber found that the diffusion coefficient varies as d^{-4} [60], where d is the diameter of the

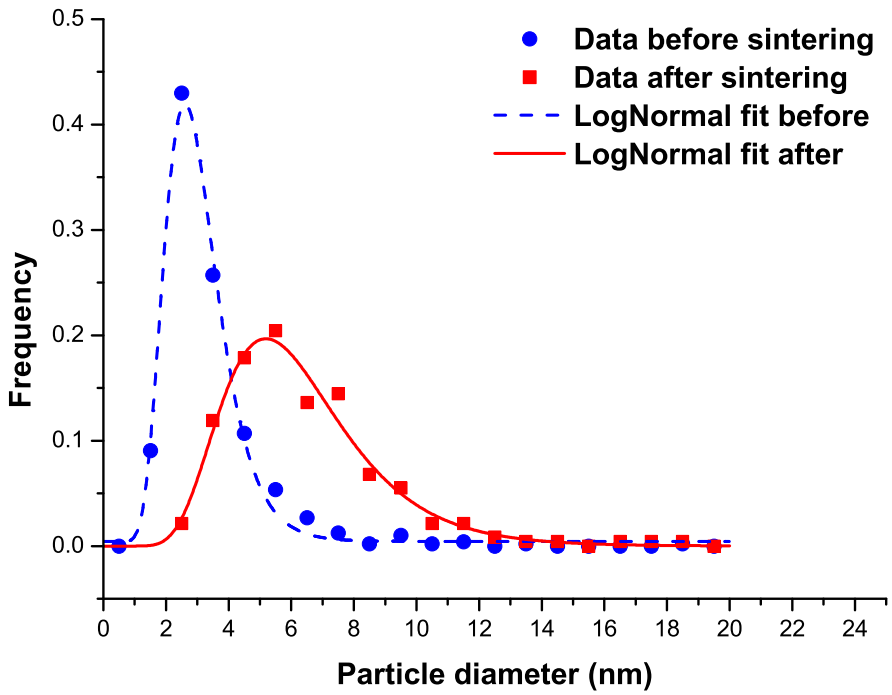

Figure 5.16: Particle size distributions of $Ni/MgAl_2O_4$ after reduction at 773K before and after sintering in 9mbar H_2O and 1mbar H_2 at 923K for 5 hours corresponding to the images in Fig. 5.15. Log-normal fitting parameters are found in Table A.7.

bubbles. This scaling law is generally applied to the diffusion of supported metal particles as well. This strong dependence of diffusion on particle size means that large particles should become virtually immobile when growing beyond a certain critical diameter. Following this theory, sintering due to particle migration can only occur when particle sizes are small. To give an example of characteristic length and time scales involved in the random walk, the average migration length, X_c, over 10s, 100s, and 1 hour for spherical Ni particles at 1023K is calculated from the expression [43]:

$$X_c = 2\sqrt{9.03 \cdot 10^{15} nm^2/s \exp\left(\frac{-159 \cdot 10^3 kJ/mole}{RT}\right)\left(\frac{0.23}{d/2}\right)^4 \cdot t} \quad (5.12)$$

where d is the particle diameter, T is the absolute temperature, and R is the universal gas constant. Values are shown in Table 5.4.

The online in situ TEM studies were carried out with the same low surface area, low loading nickel/spinel catalyst ($Ni/MgAl_2O_4$) as described in Section 5.1. For most of the in situ TEM movies the sampling rate was 2

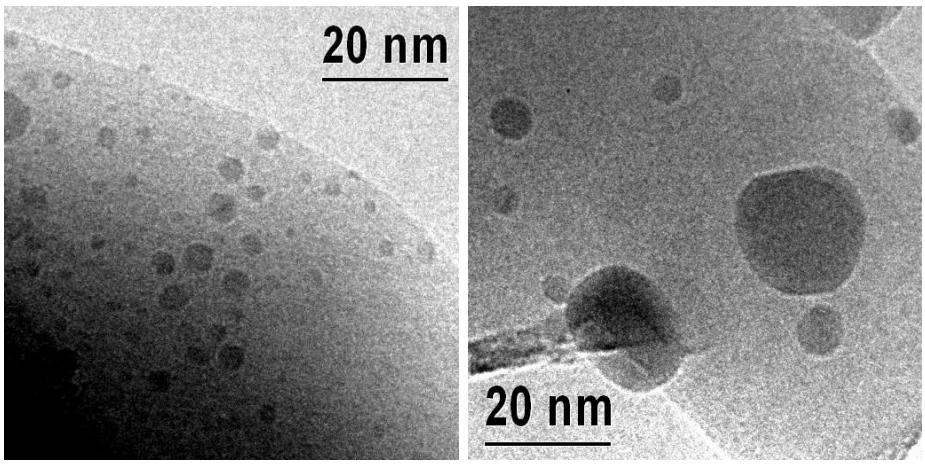

(a) Before sintering. (b) After sintering.

Figure 5.17: Representative TEM images of $Ni/MgAl_2O_4$ after reduction at 773K before and after sintering in 2mbar H_2O and 2mbar H_2 at 1023K for 5 hours.

	t=10s	t=100s	t=3600s
d=1nm	1×10^4nm	4×10^4nm	2×10^5nm
d=2nm	3×10^3nm	9×10^3nm	5×10^4nm
d=5nm	4×10^2nm	1×10^3nm	8×10^3nm
d=10nm	1×10^2nm	4×10^2nm	2×10^3nm
d=20nm	3×10^1nm	9×10^1nm	5×10^2nm

Table 5.4: Average migration lengths of nickel particles as calculated from Eqn. 5.12.

frames/s. At this rate the electron beam dose rate could be kept at around $2 \times 10^3 e^-/nm^2s$ ($3.2{\cdot}10^2 A/m^2$). At 2 frames/s most of the migration of the particles was captured. Lower frame rates might capture more mobility but at the cost of missing the individual migration/coalescence events. Using 2 frames/s was a compromise between obtaining movies of an analyzable quality while not influencing the particle mobility with the beam and still capture all the migration of the particles.

The procedure for acquiring the in situ TEM movies followed the lines of the offline experiments described in Section 5.4. The sample was reduced at 773K for at least 1 hour in 3mbar H_2 before increasing the temperature to the sintering temperature. The movies were acquired as soon as the sample drift had decreased to an acceptable level (after the transient period) for movie acquisition, ca. 1nm/s. The transient period was most often around

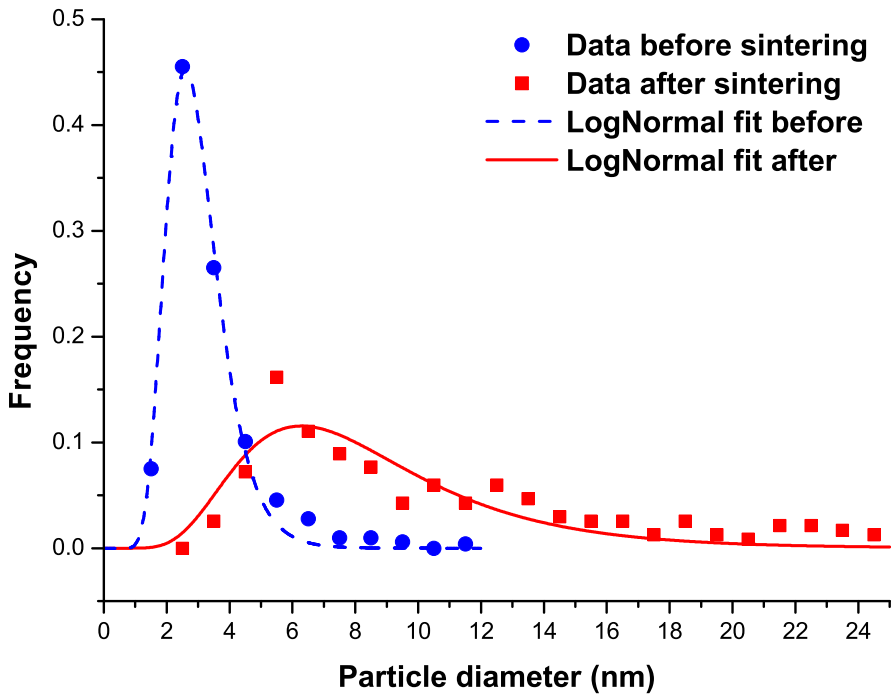

Figure 5.18: Particle size distributions of $Ni/MgAl_2O_4$ after reduction at 773K before and after sintering in 2mbar H_2O and 2mbar H_2 at 1023K for 5 hours corresponding to the images in Fig. 5.17. Log-normal fitting parameters are found in Table A.8.

10 minutes. Movies were acquired using EMMENU 3 from Tvips GmbH. EMMENU 3 acquires images to memory and writes them to the hard drive after acquisition has ended.

Each online in situ experiment involved a freshly prepared sample that was treated in flowing gas. Movies were acquired in either pure hydrogen or a mixture of hydrogen and water vapor.

5.5.1 Diffusion

To analyze the diffusion of metallic nickel particles, movies are acquired under 2-3mbar H_2O and 2mbar H_2 at 958K and 1023K. From the movies, every tenth frame was extracted and analyzed. Observations from the movies showed that particle migration occurred in a discrete manner and analyzing every tenth frame captured almost all of the migration of the particles.

Fig. 5.19 shows a sketch of the analysis method. Models of two consecutive images in the analysis set are shown. The support structure and particle is labeled 1 in the first image and 2 in the second image. The dashed arrows

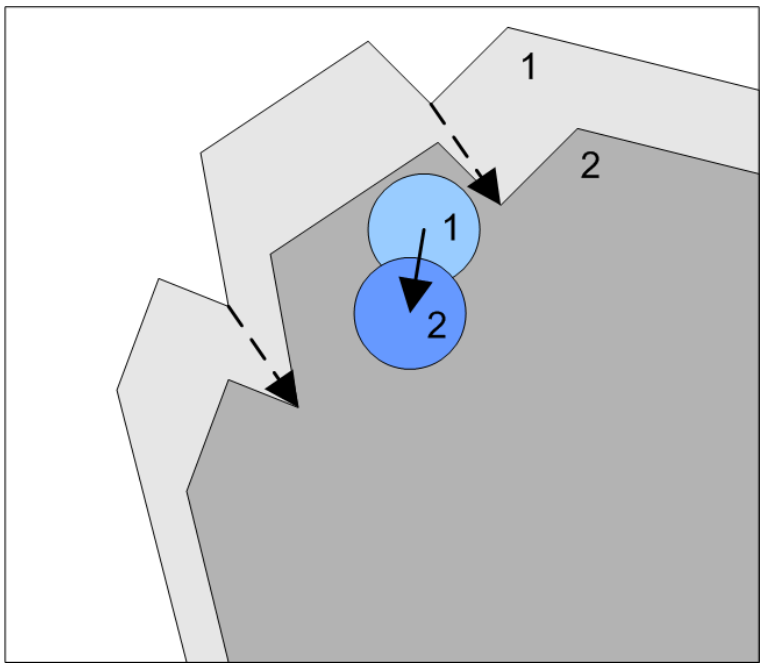

Figure 5.19: Sketch of the analysis procedure for the online experiments. See text for details.

show the movement of the support, the solid arrow show the movement in the particle. The effective migration of the metal particle between consecutive images is the difference between the relative movement of the support plate and the relative movement of the metal particle. The accumulated migration distance is the sum of the differences. This analysis method gives the 2-D projected migration of the particles. The low-surface area support material and the fact that movies were acquired from flat plate-like structures makes this a reasonable assumption.

The frames shown in Fig. 5.20 are extracted from a movie acquired at 1023K in 3mbar H_2 and 2mbar H_2O. The same region of the sample is shown over a period of 87s. Between Fig. 5.20(a) and Fig. 5.20(b), particle A (d=8nm) absorbs particle B (d=5nm), the resulting particle remains stable at the initial center of mass of particle A. From Fig. 5.20(b) to Fig. 5.20(e), C (d=11nm) moves downward following an edge on the support, the edge is visible through the particles. During particle C's migration it absorbs particles D (d=4nm) and E (d=5nm), particles much smaller than C, also attached to the edge. Particles D and E do not migrate themselves, but coalesce with C during C's migration. From Fig. 5.20(d) to Fig. 5.20(g), F (d=10nm) moves left along an edge and finally in Fig. 5.20(h) absorbs G (d=3nm), which has otherwise remained stable all through the duration of

the movie.

From frames like those shown in Fig. 5.20 (the frames do not necessarily coincide with the analyzed frames) the position and diameter of each particle was logged. The position of two reference points was also logged to correct for the sample drift. The reference points were most often intersections between support plates or recognizable corners. From the difference in position of each particle from frame to frame, the accumulated migration distance was calculated as a function of time, see Fig. 5.21. The diameter of the individual particles was monitored as a function of time and plotted as in Fig. 5.22. Data is shown over ca. 145s. The frames shown in Fig. 5.20 have been cropped to show the same area, so the number of particles are not the same as in Figs. 5.21 and 5.22. For the combined movie analysis, the first 100s of all movies were used, i.e. 11 frames from each movie was used for the analysis. From Fig. 5.21, it is observed that the particles that migrate the shortest distances all migrate ca. 0.3nm per sampling. Observations from the movies indicate that these particles are actually immobile, hence the total migration distance of ca. 3nm over the first 100s of the movie is attributed to the accuracy with which particle positions could be determined. Since 11 frames were analyzed from each movie the accuracy with which the position of a given particle can be determined is ca. 0.3nm every time a particle is sampled and the accuracy on the total migration data is ca. 3nm. Data was acquired from several in situ movies at 958K and 1023K, and the total migration distances over 100s are shown in Figs. 5.23 and 5.24. Each data point represents the accumulated migration distance of a single nickel particle. Particles ending their life in a coalescence event are not included in the plots since the coalescence results in an artificially long migration distance over a very short time interval. See Section 5.5.2 for a description of the actual coalescence events.

The horizontal traces of the particle diameters vs. time shown in Fig. 5.22 indicate that the diameters of the particles remain constant within the measurement accuracy over the acquisition of the movie. However, this does not necessarily mean that Ostwald ripening does not take place. The time scale over which the in situ TEM movies are acquired, is too short to make such a statement. The change in particle diameter resulting from Ostwald ripening can not be observed on this time scale. Vertical lines in the plots indicate sintering by coalescence.

In the in situ TEM movies, migration of large particles was more commonly observed than migration of small particles, see Figs. 5.23 and 5.24. Often large particles were observed to migrate from a position on the terrace to an edge site. In some cases smaller particles attached to an edge site were absorbed by larger particles on the terrace and the resulting particle would stick to the edge site at the initial center of mass of the smaller particle. Hence the center of mass for the small particle does not move whereas the larger particle migrates to the edge.

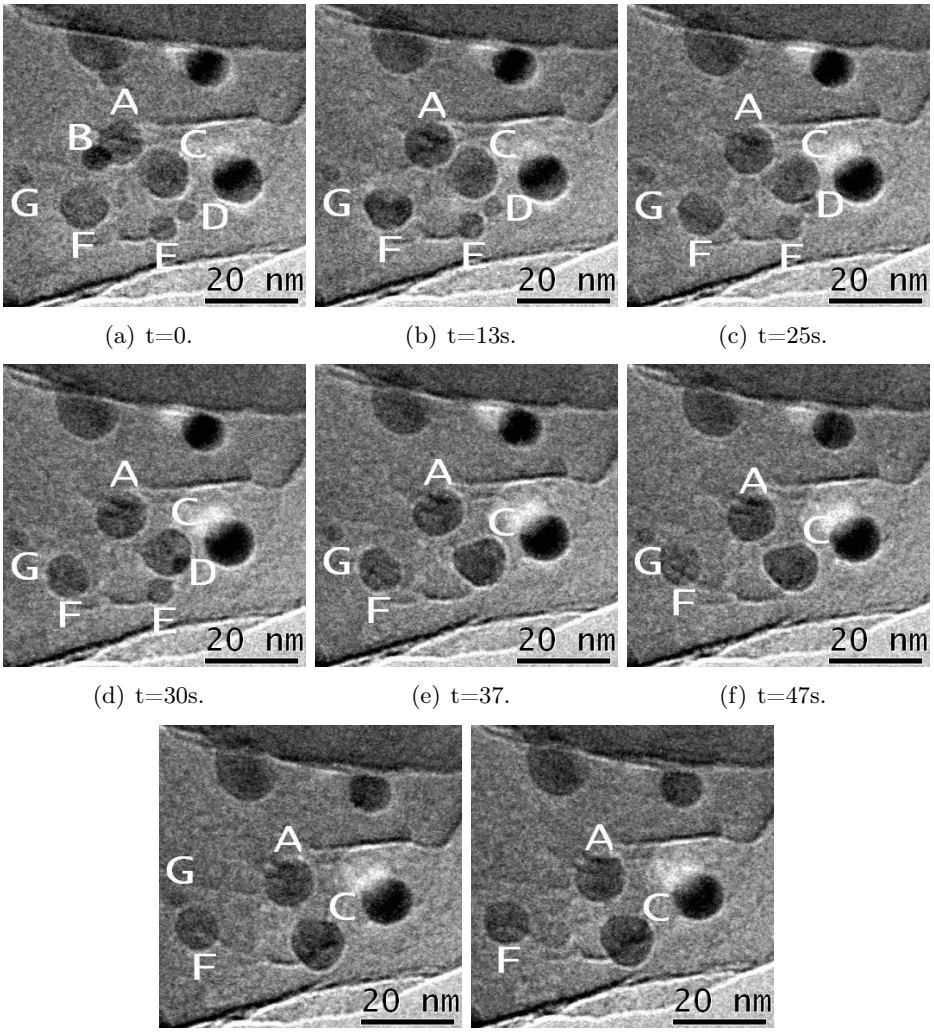

(a) t=0. (b) t=13s. (c) t=25s.

(d) t=30s. (e) t=37. (f) t=47s.

(g) t=80s. (h) t=87s.

Figure 5.20: Frames extracted from an in situ TEM movie acquired under 2mbar H_2O and 2mbar H_2 at 1023K. The larger particles migrate and absorb smaller particles they encounter on their way. The frames have been cropped to show the same area.

In some cases, nickel particles were observed to obtain shapes not resembling Wulff shapes. Fig. 5.25 shows frames of such a situation. Particle B is anchored at both ends, as it glides downwards in the frame at one end, the particle becomes elongated. The Particle was anchored at multiple anchoring sites and did not let go until the surface free energy of the particle became too large for the particle to stay attached at both anchoring sites. At t=103s, the energy lost to surface energy due to the elongation becomes

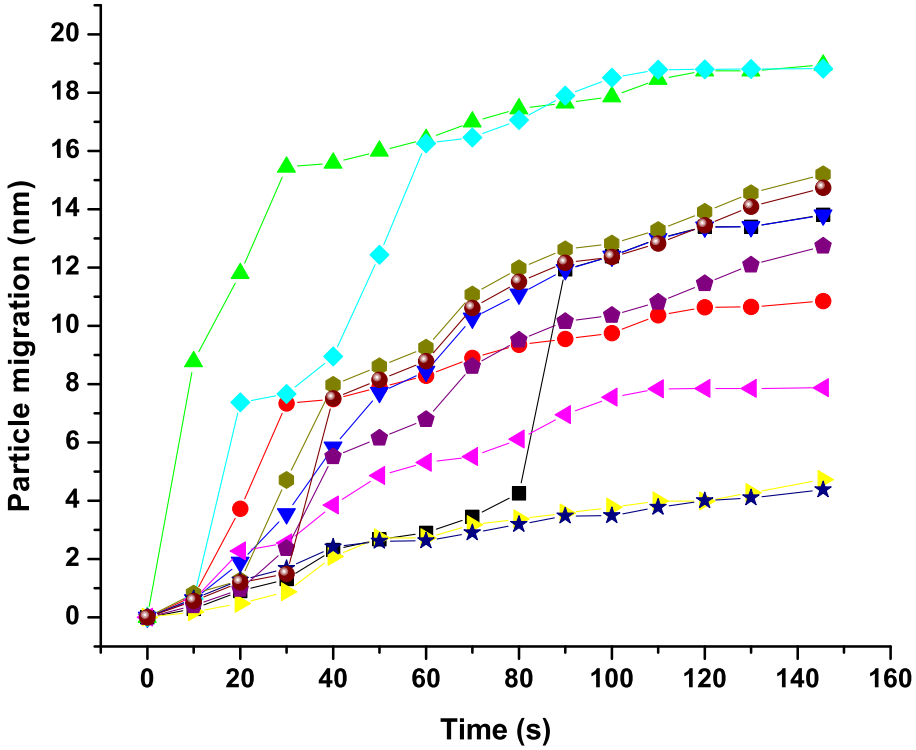

Figure 5.21: Accumulated migration as function time for the movie shown in Fig. 5.20. Each trace represents one particle.

larger than the energy gained from the anchoring site and the particle lets go at one anchoring point and contracts.

In other cases the largest particles were found to migrate along edges on the support. Fig. 5.26 shows a particle A migrating in a discrete fashion. Between the migrations, the particle remains stable at certain points along an edge seen through the particle. Such observations indicate that particles are bound more strongly to higher coordinated edge sites than to terrace sites.

The movies provide evidence for migration and coalescence of the Ni particles, no matter what the composition of the atmosphere was. However, a higher degree of migration was observed at higher temperature and when including water vapor in the atmosphere. The in situ TEM movies showed that the Ni particles migrate over very short distances. Surprisingly, the smallest metal particles with diameter <8nm, were found to migrate the shortest distances contrary to the d^{-4} scaling used by Gruber and Richardson/Crump, see e.g. Figs. 5.20, 5.27, 5.28, and 5.31. The longest migration distances

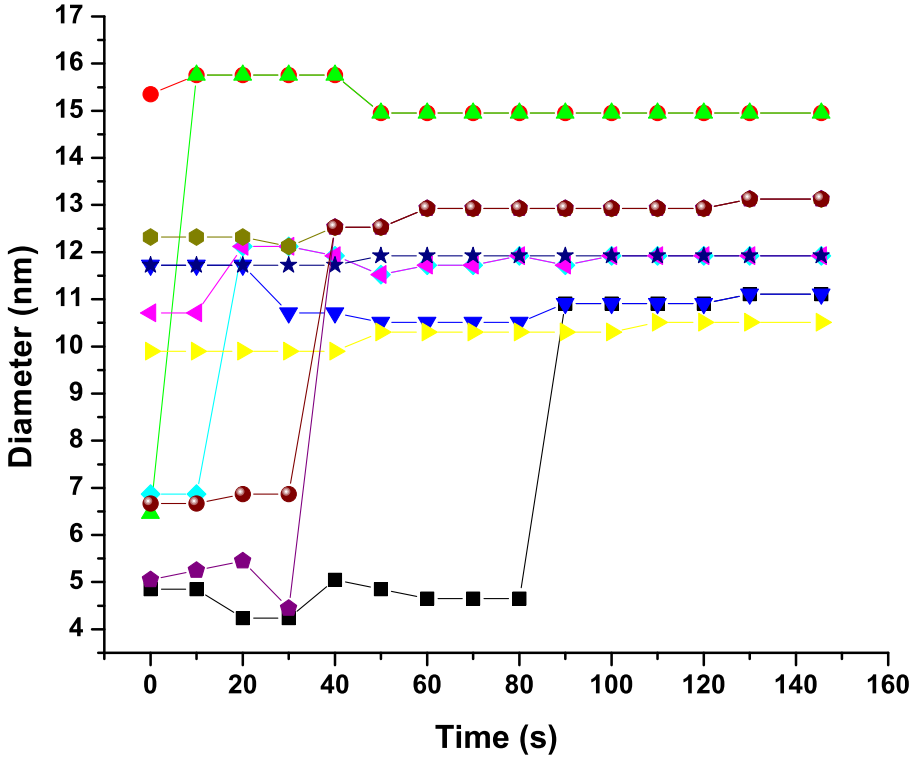

Figure 5.22: Particle diameter as function of time for the particles shown in Fig. 5.20. Each trace represents one particle. As most of the traces are horizontal, no indication of Ostwald ripening was observed.

were observed for the intermediate sized particles in the distribution, see Fig. 5.24. Random walk motion on a length scale as indicated in Table 5.4 was clearly not observed under any conditions. Migrating particles rapidly traveled short distances in a discrete jumping fashion, after which they resided in a location before they again rapidly jumped to a new location. This is seen in the migration plot in Fig. 5.21 where the traces are almost horizontal over long intervals if corrected for the 0.3nm accuracy per sampling. As indicated, the migration of a particle most often occurred along an edge on the support, or from a flat area to an edge.

To sum up this section, the main observations were:

1. Metal particles below ca. 8nm in diameter most often remain immobile, see Figs. 5.23 and 5.24.

2. Metal particles ca. 8-15nm in diameter are able to migrate on the support, see Figs. 5.23 and 5.24.

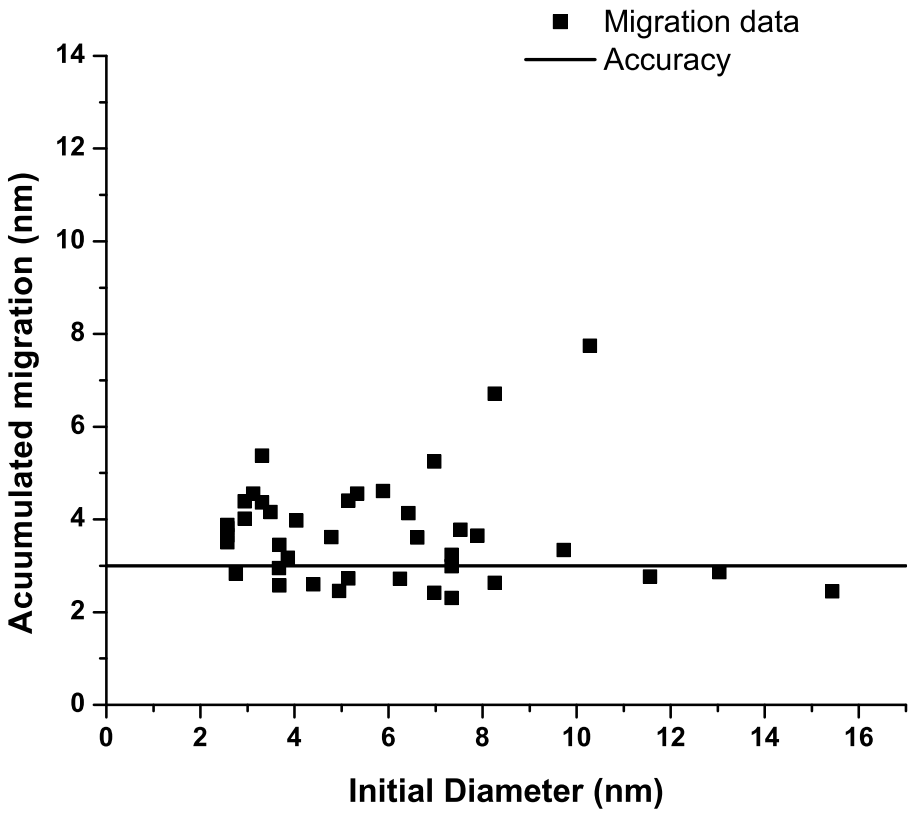

Figure 5.23: Migration distance as function of particle diameter over a 100s period as estimated from movies acquired at 958K in 2mbar H_2 and 2mbar H_2O. Each data point represents the migration of an individual particle.

3. Particle migration occurs primarily along edges on the support.

4. Particles with diameters larger than about 15 nm are immobile on the time scale used in the present study.

5.5.2 Coalescence

The coalescence events observed in the in situ TEM movies, mainly involved the larger particles in the ensemble. A d^{-4} scaling law predicts that if a large particle is to coalesce, a smaller particle should migrate towards the larger particle and coalescence can occur. The observations from the in situ TEM moves showed that if a small particle was to coalesce, a larger particle had to migrate to its location and coalescence could take place. The actual coalescence events observed occurred over a very short time interval, with the

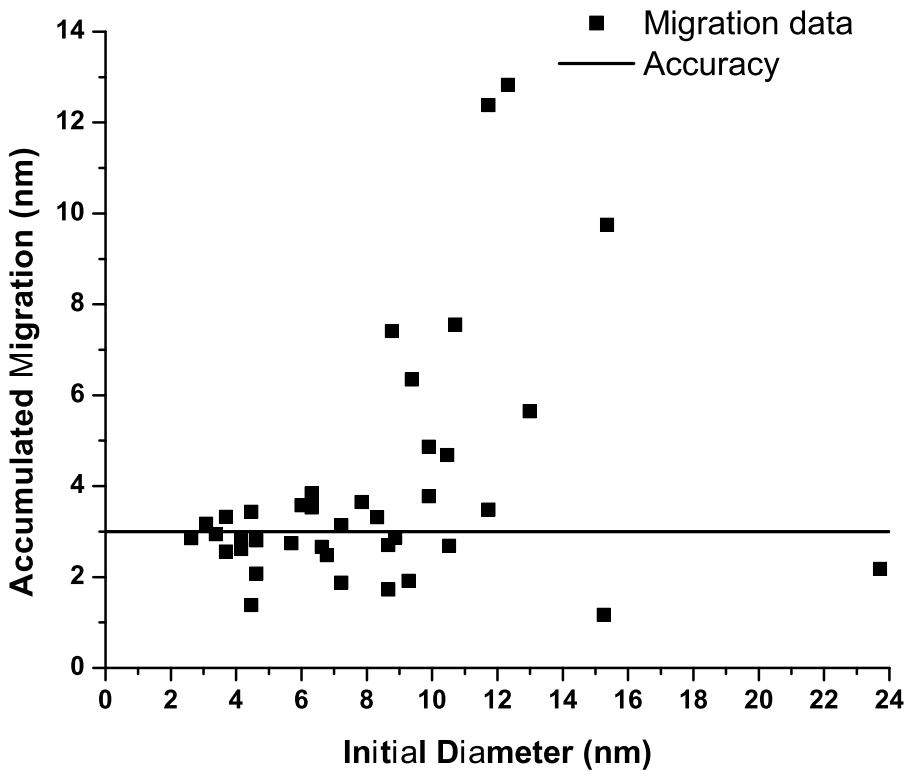

Figure 5.24: Migration distance as function of particle diameter over a 100s period as estimated from movies as shown in Fig 5.20 acquired at 1023K in 2mbar H_2 and 2mbar H_2O. Each data point represents the migration of an individual particle.

time resolution used (500ms) between two consecutive images, an intermediate state in the coalescence events was almost never observed. A van der Waals force may be responsible for this rapid coalescence. Immediately after the coalescence, the resulting particle achieved its minimum surface equilibrium shape and was again immobile on the support. Fig. 5.27 shows frames from an in situ movie acquired at 1073K in an atmosphere of 2mbar H_2 and 3mbar H_2O at 500ms exposure time. Two distinct coalescence events are observed. In the first event a particle A (d=7nm) coalesces with B (d=11nm). That A did not coalesce with C could be a result of height differences in the sample, e.g. C may sit on a terrace higher than the other two particles. This is not directly interpretable from the TEM images. Later on the resulting particle of the first event coalesces with C. In this event a cloud is observed in the region between the two particles, see Fig. 5.27(c). This could indicate

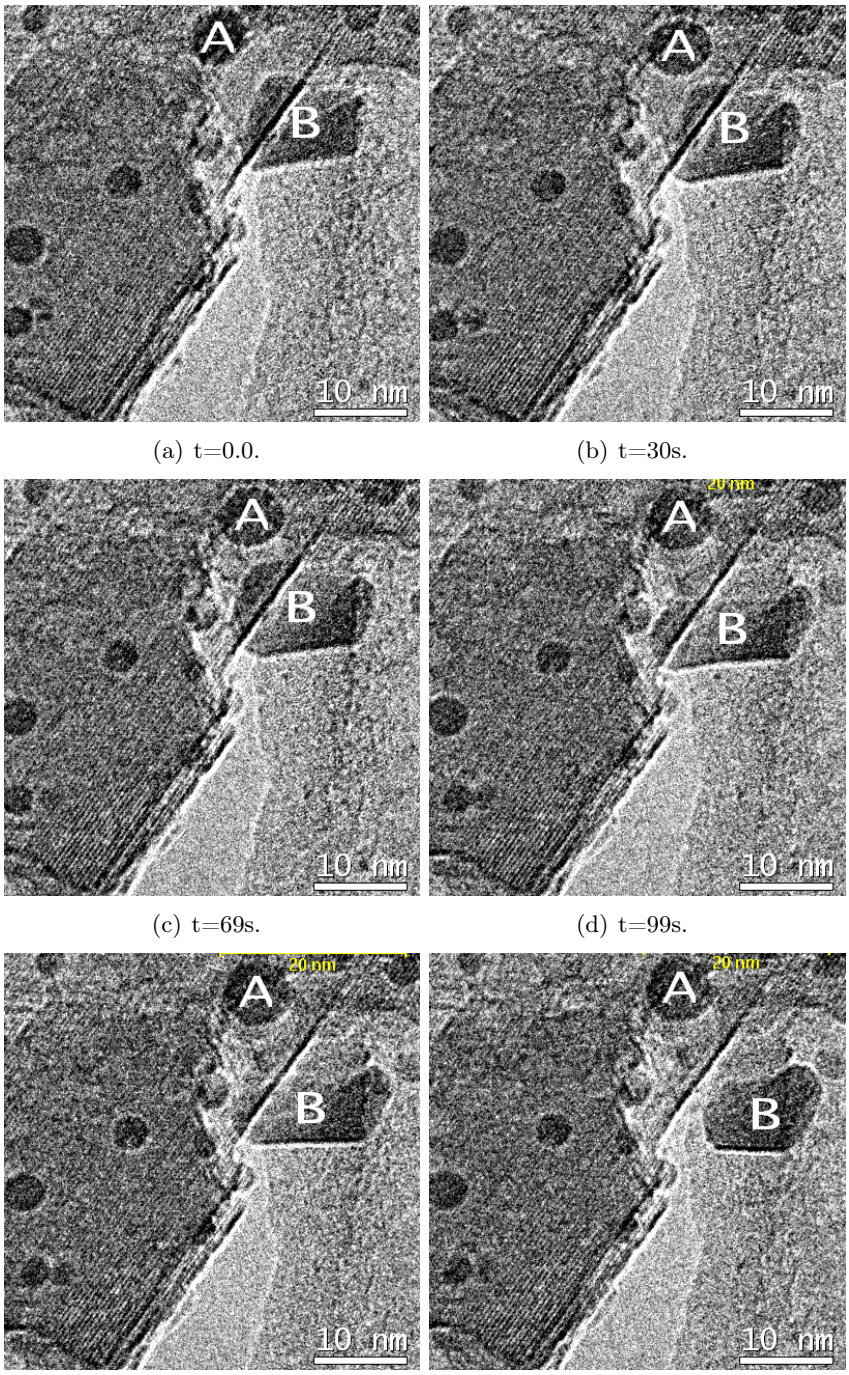

(a) t=0.0. (b) t=30s.

(c) t=69s. (d) t=99s.

(e) t=103s. (f) t=104s.

Figure 5.25: Frames extracted from an in situ TEM movie acquired under 3mbar H_2 at 871K. The particle labeled A moves from a terrace site to a step site and sticks to it. the particle labeled B sticks to edges and moves while attached at both ends. When the elongation becomes too energetically unfavorable, the particle releases at one end and becomes a stable particle. The other particles in the movie move very little.

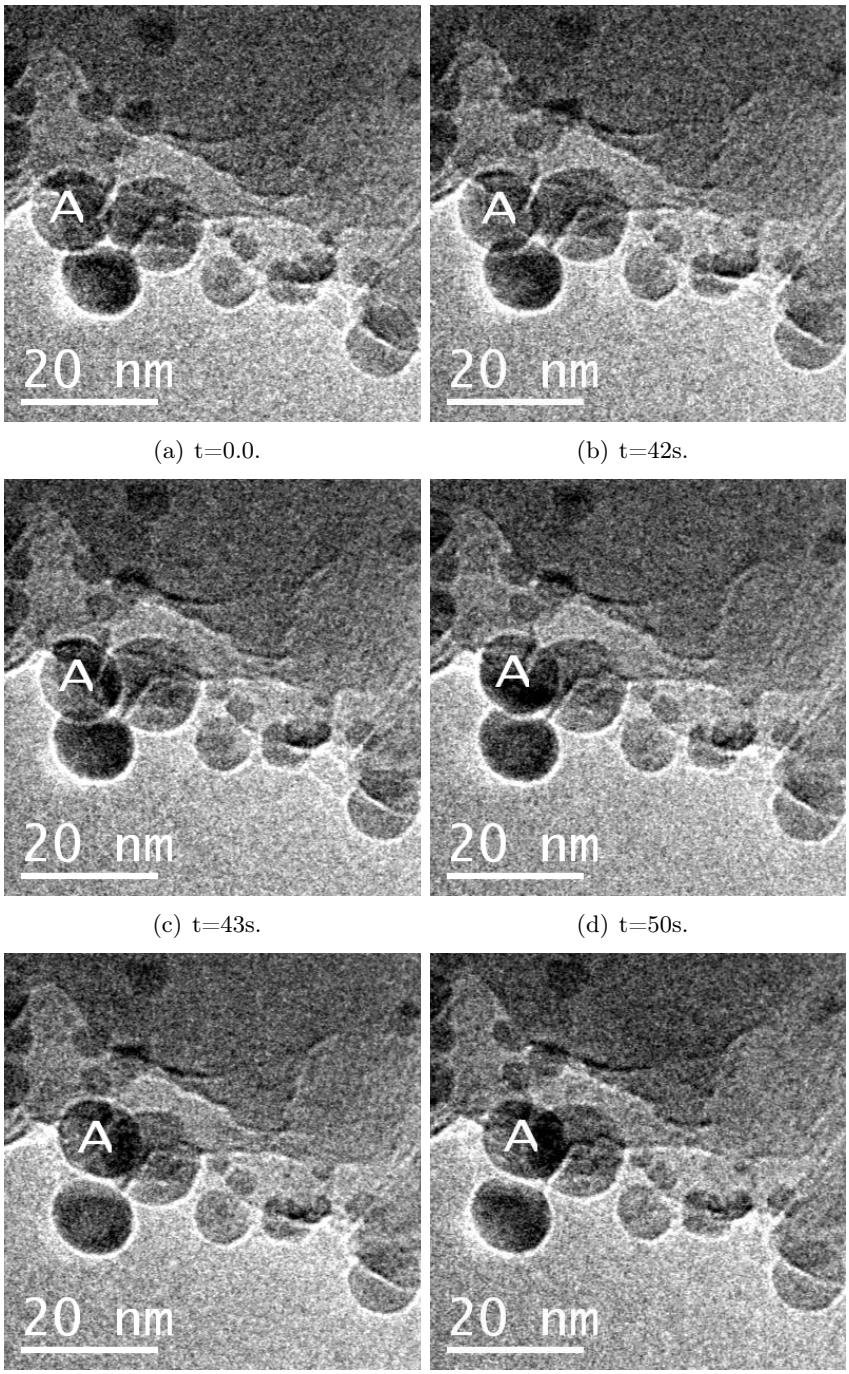

(a) t=0.0. (b) t=42s.

(c) t=43s. (d) t=50s.

(e) t=55s. (f) t=105s.

Figure 5.26: Frames extracted from an in situ TEM movie acquired under 2mbar H_2O and 2mbar H_2 at 1023K. The particle labeled A moves along an edge and remains stable in turn at different points. All other particles remain immobile. The individual migrations of particle A occur within one frame.

an initiation step of the coalescence event consisting of a bridge of atoms or molecules transporting mass between the two particles. Mobile surface atoms or clouds have been observed earlier for gold and ruthenium [91, 92]. The complete coalescence event occurred on a time scale shorter than 500ms and no frame showed other intermediate steps than the cloud in Fig. 5.27(c). The movie from which the frames were extracted was acquired at an electron dose rate of $4{\cdot}10^3 e^-/nm^2 s$ ($6.4{\cdot}10^2 A/m^2$). A similar event occurs in Fig 5.28. This event occurs on a terrace where two particles similar in size coalesce with the resulting particle resting in the center of mass of the two initial particles. Again the coalescence event takes place in less than 500ms. For the frames shown in Figs. 5.27 and 5.28 particles smaller than ca. 8nm in diameter are observed, but their migration is minimal.

Figs. 5.25, 5.26, and 5.29 show further examples of particle migration and/or coalescence. These movies are representative for the conditions under which they were acquired. In all cases, a higher degree of mobility is observed for the larger particles in the frames. Particles smaller than ca. 8nm in diameter migrate only short distances and such migration was rarely observed.

From the in situ movies it is possible to estimate a metal diffusivity and an activation energy during the coalescence event. The images in Fig. 5.27 are used for the calculation. For simplicity it is assumed that all atoms of particle B are located at the center of mass of the particle in Fig. 5.27(c) and moves to the center of mass of the resulting particle in a linear fashion. Numbers and formulas for non-faceted spheres from [43] and [93] are used. The crystal diffusivity, D_c, is determined from

$$X_c = 2\sqrt{D_c t} \Rightarrow D_c = \left(\frac{X_c}{2}\right)^2 \frac{1}{t} \tag{5.13}$$

where X_c is the crystallite migration distance and t the time. Hence the crystal diffusivity is

$$D_c = \left(\frac{13.4nm}{2}\right)^2 \frac{1}{0.5s} = 89.78nm^2/s. \tag{5.14}$$

From the crystal diffusivity the metal surface diffusivity, D_s, is determined from

$$D_c = 0.301 D_s \left(\frac{a}{r}\right)^4 \Rightarrow D_s = \frac{D_c}{0.301}\left(\frac{r}{a}\right)^4 \tag{5.15}$$

where a is the atomic diameter and r the particle radius. Using a=0.23nm, r=5.5nm, the metal surface diffusivity is

$$D_s = \frac{89.78nm^2/s}{0.301}\left(\frac{5.5nm}{0.23nm}\right)^4 = 9.75 \cdot 10^7 nm^2/s = 9.75 \cdot 10^{-7} cm^2/s. \tag{5.16}$$

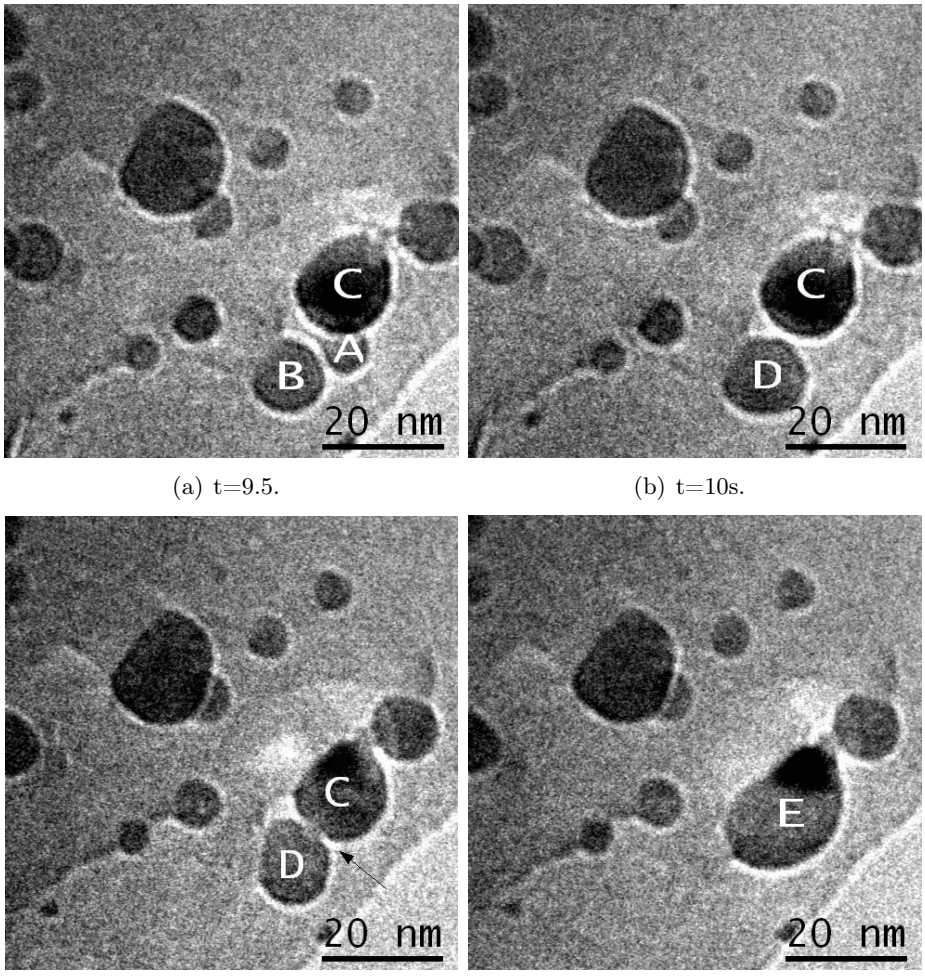

(a) t=9.5. (b) t=10s.

(c) t=56s. (d) t=57s.

Figure 5.27: Frames extracted from an in situ TEM movie acquired under 3mbar H_2O and 2mbar H_2 at 1073K. Image series showing coalescence over a time interval of less than 500ms. A narrow cloud between the two particles just before coalescence is indicated.

In terms of activation energy this gives

$$D_s = D_0 \exp(-E_a/RT) \Rightarrow E_a = -\ln\left(\frac{D_s}{300}\right) RT = 174 kJ/mole. \quad (5.17)$$

Sehested *et al.* [11] report activation energies of 115kJ/mole in the temperature interval 773-923K and 292kJ/mole in the interval 923-1098K. The value of E_a determined in Eqns. 5.14 - 5.17 is a very crude way of estimating the activation energy of surface diffusion of nickel species. The mechanism

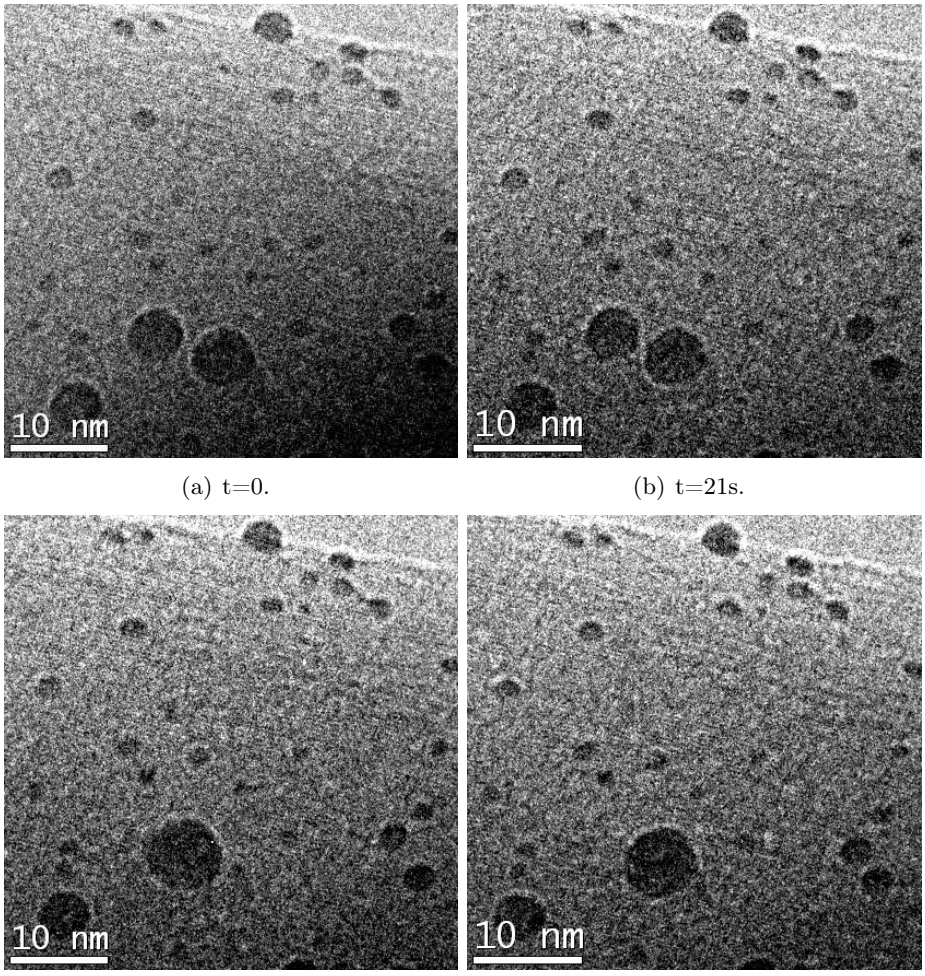

(a) t=0. (b) t=21s.

(c) t=22s. (d) t=55s.

Figure 5.28: Frames extracted from an in situ TEM movie acquired at 881K in 3.5mbar H_2. The small particles remain immobile on the surface of the support while the two largest coalesce and form one particle.

for metal particle diffusion may not be the same during coalescence as it is during migration. The accuracy of the calculation is mainly limited by the sampling rate (1/exposure time) of the movies. Hence the number should be regarded as an upper limit for the metal diffusivity.

5.6 On Electron Beam Effects

To estimate the influence of the electron beam dose rate on particle mobility, movies were acquired using electron dose rates up to ca. 70 times higher than

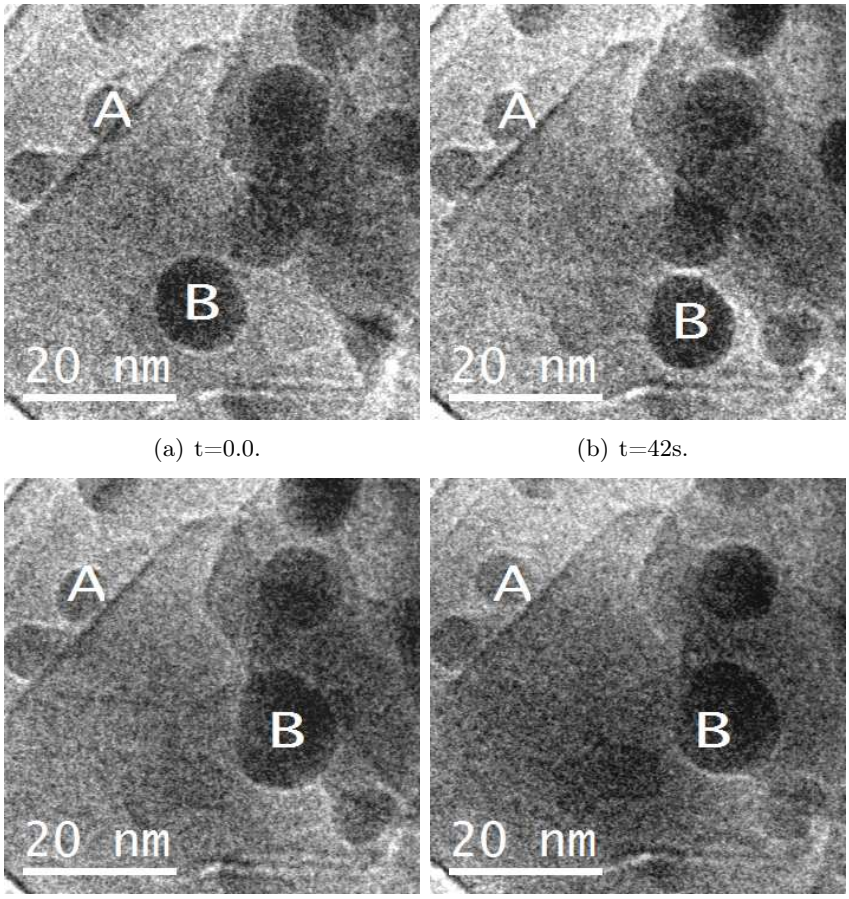

(a) t=0.0. (b) t=42s.

(c) t=43s. (d) t=50s.

Figure 5.29: Frames extracted from an in situ TEM movie acquired under 8mbar H_2O and 2mbar H_2 at 1023K. The particle labeled A moves sticks to a step and moves along it. The big particle labeled B moves on a terrace and coalesces with a particle attached to a step.

those used for the analyzed movies as shown in e.g. Fig. 5.20. At the higher dose rates the only observable difference is damage to the support material. The particle migration observed under the high beam intensity was similar to that observed in the analyzed in situ TEM movies. Fig. 5.30 shows a region of the $Ni/MgAl_2O_4$ catalyst before and after exposure to an intense electron beam. From the figure it is observed that two nickel particles have remained immobile and one nickel particle (ca. 10nm in diameter) has migrated ca. 10nm. This migration distance is similar to that observed for 10nm particles in Fig. 5.24. Damage like in Fig. 5.30 was observed in the analyzed movies, but only after prolonged exposure to the electron beam, longer than twice

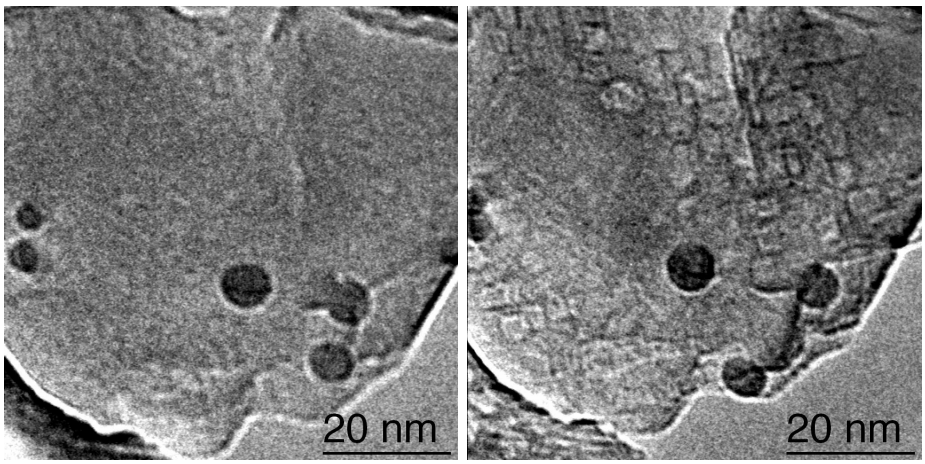

(a) Area of sample prior to exposure to intense beam.

(b) Same area after exposure to intense beam.

Figure 5.30: Images of the same area before and after exposure to an intense electron beam. Fig. 5.30(a) is acquired at an intensity similar to the intensity used to acquire the in situ TEM movies. Fig. 5.30(b) shows the same area of the $Ni/MgAl_2O_4$ sample after ca. 2 minutes of exposure to an electron dose rate of $1.4{\cdot}10^5 e^-/nm^2{\cdot}s$ ($\sim 2 \cdot 10^4 A/m^2$). The movie from which the images were extracted was acquired under 2mbar H_2O and 2mbar H_2 at 1023K.

the analysis period.

5.6.1 Migration Studies of Ruthenium on Boron Nitride

In situ movies have shown highly mobile ruthenium particles on boron nitride support under an intense electron beam. However the electron beam did not damage the boron nitride support to the same extent as the $MgAl_2O_4$ was damaged.

To further shed light on the effects of the electron beam on the mobility of metal particles particles, the ruthenium/boron nitride catalyst was studied at different temperatures under the same electron beam dose rate. Hence if the mobility is affected by the electron beam, the effect will be the similar in all cases. The electron dose rate used for acquiring the in situ TEM movies of the ruthenium/boron nitride catalyst was comparable to the intensity used for the Ni/spinel catalyst. The experiment was done at a higher temperature than the $Ni/MgAl_2O_4$ experiments. The Ru/BN catalyst was chosen since BN is more stable at high temperatures than $MgAl_2O_4$.

For this experiment, the Ru/BN catalyst was crushed using a mortar and pestle, and dispersed on a molybdenum TEM grid. Molybdenum was chosen over stainless steel since it is more inert in non-oxidizing atmospheres. A 3:1

mixture of H_2 and N_2 was introduced into the in situ chamber at a total pressure of ca 3.4mbar. Movies were acquired at room temperature after which the temperature was increased in steps to 580K, 681K, 793K 881K, and 963K at this temperature the heating stage was at maximum power. The temperature was then increased further by decreasing the gas pressure in the in situ cell. At P=0.7mbar the temperature was 1174K, at P=0.5mbar T=1203K, and at P=0.3mbar T=1244K. At each temperature a movie was acquired and the particle mobility analyzed. Fig 5.31 shows a series of images from the movie acquired at 1244K. Up to 963K no mobility of the ruthenium particles was observed. At the higher temperatures an increasing amount of particle mobility was observed. In movies showing particle mobility, those acquired at T>1174K, were analyzed for mobile particles. The result of the analysis is shown in Fig. 5.32. Each point in Fig. 5.32 represents a ruthenium particle. The particle is plotted in the lower group if it remains stable over the duration of the movie, ca. 2min, and in the upper group if it migrates over the support. The migration length is not considered in the plot, however, the particles migrating the longest distance at each temperature has been indicated by a circle. These "supermovers" are found in the diameter region from 9-16nm, i.e. in the middle of the total particle ensemble. In the movie acquired at 1244K, see Fig. 5.31, the "supermover" first moves from a terrace to an edge, then moves along the edge, leaves the edge and migrates across a terrace, sticks to another edge, and then leaves this edge. This behavior is similar to the behavior observed for the nickel particles on spinel support. The analysis also shows that large particles up to ca. 22nm are found on the support.

Gryaznov *et al.* [94] calculated the effects of the electron beam in an electron microscope on the local temperature of gold nano-particles. They found that the increase in local nanoparticle temperature goes as $T \propto d^2/k$, where k is the thermal conductivity of the metal particles in the sample. At beam intensities around $3{\cdot}10^2 \mathrm{A/m^2}$, roughly the values used for recording the in situ TEM movies reported here, the local temperature increase induced by the electron beam for a gold particle with d=20nm was ca. 50K. This diameter corresponds to the upper end of the nickel particles shown in Fig. 5.23 and 5.24. As the thermal conductivity of nickel is lower than that of gold and most nickel particles observed are smaller than d=14nm, an even lower temperature increase is expected for the nickel particles.

Since particles remain immobile up to a certain temperature under a given electron dose rate, it is concluded that the temperature increase induced by the electron beam is of minor importance compared to the heat supplied by the holder. This is seen from Fig. 5.32 where at T=963K all particles are plotted in the lower immobile group. At T = 1174K, particles start to move under the same electron dose rate shown by particle plotted in the upper mobile group. As the temperature is increased further, more an larger particles are plotted in the upper group. However, the effects of the

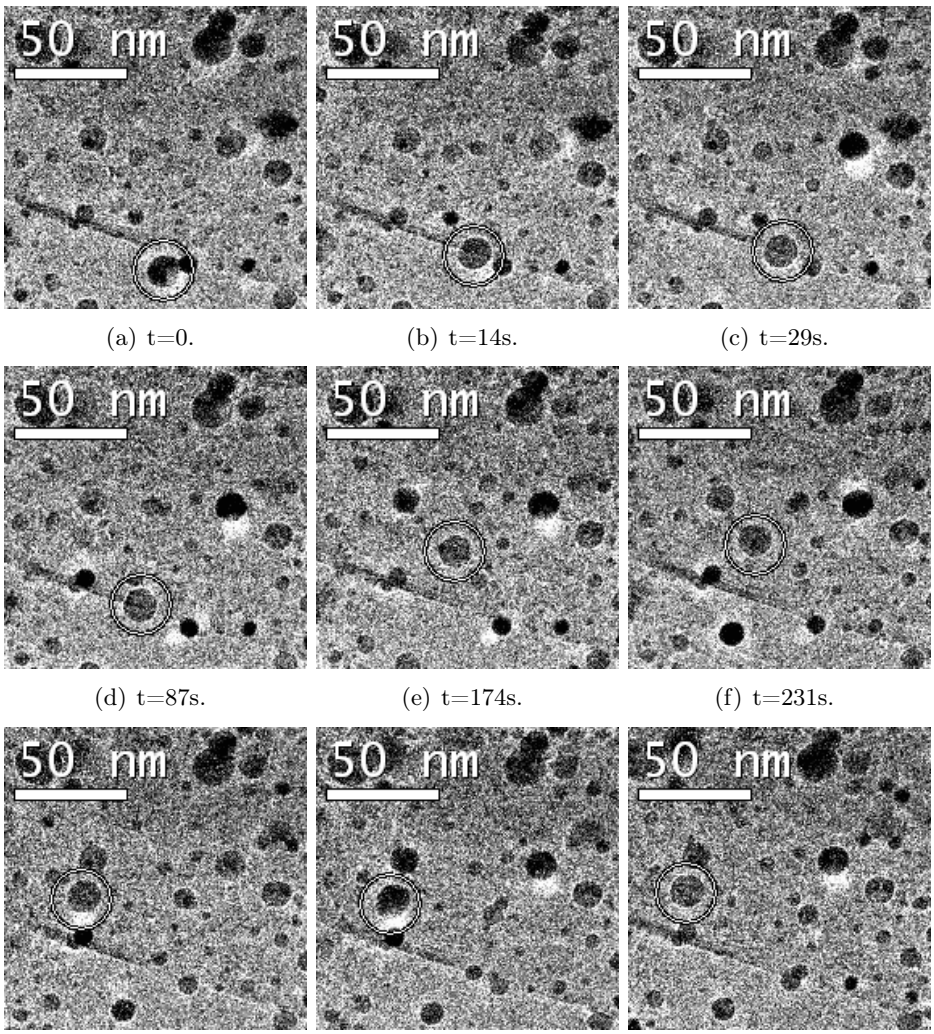

(a) t=0. (b) t=14s. (c) t=29s.

(d) t=87s. (e) t=174s. (f) t=231s.

(g) t=390s. (h) t=444s. (i) t=490s.

Figure 5.31: Frames from an in situ TEM movie of ruthenium on boron nitride acquired at 1244K in 0.3mbar 3:1 H_2/N_2. The "supermover" is shown with a circle corresponding to the red circle in Fig. 5.32.

electron beam cannot be neglected entirely. Most likely, the local temperature on the catalyst sample is the sum of the contribution from the holder and the contribution of the electron beam, the latter being the smaller contribution. The temperature increase induced by the electron beam has been minimized by keeping the electron dose rate as low as possible. It is also a possibility that the effect of the beam is to induce anchoring sites in the support material giving rise to more stable metal particles.

The conclusion here is that under the conditions used, exposing the sam-

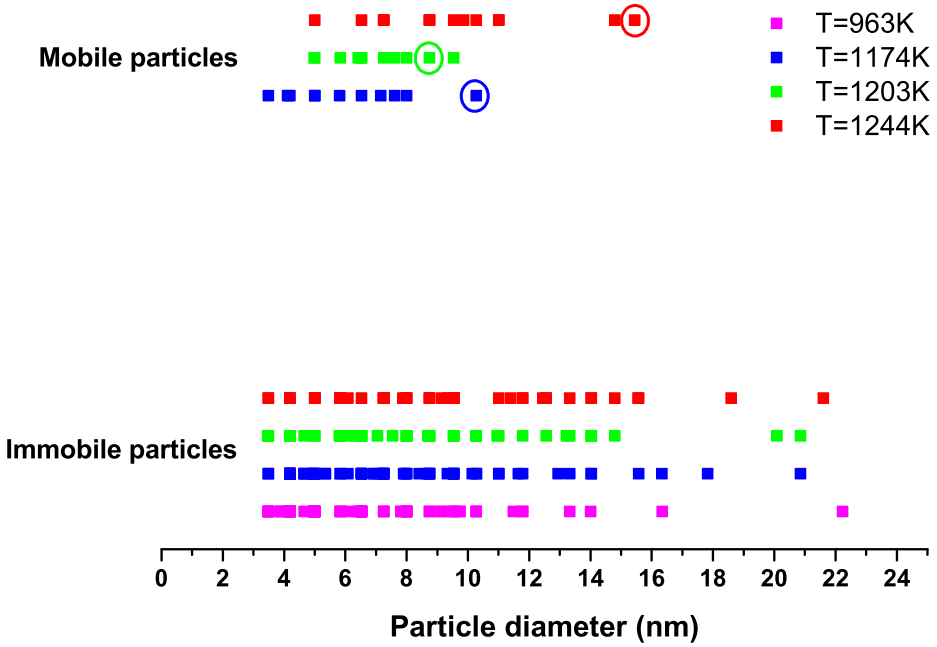

Figure 5.32: Mobility of Ru particles on BN. The lower group of particles remain immobile over the duration of the movies. The upper group represent mobile particles. The particles migrating the longest distance are indicated by circles.

ples to electron dose rates below ca. $10^3 \mathrm{A/m^2}$ does not induce significant migration of the metal particles as compared to the mobility induced by the heating of the sample. Future experiments are needed if the effect of the beam on the local temperature is to be quantified. For the particle sizes dealt with in this work, this is also the conclusion of the theoretical work by Gryaznov *et al.* [94].

The mobility of the ruthenium particles was studied to estimate the activation energy of the migration process. The migration distances of the two most mobile ruthenium particles in the movies acquired at 1174K, 1204K, and 1244K were determined in the same way as the migration distances of the nickel particles were determined. The mean diffusion coefficients, D_s, were determined using Eqns. 4.8, 4.9, and 4.10. The logarithm of the diffusion coefficients was plotted against $1/RT$ in Fig. 5.33 and the activation energy was determined from the slope of the plot. The activation energy as determined from this analysis is $277 \pm 10\mathrm{kJ/mole}$.

When evaluating this activation energy it is worth noting, as seen from Fig. 5.31, that many particles of various sizes remain immobile and only few particles migrate, suggesting that two individual processes are involved in the

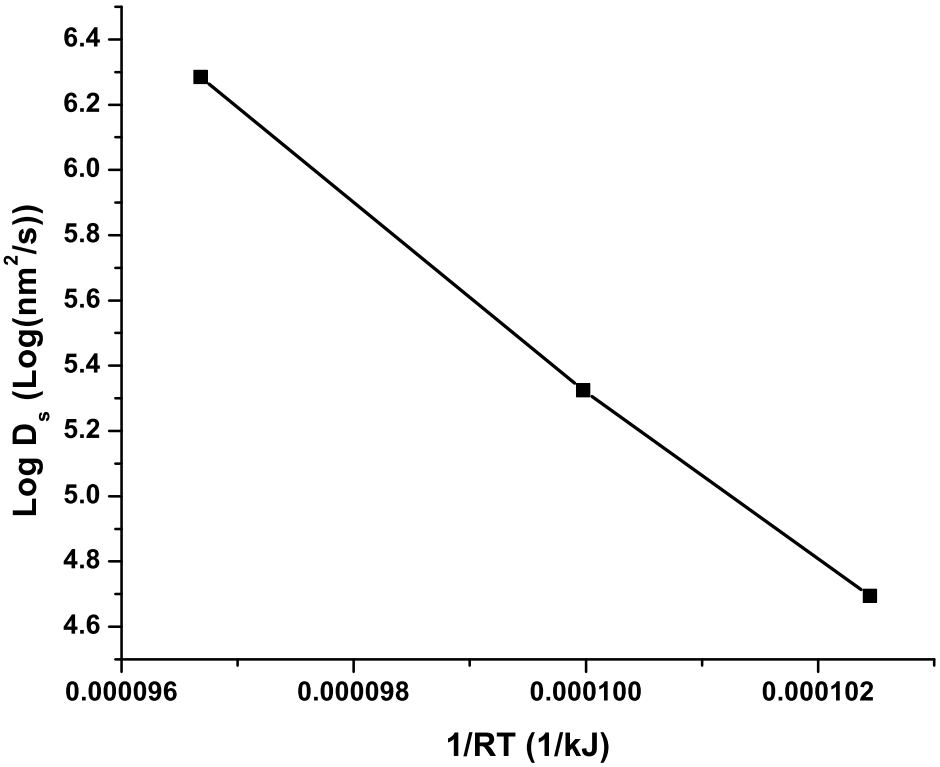

Figure 5.33: Arrhenius plot for determining the activation energy of the mobility of ruthenium particles on boron nitride. The data was extracted from the in situ TEM movies described in the text.

sintering: the release of the particles form the support, and the migration of the particles on the support. More on this later.

5.7 Discussion

5.7.1 Comparison of Parameter Experiments With Theory

The plots of the mean diameter vs. time, Figs. 5.8 and 5.9, were fitted using the model of Sehested

$$\bar{d}_{Ni}(t) = \left(const \cdot \frac{K_2 D_{OH-dimer} X_{Ni} t}{\bar{d}_0^7 (1 - X_{Ni}) A_{car}} \cdot \left(\frac{P_{H_2O}}{P_{H_2}^{0.5}} \right) + \bar{d}_{Ni,0}^7 \right)^{1/7}. \qquad (5.18)$$

Here K_2 is the equilibrium constant for the formation of a 2Ni-OH complex, $D_{OH-dimer}$ is the diffusivity of 2Ni-OH complexes and *const* is a constant. For further details, see [11]. The formula has been derived based on classical

theory, density functional theory and on experiments done in microreactors at atmospheric pressure and above. Eqn. 5.18 predicts that sintering in a dry environment will result in no change of the mean particle diameter. However this is not an industrially realistic situation and the extrapolation of the equation to such a condition may not be justified. In the present study, sintering experiments carried out in non-aqueous environments were not compared with Eqn. 5.18. Sintering might however still proceed via other mechanism than nickel-dimer diffusion, e.g. monomer diffusion as also discussed in [11].

Within the width of the distributions, Eqn. 5.18 accurately fits the observations. The model thus accounts for sintering data at very different conditions, from the high pressure reactions experiments to the low pressure in situ TEM experiments. The mean diameters follow traces as also shown in Fig. 5.34, with most of the particle growth occurring in the initial period of sintering after which the rate of particle growth flattens out as many particles have grown too large to migrate significantly. The experiments also show, in agreement with the Eqn. 5.18, that the temperature has a large influence on the growth of metal particles. The temperature is accounted for in Eqn. 5.18 in the K_2 and $D_{OH-dimer}$ terms. The conclusion from the parameter experiments is that Eqn. 5.18 can explain the evolution in nickel particle growth at pressures in the millibar regime.

5.7.2 Comparison of Offline Experiments with Theory

In agreement with the parameter experiments, the offline experiments show only minor changes in both mean particle diameter and particle size distribution at 1023K in pure hydrogen, see Fig. 5.12. The only difference is minor increase in mean particle diameter from 3nm to 4nm and a slight broadening of the peak due to the formation of a few particles slightly larger than average responsible for the change in mean diameter. The shape of the PSD, both before and after sintering, can be accurately fitted with a log-normal distribution. After 5 hours the fraction of particles with diameter below 3nm has only changed from 61% to 49%. Richardson and Crump [43], showed that after reduction in hydrogen and sintering in helium at 873K their particle size distribution became bimodal. Even after 30 hours of sintering they still had a considerable amount of particles below 3nm. Thus it seems that a considerable amount of the initial particles remained immobile. The difference in sintering atmosphere between the present study (the non-aqueous experiments) and the data of Richardson and Crump should have minor influence since the nickel particles will stay reduced in the inert helium atmosphere at 873K. Other authors have reported only little sintering of nickel in pure hydrogen [39, 95, 96]. This agrees well with Eqn. 5.18 which predicts no sintering in pure hydrogen [11].

The addition of water vapor to sintering atmosphere has a significant

effect on metal particles. After 5 hours at 923K in 2mbar H_2O and 2mbar H_2, the PSD has broadened significantly and most of the particles below 2nm have disappeared, see Fig. 5.14. The tail on the large diameter side of the distribution has become longer and particles above 10nm in diameter are observed. The peak in the distribution does, however, only shift from 3nm to 4nm.

Increasing the partial pressure of water in the sintering atmosphere, 9mbar H_2O and 1mbar H_2 at 923K, increases the sintering even further. After 5 hours of sintering the FWHM of the distribution has doubled, see Fig. 5.16. The largest particles are around 18nm, but still a significant amount of particles, 14%, below 4nm are found in the distribution, therefore a lot of particles are still inactive in the sintering process. However, not many of the largest particles are found, the distribution is flat past 12nm and contains very few particles.

Making the sintering conditions even more severe with respect to temperature, see Fig. 5.18, 1023K, 2mbar H_2O, 2mbar H_2 further widens the particle size distribution. Particles larger than 20nm in diameter are now formed within 5 hours of sintering. Again the distribution is flat ranging from 16nm to 24nm. Small particles are still present in the distribution, however their fraction has decreased from 57% to 3%. The decrease in the number of small particles can be a result of sintering occurring when larger particles migrate and absorb the small particles when encountered.

On the small diameter end of the particle size distribution for all the offline experiments particles were found to persistently exist after 5 hours of sintering. Thus these particles seem to have a high activation energy for mobility. Agreeing with conventional knowledge, the increase of temperature and the partial pressure of water vapor in the sintering environment increased the sintering rate. However, at 773K the water vapor did not seem to significantly alter the particle size distribution over 5 hours.

From the offline data it is possible to estimate the validity of the Sehested equation when extrapolating to the low pressures in the in situ TEM. For the offline experiment carried out at 923K and 1023K, the mean particle diameters obtained were compared with Eqn. 5.18 [11]. Using the mean diameters obtained in the offline experiments after 5 hours of sintering in 2mbar H_2O and 2mbar H_2 at 923K and 1023K, $d = 4 \pm 2$nm and 10 ± 5nm respectively, and combining $const$, K_2 and $D_{OH-dimer}$ into one constant, C, the theoretical evolution in particle diameter was estimated. Values for the combined constant were derived using the solver function in MS Excel. The evolution in mean particle diameter based on Eqn. 5.18 using these constants has been plotted in Fig. 5.34. Using Eqn. 5.18 to estimate the mean particle diameter after 5 hours of sintering in 9mbar H_2O and 1mbar H_2 at 923K using the constant found for 2mbar H_2O and 2mbar H_2, gives d=5.6nm, which is slightly lower than the value found in the in situ TEM experiments, $d = 6 \pm 3$nm, but still well within the width of the distribution.

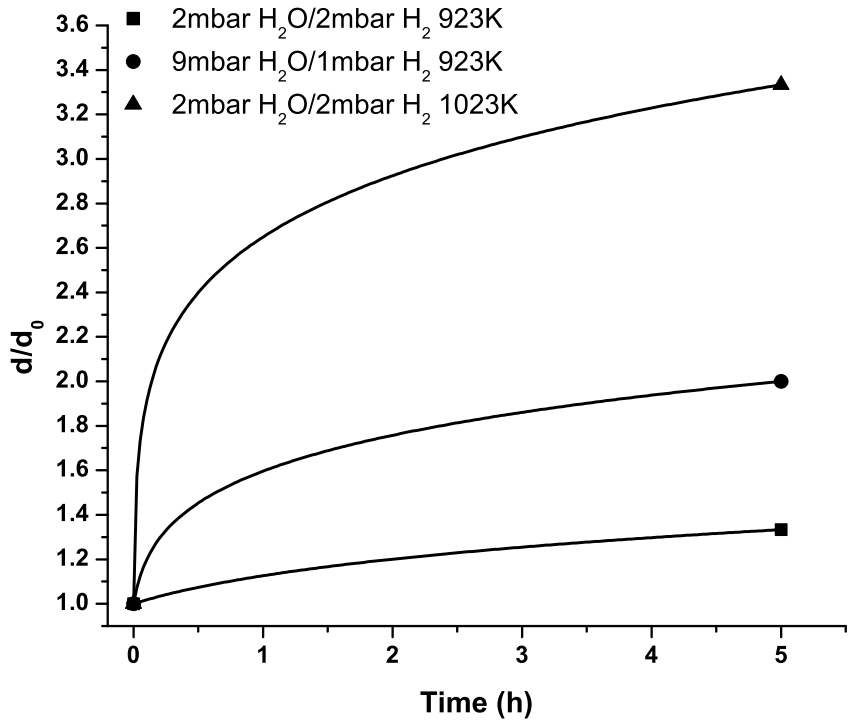

Figure 5.34: Evolution of mean particle diameter as predicted by the Sehested formula. The solid lines show the fits to Eqn. 5.1.

Such comparisons have not been possible for the other conditions due to the experimental challenges mentioned earlier. The correspondence between the in situ TEM data and the Sehested equation substantiates the validity of the equation and the assumptions behind it.

Fig. 5.34 shows that in 2mbar H_2O and 2mbar H_2 at 1023K, Eqn. 5.1 predicts rapid growth of the nickel particles. The Ni particles grow to half the diameter found experimentally after 5 hours in less than 15 minutes, meaning that most of the sintering events must occur in this period. Hence not many events are expected after this time. The number of observed migration and/or coalescence events observed in the online experiments was similar or lower than expected from the calculation in Section 5.4.1, and hence consistent with Fig. 5.34. Since the transient period is longer than three minutes this reduced number of observed events seems reasonable based on Eqn. 5.18.

The offline experiments showed that in different environments at different

temperatures, a population of particles below 5nm in diameter exists after 5 hours of exposure to the sintering environment. These particles must somehow be trapped to anchoring sites on the support material and not be able to participate in coalescence events unless other particles migrate to their position. Further an expectancy frequency with which to observe particle coalescence events was determined based on the initial and final metal particle average diameters.

In summary, it is found that Eqn. 5.18 can predict the mean particle diameter in the pressure regime relevant for the in situ TEM.

5.7.3 Discussion of Online Experiments

Whereas the classical Gruber picture of metal particles moving in a random walk with a diffusion constant that scales as d^{-4} may account for the migration of metal particles on a perfect defect free support, it is not consistent with the current in situ TEM observations. In a previous study by Baker *et al.* [97] it was observed that small particles moved faster than the larger particles and the diffusion distances did approximately follow a d^{-4} scaling. In contrast, the in situ TEM work presented here has involved experimental steam-reforming catalysts. The $Ni/MgAl_2O_4$ catalysts may provide bonding of Ni particles to defects on the support, causing the nickel particles to be less mobile. The rate limiting step appears to be the detachment of metal particles from their stable anchoring sites. Activation barriers for this process may be derived from future in situ TEM studies involving larger variations in temperature, larger data sets and movie acquisition directly after the temperature has reached the sintering temperature. However, sample drift makes it challenging to record movies while the sample temperature is being changed, i.e. in the transient period. This represents a significant experimental challenge.

If the sintering events are evenly distributed over the sintering period, approximately 1 event should be observed in each in situ TEM movie. These numbers are higher than the order of magnitude experimentally observed. Since acquisition of an in situ TEM movie with a quality for analysis requires a stable sample, the movies are often acquired some time after the desired temperature has been reached due to stability issues. At this time the majority of the sintering events may already have happened and the probability of observing an event will be lower than the number found in Section 5.4.1. The smaller particles that were not anchored from the beginning of the heating ramp can become mobile in the transient period and find an anchoring site or coalesce with other particles. This can explain why in the period after the transient period, where the analyzed movies are acquired, only coalescence events between larger particles are observed, and smaller particles that haven't already diffused or coalesced will remain stable, maybe because they have found an anchoring site of low potential energy. The estimate

in Section 5.4.1 is rather crude and does not take into account that in situ movies are preferentially acquired with a small amount of empty space in the field of view, and the morphology of the support is regarded as a perfectly flat plate.

An important observation is that small particles can remain immobile on the support and coalesce with larger particles only when the larger particles migrate to the smaller particles positions. Such observations substantiate a model where small particles are trapped by the support material.

Observation of coalescing particles occurred only rarely. Most movies were acquired at 1023K in 2mbar H_2 and 2mbar H_2O, the same conditions under which the data shown in Fig. 5.18 was acquired. In Fig 5.18 the population decreases from 505 particles to 235 particles, i.e. ca. 250 coalescence events occurred over 5 hours corresponding to ca. 1 event per minute. Qualitatively this number corresponds well with the number observed in the in situ TEM movies. However, a quantification of coalescence frequencies requires more data which haven't been obtainable within the scope of this work.

5.7.4 A Sintering Model

All three sets of experiments show the presence of particles smaller than 5nm in diameter. The presence of these particles after 5 hours of sintering even under severe conditions, high temperature and high partial pressure of water vapor, must mean that they are fixed to the support. This is most clearly seen in movies as shown in Figs. 5.20 and 5.31. In these movies the larger particles are observed to migrate along edges on the support. For the smallest particles in the ensemble, vacancies or line defects in the support might be enough to trap the particles. If smaller particles are prevented from migrating the only way they can coalesce is if they are picked up by larger particles during their migration, which is also the observation in the in situ TEM movies and shown schematically in Fig. 5.35.

The models presented in Chapter 4 do not include a term accounting specifically for the trapping of the smallest particles. The present in situ results show that the carrier plays a significant role in immobilizing the particles, and that this immobilization is stronger for the smallest particles. An activation barrier increasing with decreasing particle diameter should be included in the particle diffusion coefficient to account for the immobility of small particles. Hence the particle diffusion coefficient vs. particle radius would have a local maximum at a finite value. From Figs. 5.23 and 5.24 this maximum seems to be around 10nm. Particles larger than this value are virtually immobile as predicted by the Gruber model. When explaining data for catalysts that have been sintered for a longer period of time, e.g. several days, such a parameter may not be as important as all small immobilized particles may have been picked up.

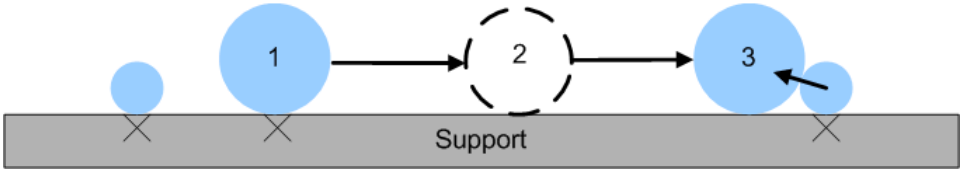

Figure 5.35: Schematic of the migration and coalescence events. While smaller particles are most often observed to remain stable on the support, possibly trapped by defects, the particles larger than ca. 8nm migrate and absorb smaller particles they encounter during their migration. The large particles remain stable for a period of time, 1, after which they rapidly migrate, 2, and become immobile again and/or may coalesce with other particles, 3.

To account for the observations described above, an factor accounting for the trapping of particles to the support has to be included in a model. This factor has to be larger for small particles than for big particles. A model for the mobility of metal particles must then incorporate the following statements:

- The ability of a metal particles to release itself from their anchoring site on the support is particle size dependent
- The smaller the particle, the larger the barrier
- For particles larger than a certain size, the diffusivity scales with size as suggested by the Gruber formula

The first statement is substantiated by the observation of small immobile particles on the support. Even after sintering for longer periods of time in severe environments. In the online experiments, the smallest particles were observed to move the least. The second statement is substantiated by Figs. 5.23 and 5.24. Even though the statistics in these plots are poor, the trend is that small particles remain immobile while particles larger than ca. 8nm in diameter migrate the longest distances. From these studies, the third statement is hard to prove. Due to the short sintering times used, particles do not grow to diameters larger than ca. 25nm. But as experimental evidence in the literature shows that particles do not grow to infinite sizes such a statement seems to be justified.
The statements above suggest that the diffusion coefficient of metal particles take the form

$$D_c = f_{release}(r) \cdot D_{c,gruber} = f_{release}(r) \cdot 4.818 \cdot D_s \cdot \left(\frac{a}{d}\right)^4 \qquad (5.19)$$

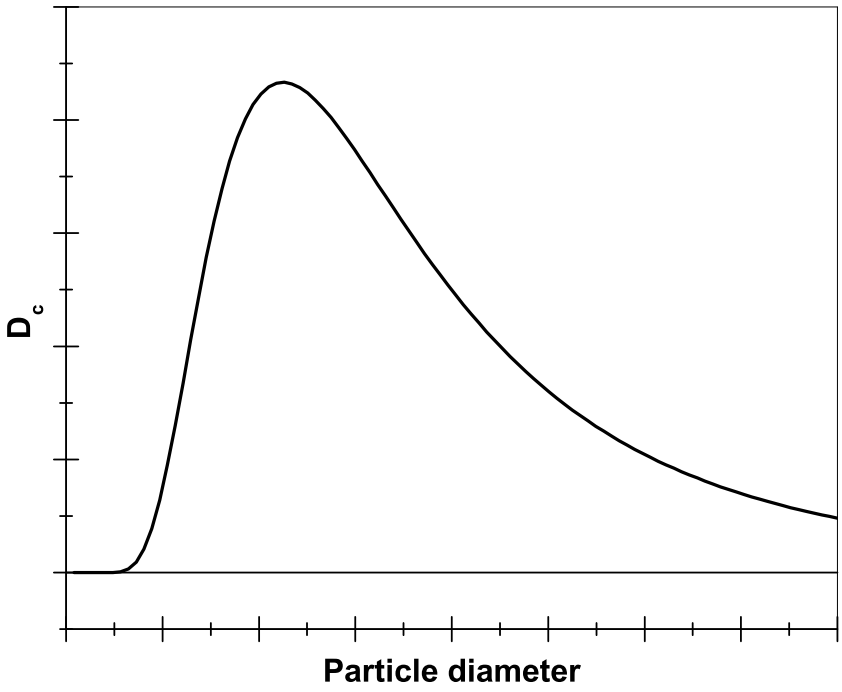

Figure 5.36: Particle diffusion coefficient vs. particle diameter as predicted by Eqn. 5.19.

where $f_{release}(r)$ approaches zero as the particle diameter approaches zero, and $f_{release}(r)$ approaches one as the particle diameter approaches infinity, i.e. Eqn. 5.19 approaches a Gruber-type behavior for large particles. Such a model is sketched in Fig 5.36 showing the particle diffusion coefficient as a function of the particle diameter.

Based on the data, no apparent differences in the coalescence mechanism were observed when changing the atmosphere composition or the temperature. The only difference is the frequency with which coalescence events occur. Since this frequency is in all cases very low, a small change is difficult to quantify. The observed time scale for the individual coalescence events agrees well with that reported in the literature [42, 64, 65].

If defects on the support do indeed stabilize particles, the higher electron beam intensity could in fact decrease the particle mobility due to the formation of defects in the support. On the other hand, in the extreme case it is possible to induce changes in the metal particles, that might enhance the particle diffusivity. Mobility of surface atoms has been observed for gold particles in vacuum in earlier published work [98] so surely the electron beam

has an effect on the mobility of nano-particles. However in that case, images were acquired with 100 times the electron dose rate as used in this study.

To make the model quantitative more experimental data are needed on well defined supports containing few and well defined anchoring sites. On such supports a higher degree of particle mobility is expected than was found for the commercial system containing a high number of anchoring sites. As the present study was aimed at commercial steam reforming catalysts, such a study is not within the scope of this study.

5.8 Conclusion

The observation of medium-sized particles being more mobile than smaller ones may help rationalize sintering phenomena in a wide range of supported nanoscale metal/oxide systems. In the context of the present study, the long tail in the PSD, see Fig. 5.18, can now be explained by migration and coalescence of the larger particles in the distribution. The migration and coalescence of large particles may even lead to formation of large particles, as described by Agnelli [46] and Harris [99]. The in situ TEM observations are consistent with a recent study of Au clusters on amorphous alumina, where it has been implied that larger clusters may be more mobile than smaller ones [100]. These observations were based on TEM images acquired before and after annealing. The PSD became bimodal, which could be reproduced by a Monte Carlo simulation based on particle trapping to surface defects. For Ni supported on alumina a similar phenomenon was observed [80]. When coating the catalyst with a thin layer of carbon and sintering it, tracks were observed next to the particles. In most cases the tracks left by the largest particles were longer than the tracks left by the smaller particles indicating that the larger particles migrated further than the smallest particles. Carrey *et al.* found that Au particles on Al_2O_3 start diffusing when reaching a given critical size. The present in situ TEM movies provide further evidence for the phenomena observed by these authors. Likewise Richardson and Crump found that even after 30hrs of sintering in helium at 873K small particles around 2nm were still present in the distribution and had become stabilized [43]. Wallace *et al.* [84] concluded that defect sites on TiO_2-SiO_2 mixed oxide films were responsible for the stabilization of Au clusters, while the sintering rate increased with temperature, the introduction of surface defects decreased the sintering rate in agreement with the present study.

All particle size distributions obtained in this work could be well fitted using the log-normal distribution function. All sintering events observed in the in situ TEM movies were of the particle migration and coalescence type. However, the time interval over which the movies were acquired might have been too short to observe any change in particle sizes due to an Ostwald ripening process. Based on the observations done here, it is concluded that

sintering by particle migration and coalescence produces a size distribution that has a tail on the large diameter side of the peak, and that large particles may develop by coalescence among the larger particles in the ensemble.

In summary, the findings were the following:

1 The simple Gruber model is not supported for particles smaller than 8nm in diameter by online observations.

2 Particles smaller than ca. 8nm in diameter can be trapped on the surface of the support material.

3 A qualitative model has been suggested that incorporates the statements above.

4 The trends predicted by the Sehested equation are observed in the low pressure regime relevant for in situ TEM experiments.

5 Qualitatively, the coalescence events observed in the in situ TEM movies can account for the changes observed in the particle size distributions in the offline experiments. Better statistics are needed to make a quantitative connection.

Chapter 6

Scanning Electron Microscopy of Flat Model Catalysts

In recognition of the fact that the statistics obtainable using in situ TEM are poor, other techniques are sought to acquire supplementary supporting evidence for the conclusions drawn at the end of Chapter 5. To further complicate matters, nickel is a very reactive metal and exposing nickel containing catalysts to ambient atmosphere significantly affects the results. Hence different, more noble, metals were chosen for the experiments described below.

As described in Section 3.3, modern SEM's are capable of resolving particles of sizes of interest in catalysis. As SEM is a surface technique, the metal particles have to be present on the outer surface of the samples or close to the surface to be detected with high resolution. This can be accomplished by depositing the metal precursor/particles on a flat substrate. Flat slabs of metal oxide substrates like the ones used for supports in industrial catalysis are available off the shelf.

One of the most complex things about studying industrial catalysts is their tortuous pore structure. Industrial catalysts have a complicated system of macro-, meso-, and micropores keeping the active metal particles well dispersed under reaction conditions. Such structures are difficult to study with surface techniques like SEM. Hence, for these studies, a series of flat model catalysts were prepared.

6.1 Model System Preparation

As substrates, SiO_2 and α-Al_2O_3 in wafer form from MTI Corporation were used. The SiO_2 was amorphous (fused) and the α-Al_2O_3 single crystals was cut in the $\langle 11\bar{2}0 \rangle$ orientation. Both crystals were clear colorless materials polished to a surface roughness of $<$5Å. With the resolution of the scanning electron microscope the substrates were completely featureless.

Metal was deposited on the metal oxide wafers using an ion beam sput-

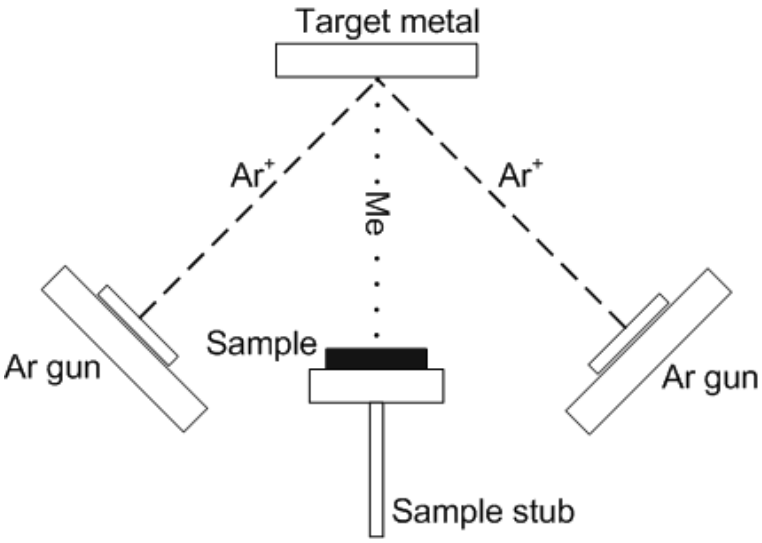

Figure 6.1: Ion beam sputtering setup. Two beams of argon ions hit a metal substrate. As metal atoms are detached from the substrate they deposit on the sample forming a film of homogeneous thickness.

tering machine (IBS) from South Bay Technologies. Using IBS for metal deposition keeps the sample surfaces clean and the metal can be deposited with a homogeneous thickness on the substrate. The wafer was placed on a sample stub with a piece of double sticky tape and placed in the deposition chamber in a multi-directional sample holder and turned upside down so no metal was deposited while aligning and adjusting the argon guns. The target metal was placed on a carousel for holding 3 sputtering targets. The chamber was evacuated to a base pressure better than 5×10^{-6}mbar. After evacuation of the deposition chamber the acceleration voltage in the argon guns was increased to ca. 7kV. The flow of argon was adjusted through one gun at a time until the ion current was 2mA in each gun. The height of the target metal was adjusted so the two Ar beams hit the same point. This was done by aiming the guns at a transparent dummy target where the position of the beams could be observed. When the height was set, the target metal carousel was turned to the target metal and the wafer sample was turned around so metal could be deposited. During metal deposition the sample holder was rotated and tilted continuously to assure homogeneous deposition thickness. During metal deposition, the deposition rate was monitored by a quartz microbalance placed at an angle to the sample. Before metal deposition, the quartz microbalance was placed in the sample position for calibration. The metal sputtering targets used for deposition were 99.99% purity from Goodfellow.

6.2 Image Analysis

Particle sizes were determined using PGT's Spirit program. The images were first filtered using a median filter. The median filter removes impulse noise in the image by replacing the center pixel with the median value of the neighboring pixels. The image was segmented in contrast into a binary image. Pixels having an intensity above a certain value were assigned the value one, pixels having intensity below that value was assigned the value 0. From the segmented image a binary mask is extracted. After filtering and segmentation, a filter is applied to the image discriminating features in the binary mask based on their size and shape. Features having an aspect ratio above 1.5 were not allowed to pass, this eliminates overlapping particles from the count since overlapping particles would appear elongated in the image. The images were inspected to determine the size of the smallest particles. In the count features smaller than this minimum size were not allowed to pass, features smaller than this minimum were interpreted as noise. Features that pass the filter are interpreted as particles and included in the particle size distributions. Particles smaller than the minimum size may be present in the ensemble, but as the size of these features in the image approach the pixel size, a limit has to be set to be certain that only particles were counted and not noise. For the particle size distributions the particles were placed in 1nm wide bins.

An advantage of the flat model catalysts is that the particle coverage is similar throughout the sample, hence, the area imaged between consecutive treatments does not need to be the same. The behavior of the particles is expected to be the same as the morphology of the substrate does not vary from area to area. Large data sets can be collected fast as appropriate areas do not need to be sought. This results in particle size distributions with good statistics.

6.3 Treatments of Model Catalysts

After preparation, the samples were calcined for one hour in a Thermolyne muffle furnace in atmospheric air at 840mbar. The calcination procedure has earlier been shown to give better dispersion of the metal particles after reduction than without the calcination step [101] and produce particles of smaller diameter. After calcination the samples were reduced in a Lindberg/Blue tube furnace in flowing hydrogen at ca. 50sccm/min at 840mbar. The calcination and reduction temperatures varied from sample to sample. Fig. 6.2 shows the results of these two treatments for palladium on alumina. After calcination, palladium oxide is present on the surface of the substrate as a film of homogeneous thickness. After reduction the palladium oxide film is reduced and forms spherical particles. The palladium oxide layer still

appears smooth after reduction. That particles are spherical is based on Fig. 6.2(c). The surface of the reduced substrate was marked with a scribe, and the sample was imaged with no further treatment. Where particles were scraped off the surface they agglomerated into clumps of particles. As all of these particles appear as spheres and none are observed having edges, see Fig. 6.2(c), it is concluded that they are also present on the surface of the substrate as spheres.

The sintering treatments of the flat model catalysts were carried out in a Lindberg single zone tube furnace. The samples were placed in an alumina tray and inserted into the center of the heating zone. A 7% H_2/N_2 was used as the sintering gas. The gas was flowed through the tube either directly to the tube furnace or through a bubbler if water vapor was required. The samples were sintered at 840mbar. The line from the bubbler to the tube furnace was lined with heating tape to avoid recondensation on the tube walls. The temperature of the bubbler and lining was adjusted to control the vapor pressure of water according to the Antoine equation. The temperature was controlled using the built in thermocouple which was calibrated against a second thermocouple placed in the center of the tube. The temperature was increased slowly so the temperature controller would not overshoot the target temperature. The time when the temperature reached the sintering temperature was chosen as t=0. After treatment, the furnace and sample was cooled in flowing gas. After the temperature of the furnace had reached ambient temperature, the sample was removed from the furnace.

6.4 Results of Flat Model System Studies

The Au/SiO_2 sample were prepared using IBS as described above. The sample was calcined for 1 hour at 773K ramping up at 10K/min. Even though the formation of an oxide is not expected, the procedure outlined above was followed for consistency. After calcination the sample was reduced at 873K ramping up at 10K/min. After calcination and reduction the sample was imaged and particle size distributions determined. The sample was sintered at 973K in 7%H_2 in N_2 for 6 hours at a time. As sintering is strongly dependent on temperature the effects of the ramp up and cool down periods are expected to be negligible. As the samples are flat, it is not necessary to ramp up the temperature slowly as any water vapor will evaporate quickly from the surface as opposed to evaporation from the pores in a porous sample.

Backscatter electron images were used for the particle size distributions. The high atomic number of gold compared to silicon and oxygen makes the gold particles appear bright in the BSE images and particles can easily be measured automatically, see Fig. 3.16. In the automatic counting routine, the minimum feature cut-off was chosen as 2nm.

Fig. 6.3 shows characteristic backscatter electron images of gold particles

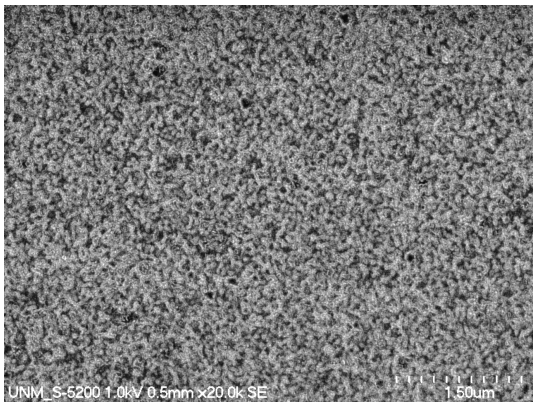

(a) PdO/Al_2O_3 after calcination at 973K.

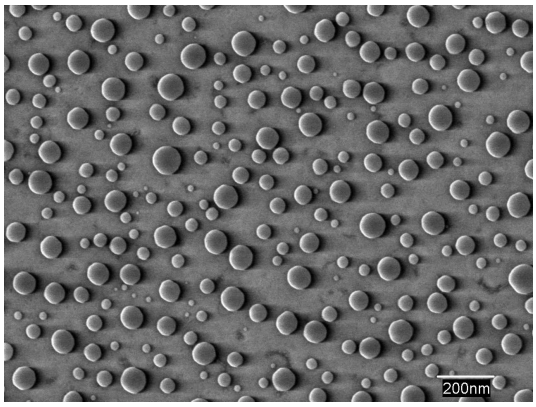

(b) Pd/Al_2O_3 after reduction at 1173K.

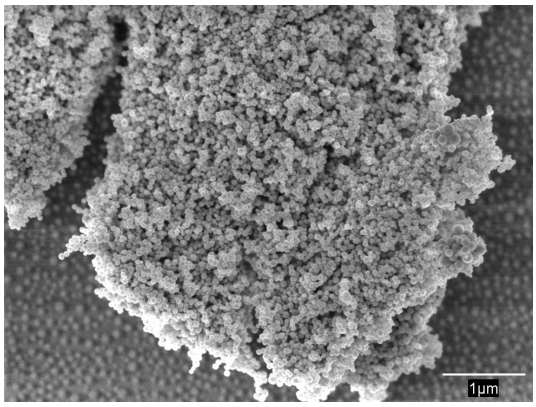

(c) Pd/Al_2O_3 after reduction at 1173K.

Figure 6.2: Secondary electron images of stages of the model catalyst preparation process. The sample is calcined in air at 973K and reduced in flowing hydrogen at 1173K. Note the difference in magnification. When the sample is calcined, Fig. 6.2(a), a homogeneous film of PdO is formed. As the sample is reduced, Fig. 6.2(b), the PdO film breaks up into particles. When scraped from the substrate surface, Fig. 6.2(c), the Pd particles form agglomerates of spherical particles.

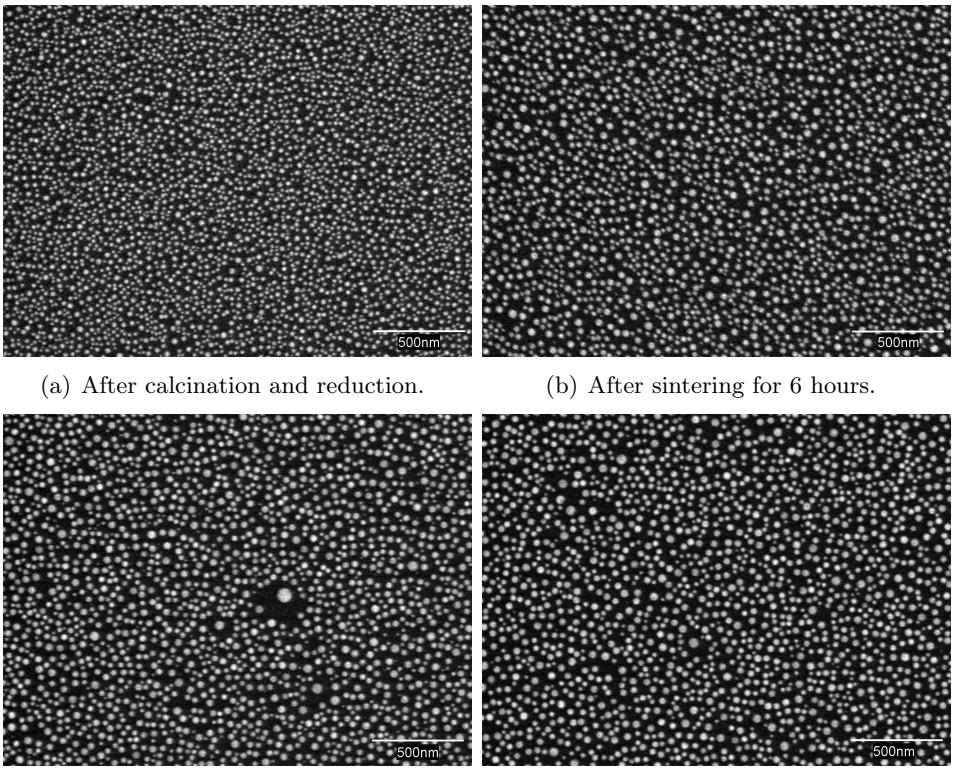

(a) After calcination and reduction.

(b) After sintering for 6 hours.

(c) After sintering for 12 hours.

(d) After sintering for 18 hours.

Figure 6.3: Representative backscatter electron SEM images of 4 different areas of gold on silica as a function of sintering time. Large particles are formed when treating the sample in hydrogen. The regions around the largest particles are depleted suggesting that that large particles have collected the smaller particles. In regions where no large particles are found, the distribution does not sem to vary from region to region.

on silica. After calcination and reduction the sample consists of an ensemble of gold particles distributed homogeneously throughout the sample. The particle size distribution is almost symmetric with a mean particle diameter of 20.3nm and a standard deviation of 5.8nm. The distribution has small tails on both sides of the peak in the particle size distribution. Even though the distribution looks truncated on the small diameter side of the peak, no features smaller than the included particles were found by careful inspection of the images.

As the sample is sintered, the peak in the distribution moves to the right and starts to show bimodality, see 6.4(a). After 6 hours of sintering the mean particle diameter is 25.8nm and the standard deviation is 7.1nm. The upper cut-off of the distribution moves from ca. 40nm after calcination and

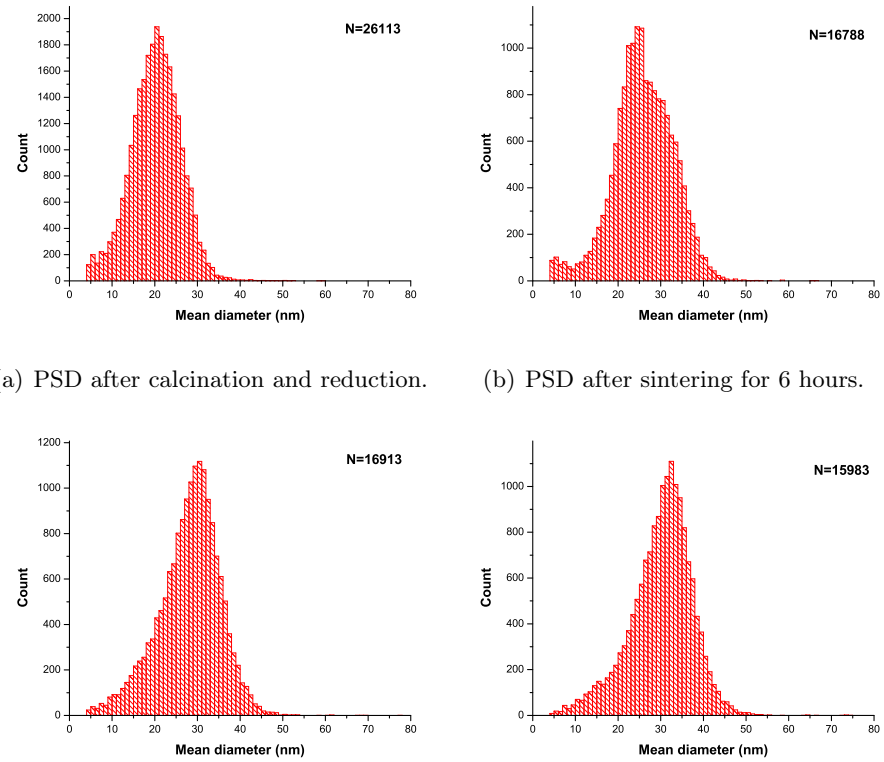

(a) PSD after calcination and reduction.

(b) PSD after sintering for 6 hours.

(c) PSD after sintering for 12 hours.

(d) PSD after sintering for 18 hours.

Figure 6.4: Particle size distributions for gold particles on silica support.

reduction to ca. 45nm after 6 hours of sintering, see Fig. 6.4(b).

After 12 hours at 973K, the bimodality in the particle size distribution has disappeared, see Fig. 6.4(c). The small diameter side of the peaks decreases to 0 at around 4nm, hence the size of the smallest particles in the distribution are still around 4nm, but they have decreased in number. Instead the distribution starts to develop a tail to the large diameter side while still having a significant tail on the small diameter side. The mean particle diameter is 28.0nm and the standard deviation is 7.2nm. The cut-off on the large diameter side of the peak is around 50nm.

After 18 hours of sintering, the mean diameter has increased to 30.1nm and the standard deviation to 7.3nm. The tail on the small diameter side of the peak still extends all the way to 4nm and the tail on the large diameter side of the peak becomes longer extending to ca. 50nm, see Fig. 6.4(d).

After sintering a few large particles are formed while a population of small particles still exists. Around the large particles, depleted regions are found. Either the original particle population in these depleted regions has

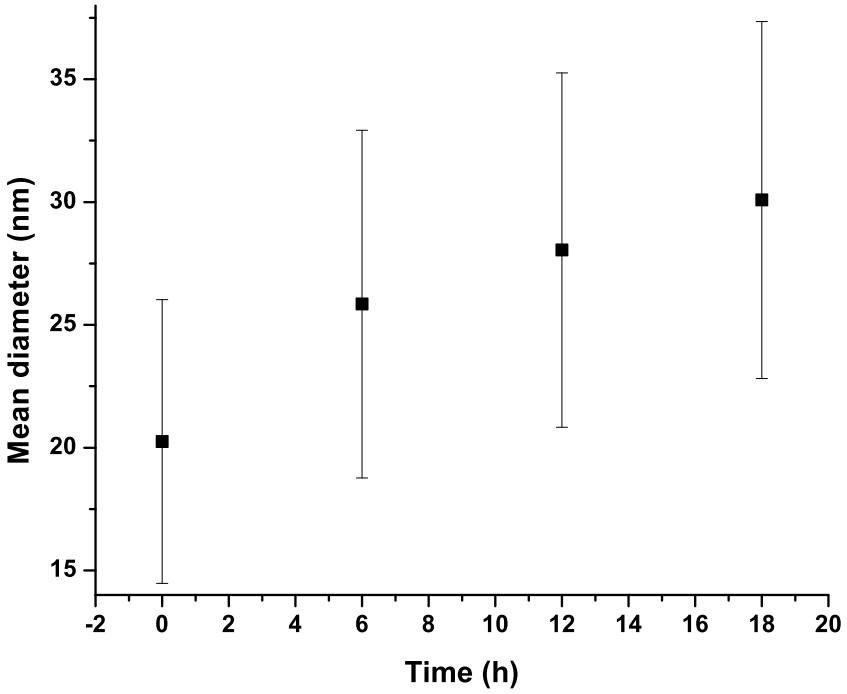

Figure 6.5: Mean particle diameter and standard deviation for Au on SiO_2.

migrated and coalesced to form one large particle or one mobile particle has collected all the particles in its vicinity. The former statement seems unlikely as the phenomenon is only observed locally and not throughout the whole sample. The number of particles decreases over the first 6 hours after which the number of particles remains almost constant, see Fig. 6.4. However few of these regions are found and the effect on the number of particles will be small and the mean particle diameter only changes little after 6 hours of sintering, see Fig. 6.5.

The total number of particles only changes significantly over the first sintering period. During the last two sintering periods the population is almost constant, but the mean particle diameter still changes, but only little. Looking at the images in Fig. 6.3, the most obvious observation is the formation of the large particles resulting in depleted regions around these large particles. It seems unlikely that the formation of the large particles is a result of Ostwald ripening as they are only observed locally. If Ostwald ripening was responsible the large particles should be formed all over the sample. A few highly mobile particles picking up other particles seems like

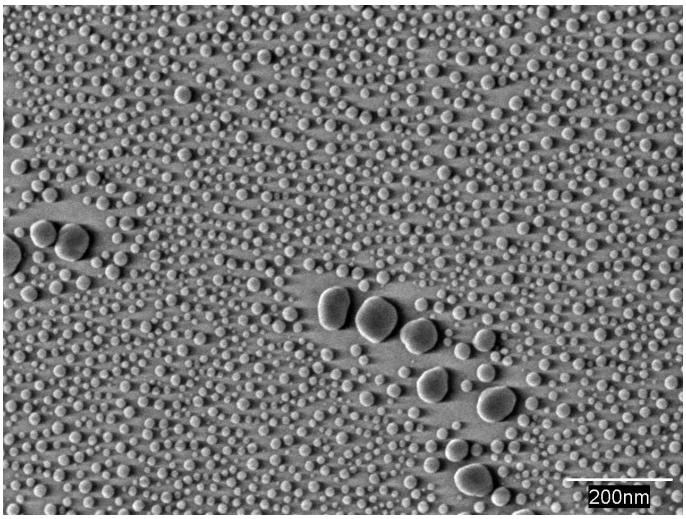

Figure 6.6: Palladium particles on alumina support. Large particles are observed with depleted regions around them.

a more plausible explanation. One particle undergoing Brownian motion could deplete a local area for particles and again become immobile as it has grown. The small increase in mean particle diameter could be a result of the formation of the large particles.

Over the first sintering period the number of particles changes significantly. This could indicate that during this period the particles are finding their equilibrium, some coalesce with each other and others get stuck to potential energy minima on the surface. These latter particles are the small particles that are found to persist in the particle size distributions.

The observation of large particles was not isolated to Au/SiO_2. A similar phenomenon was observed for Pd/Al_2O_3. Fig. 6.6 shows a secondary electron SEM image of palladium on alumina. Pd particles up to around 80nm in diameter with depleted regions around them are formed after calcination and reduction. Only few of these large particles are observed, hence they do not show up prominently in the particle size distribution, see Fig. 6.7. When the Pd/Al_2O_3 sample was observed at high magnification, as shown in Fig. 6.8, tracks are found on the support. These tracks were most frequently found to end at the largest particles, whereas no tracks were found at the smallest particles. Goeke found that Pd particle supported on alumina left trails [101] at 1173K in vacuum. These trails were attributed to the migration of the palladium particles. The lack of trails at the small Pd particles suggests that they are immobile during the treatment.

Comparing the results of the flat model samples with the in situ TEM data, two common observations are done:

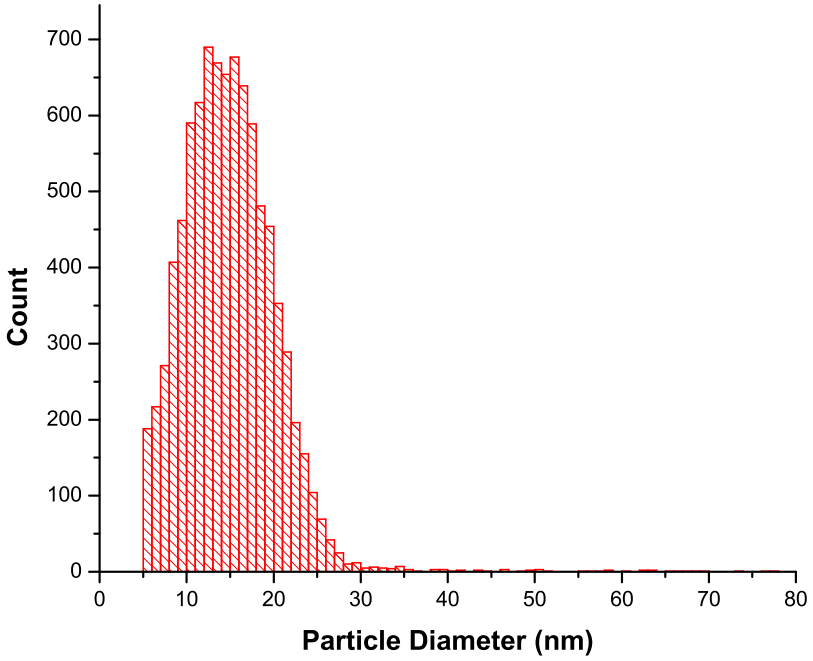

Figure 6.7: Particle size distribution of palladium particles on alumina after calcination and reduction.

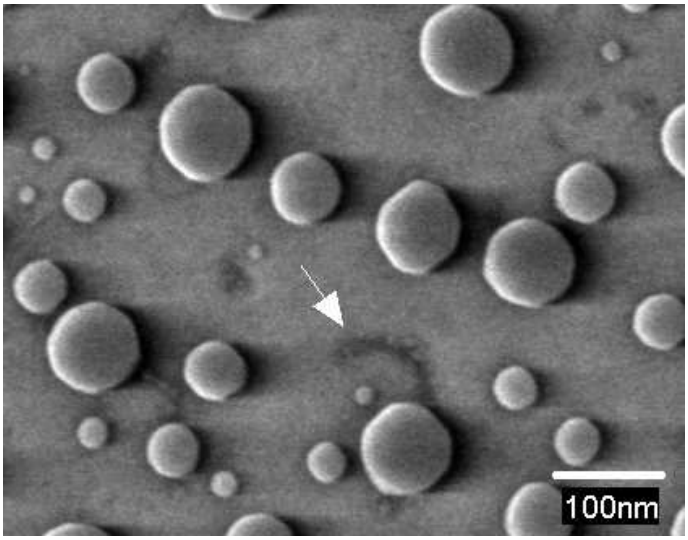

Figure 6.8: Magnified view of the lower part of Fig. 6.2(b). Particles larger than 100nm in diameter are found to coexist with particles ca. 5nm in diameter. Tracks on the support are found ending at the largest particles whereas no tracks are found near the smallest particles.

1 In both cases particles significantly larger than the average value are found.

2 In both cases particles ca. 5nm in diameter and smaller are found to persist after sintering.

However one has to be careful with this comparison, as the systems, the atmosphere and the temperature are different. The flat model supports do not contain the same degree of complexity a the industrial $MgAl_2O_4$ and hence not the same amount of anchoring sites. The interaction between the metal particles and the oxide support is most likely also very different for the different systems, making both the anchoring energy and the diffusion barriers different. Hence the size range of the intermediate particles that were found to be mobile in the in situ TEM studies may be different for the flat model catalyst. Such phenomena need to be further pursued through in situ SEM studies under a controlled atmosphere.

Future experiments with flat substrates could further shed light on the sintering phenomenon. Experiments at varying total pressure could verify the total pressure dependence in Eqn. 4.30. A controlled defect density could be introduced in the substrates to clarify the nature of the binding of small particles to such sites. Flat substrates could also be thinned to electron transparency for in situ TEM studies to remove more of the complexity found in the powder samples studied in Chapter 5. Interplay between real industrial systems and model systems may provide enough information to help limit sintering of supported heterogeneous catalysts.

Chapter 7

Conclusions and Outlook

Sintering is observed to occur via particle migration and coalescence when a nickel catalyst supported on magnesium aluminum spinel is exposed to atmospheres resembling those found in a steam-reforming reactor at high temperatures. Particles <8nm are observed to remain immobile on the support while migration of particles larger than ca. 8nm was observed more often. Most of the particles, however, remain immobile while only a few migrate. Diffusion coefficients can vary over a wide range for similar sized particles depending on the local environment of the individual particle, hence deriving diffusion coefficients for particles of a certain particle diameter will only yield an average for that diameter, not an absolute value. It is proposed that particles remain immobile due to interactions with the support on which they become trapped on anchoring sites and remain stable for an extended period of time until absorbed by larger migrating particles.

Classical theory predicts that sintering by particle migration and coalescence should produce a particle size distributions with a log-normal shape with a tail to the large diameter side. This conclusion is further substantiated by the results of the in situ TEM experiments. All offline and parameter experiments produced particle size distributions of a log-normal shape and the online experiments showed sintering occurring by the particle migration and coalescence mechanism. However, the time scale of the online in situ TEM experiments was short compared to experimental data found in the literature. Prolonging the experiments might provide evidence for sintering by the Ostwald ripening process not observed in the present data set. As stated in Chapter 4, it has been argued that this mechanism might also produce a log-normal shaped particle size distribution. Further experiments carried out over longer periods of time have to be carried out to pursue this aspect.

Even though much of the data presented here points to contradictions with the theory proposed by Gruber for particles smaller than ca. 8nm on an industrially relevant support, the Gruber model may still explain sintering of supported metal catalyst treated for longer periods of time where particles

grow to sizes larger than those studied here and has successfully explained long term sintering experiments. The in situ TEM studies are conducted over the first small fraction of the catalysts lifetime. An industrial catalyst is expected to have a lifetime of several years, the in situ studies were conducted over only hours. We have merely looked at the infancy of the catalyst. The vast discrepancy in time scales has to be taken into account when comparing the present results with reactor tests and making interpretations in the context of the classical models as these in most cases are derived from long term sintering experiments. Even though there is a big difference in environment in the in situ TEM and an industrial reactor, the observed phenomena could be similar. If the mass transporting entities are indeed surface species, this will most likely not change from the in situ TEM conditions to the high-pressure reactor conditions. However, the coverage of the metal particles with such species may differ and the total pressure have an effect as predicted by the Sehested formula.

The mobility of particles were observed to occur in a discrete way as opposed to a continuous motion across the support surface. Particles migrated over relatively short periods of time after which they resided in a new position for a relatively long period of time. The effective particle diffusion coefficient is thus much lower than the one calculated from the short movies showing migration.

Obviously there are big differences between using flat model systems consisting of single crystals or fused metal oxides. The flat samples do not contain the complexity of the industrially relevant supports. The method of metal deposition used in this study is very different from that used for industrial catalysts. While industrial catalysts are prepared via a chemical route, the flat substrates were prepared using a physical route. As the chemistry of the resulting sample is the same, it seems fair to compare the results and as has been shown, some of the observed phenomena are the same, e.g. the formation of large particles.

A model is proposed where small particles are anchored to the support and only coalesce as a result of being absorbed by larger particles. When particles grow even larger, a classical Gruber type model is perhaps more suitable for describing the particle mobility. To determine quantitative properties of such a model, better statistics are needed as are more well-defined supports with a known defect concentration, and more information on the nature of the defects. For obtaining better statistics, a model system could be better suited system than a highly optimized industrial catalyst.

If a support can be developed that can prevent particles from growing into a critical size regime where they can no longer be trapped by the support defects, the deactivation of catalysts due to sintering by particle migration and coalescence may be limited. The main challenge seems to be the incorporation of defects in the support in a controlled fashion without changing other valuable features of the support material.

Extrapolating the model proposed by Sehested [11, 49] to the conditions in the in situ TEM studies fits the data well. However, different values of the constant C have to be used for different systems and conditions. As the partial pressure of hydrogen appears in the denominator in 1/2 power the expression depends on the total pressure. The successful predictions of the model over a wide span in pressure is a further substantiation of the assumptions on which the model builds. The experiments against which the model was originally tested, were carried out at no less than one bar and at pressures up to 40bar. Further these experiments were carried out in reactors for longer periods than the time scales usable for in situ TEM experiments. The pressure gap is challenging to circumvent using in situ TEM. New developments in high pressure stages and/or in situ cells are needed to increase the pressure even further. However, compared to classic high vacuum TEM, a big step has been taken going from UHV conditions to the millibar regime. The time issue is a matter of the experimentalist's patience and the stability of the support. At the elevated temperatures and wet atmosphere under which the present studies were carried out, the catalyst is a very dynamic system, support plates shift around, and sometimes fall off the grid, making it difficult to monitor the same region over and extended period of time. Perhaps future developments in TEM grids can remedy this, e.g more oxidation resistant stainless steel alloys.

To further support and quantify the model proposed at the end of Chapter 5, more migration data is needed. Such data could be acquired on a model type catalyst consisting of large platelets without the complexity of the industrial catalyst, but still prepared in the same way and still electron transparent for TEM studies. Such samples might also contain fewer defects leaving more particles free for migration. However the trade-off is that the samples would move further away from industrial catalysts. Experiments on a longer time scale could determine if small particles will be present, or if they will eventually be exhausted by coalescence providing further evidence for the particle migration and coalescence mechanism as opposed to Ostwald ripening.

The main result of this work is that particles smaller than ca. 8nm can remain anchored on the support material when exposed to conditions similar to those found in an industrial reactor, and only coalesce when other particle migrate close to their position and absorb them.

Appendix A

Fitting Values

	y_0	x_c	w	A
5% H_2O/H_2, after reduction	0	2.68	0.35	0.94
5% H_2O/H_2 873K, after 65 minutes	0	2.90	0.32	0.98
5% H_2O/H_2 873K, after 147 minutes	0	3.15	0.32	0.95
5% H_2O/H_2 873K, after 253 minutes	0	3.20	0.29	0.93
5% H_2O/H_2 873K, after 339 minutes	0	3.46	0.34	0.95
5% H_2O/H_2 873K, after 433 minutes	0	3.48	0.34	0.95

Table A.1: Fitting values for the log-normal fits in the experiment carried out in 5% H_2O in H_2 at 873K shown in Fig. 5.6.

	y_0	x_c	w	A
5% H_2O/H_2, after reduction	0	2.45	0.37	0.95
5% H_2O/H_2 973K, after 110 minutes	0	4.11	0.29	0.90
5% H_2O/H_2 973K, after 177 minutes	0	4.31	0.52	1.03
5% H_2O/H_2 973K, after 252 minutes	0	5.19	0.39	0.97
5% H_2O/H_2 973K, after 328 minutes	0	5.49	0.44	0.99
5% H_2O/H_2 973K, after 423 minutes	0	5.54	0.39	0.98

Table A.2: Fitting values for the log-normal fits in the experiment carried out in 5% H_2O in H_2 at 973K shown in Fig. 5.7.

5% H_2O/H_2 873K	C=9·10^7
5% H_2O/H_2 923K	C=4·10^9

Table A.3: Fitted values for the constant C in Eqn. 5.1 for that data acquired in parameter experiments. The fits are shown in Figs. 5.8 and 5.9.

.

	y_0	x_c	w	A
2mbar H_2O/2mbar H_2 773K	0	3.64	0.40	0.98
9mbar H_2O/1mbar H_2 773K	0	3.57	0.28	0.91

Table A.4: Fitting values for the log-normal fits in Fig. 5.11.

	y_0	x_c	w	A
0mbar H_2O/2mbar H_2 1023K, before sintering	0	2.70	0.34	0.98
0mbar H_2O/2mbar H_2 1023K, after sintering	0	2.88	0.32	0.91

Table A.5: Fitting values for the log-normal fits in Fig. 5.12.

	y_0	x_c	w	A
2mbar H_2O/2mbar H_2 923K, before sintering	0	2.71	0.31	0.94
2mbar H_2O/2mbar H_2 923K, after sintering	0	3.55	0.37	0.94

Table A.6: Fitting values for the log-normal fits in Fig. 5.14.

	y_0	x_c	w	A
9mbar H_2O/1mbar H_2 923K, before sintering	0	2.88	0.32	0.91
9mbar H_2O/1mbar H_2 923K, after sintering	0	5.93	0.36	1.00

Table A.7: Fitting values for the log-normal fits in Fig. 5.16.

	y_0	x_c	w	A
2mbar H_2O/2mbar H_2 1023K, before sintering	0	2.85	0.31	0.95
2mbar H_2O/2mbar H_2 1023K, after sintering	0	7.71	0.45	0.91

Table A.8: Fitting values for the log-normal fits in Fig. 5.18.

2mbar H_2O/2mbar H_2 923K	C=2·10^9
9mbar H_2O/1mbar H_2 923K	C=6·10^9
2mbar H_2O/2mbar H_2 1023K	C=1·10^{12}

Table A.9: Fitted values for the constant C in Eqn. 5.1 for that data acquired in offline experiments. The fits are shown in Fig. 5.34

Appendix B

Comparison Between Atmospheric Pressure Experiments and In Situ Data

In this appendix, the values of the constant C in Eqn. 5.1 are calculated from experiments carried out at atmospheric pressure and used for the conditions relevant for the environment in the in situ TEM.

B.1 From atmospheric pressure experiments

Data from [79]: Catalyst used: 9.5% Ni/Al_2O_3, support surface area = 203.6m^2/g.
Sintering conditions: 50 hours in 0.5bar H_2 and 0.5bar H_2O at 923K and 1023K.
Initial total surface area of Ni: 6.79m^2/g.
Ni surface area after 50hours sintering: at 923K=4.43m^2/g, at 1023K=2.34m^2/g.

B.1.1 Calculation of surface normalized mean Ni particle diameters

$$S = 4\pi r^2 \tag{B.1}$$

$$V = \frac{4}{3}\pi r^3 \tag{B.2}$$

$$r = 3 \cdot \frac{V}{S} \tag{B.3}$$

$$r_0 = \frac{3 \cdot 0.095 \cdot 1.12 \cdot 10^{-7} m^3/g}{6.79 m^2/g} = 4.7nm \Rightarrow d_0 = 9.4nm \tag{B.4}$$

$$r_{50h,923K} = \frac{3 \cdot 0.095 \cdot 1.12 \cdot 10^{-7} m^3/g}{4.43 m^2/g} = 7.2nm \Rightarrow d_{50h,923K} = 14.4nm \tag{B.5}$$

$$r_{50h,1023K} = \frac{3 \cdot 0.095 \cdot 1.12 \cdot 10^{-7} m^3/g}{2.34 m^2/g} = 13.6nm \Rightarrow d_{50h,1023K} = 27.3nm \tag{B.6}$$

B.1.2 Determination of constants

$$\bar{d} = \left[const. \frac{K_2 D_{OH-dimer} X \tau}{(1-X)A} \left(\frac{P_{H_2O}}{\sqrt{P_{H_2}}} \right) + \bar{d_0'}^7 \right]^{1/7} \Rightarrow \tag{B.7}$$

$$C = \left[\left(\frac{\bar{d}}{\bar{d_0}} \right)^7 - 1 \right] \frac{\bar{d_0'}^7 (1-X)A}{X\tau} \frac{\sqrt{P_{H_2}}}{P_{H_2O}} \tag{B.8}$$

with

$$C = const. \cdot K_2 \cdot D_{OH-dimer} \tag{B.9}$$

Assuming no change in support surface area and using [11]

$$\left[\left(\frac{\bar{d}}{\bar{d_0}} \right)^7 - 1 \right] = 1.051 \cdot 10^8 \cdot \exp \frac{-1.146 \cdot 10^2 \cdot 1000}{RT} \tag{B.10}$$

At 923K:

$$\begin{aligned} C_{923K} &= \left[1.051 \cdot 10^8 \cdot \exp \frac{-1.146 \cdot 10^2 \cdot 1000}{8.3144 J/(mole \cdot K) \cdot 923K} \right] \qquad \text{(B.11)} \\ &\quad \times \left[\frac{(9.4nm)^7 (1-0.095) 203.6 m^2/g}{0.095 \cdot 50h} \right] \left[\frac{\sqrt{0.5bar}}{0.5bar} \right] \\ &= 1.223 \cdot 10^{10} \qquad \text{(B.12)} \end{aligned}$$

In [11] it is indicated that the mechanism of sintering has changed when increasing the temperature to 1023K. Thus a value of C obtained from the ambient pressure experiments at 1023K cannot be transferred to the in situ TEM experiments where particle migration and coalescence has been shown to be the dominating sintering mechanism. However, a value of C can be determined from the in situ TEM data

Catalyst	T/K	P_{H_2}/bar	P_{H_2O}/bar	$d_{0,exp}$/nm	d_{exp}/nm
Ni/Al_2O_3	923	0.5	0.5	9.4	14.4(50h)
Ni/Al_2O_3	1023	0.5	0.5	9.4	27.3(50h)
$Ni/MgAl_2O_4$	923	0.002	0.002	3.1	4.4(5h)
$Ni/MgAl_2O_4$	1023	0.002	0.002	3.3	10.2(5h)

Table B.1: Atmospheric pressure and in situ TEM experimental values.

$$C_{1023K,i.s.} = \left[1.051 \cdot 10^8 \cdot \exp \frac{-1.146 \cdot 10^2 \cdot 1000}{8.3144 J/(mole \cdot K) \cdot 1023K}\right] \times \left[\frac{(3.3nm)^7(1-0.01)5m^2/g}{0.01 \cdot 5h}\right]\left[\frac{\sqrt{0.002bar}}{0.002bar}\right] \quad \text{(B.13)}$$

$$= 5.685 \cdot 10^{10} \quad \text{(B.14)}$$

B.2 Determination of mean particles diameters from in situ TEM data

$$\bar{d} = \left[\frac{CX\tau}{(1-X)A}\left(\frac{P_{H_2O}}{\sqrt{P_{H_2}}}\right) + \bar{d_0^7}\right]^{1/7} \quad \text{(B.15)}$$

Catalyst used: 1% $Ni/MgAl_2O_4$, support surface area = $5m^2/g$.
Sintering conditions: 5 hours in 0.002bar H_2 and 0.002bar H_2O at 923K and 1023K.
d_0=3.2nm.

$$\bar{d} = \left[\frac{1.223 \cdot 10^{10} \cdot 0.01 \cdot 5h}{(1-0.01)5m^2/g}\left(\frac{0.002bar}{\sqrt{0.002bar}}\right) + (3.13nm)^7\right]^{1/7} = 9.2nm \quad \text{(B.16)}$$

Conditions: 2mbar H_2, 2mbar H_2O, T=1023K, τ=5 hours, d_0=3.2nm

$$\bar{d} = \left[\frac{5.685 \cdot 10^{10} \cdot 0.01 \cdot 5h}{(1-0.01)5m^2/g}\left(\frac{0.002bar}{\sqrt{0.002bar}}\right) + (3.32nm)^7\right]^{1/7} = 11.4nm \quad \text{(B.17)}$$

The evolution in particle diameter is shown in Fig. B.15.

T/K	P_{H_2}/bar	P_{H_2O}/bar	$d_{0,exp}$/nm	d_{exp}/nm	d_{calc}/nm
773	0.002	0.002	3.2(!)	4.4	6.1
773	0.009	0.001	3.2(!)	4.1	7.9
923	0.002	0.002	3.1	4.4	9.2
923	0.009	0.001	3.4	6.4	12.0
1023	0.002	0.002	3.3	10.3	11.4

Table B.2: Comparison between in situ TEM experimental values and calculated values. Values marked with (!) are estimated.

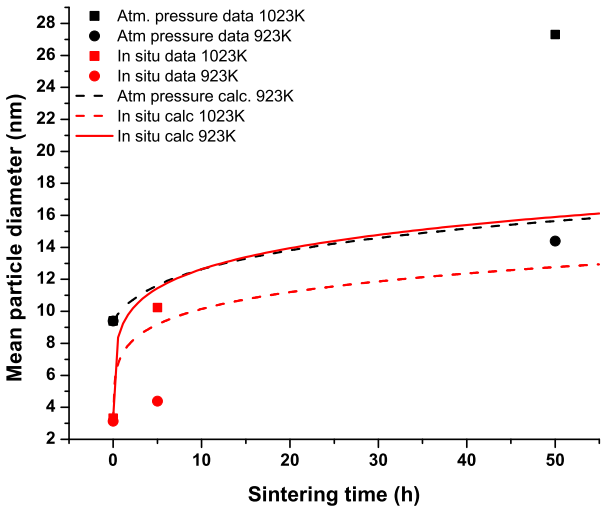

Figure B.1: Data fitted using the calculated constants and Eqn. B.15.

Bibliography

[1] *Chem.Eng. News* **83**, 41 (2005).

[2] I. Chorkendorff, J. W. Niemantsverdriet, *Concepts of Modern Catalysis and Kinetics* (Wiley-VCH, 2003).

[3] www.nacatsoc.org.

[4] J. R. Rostrup-Nielsen, *Catalysis - Science and Technolgy*, vol. 5 (Springer-Verlag, 1984).

[5] J. M. Thomas, W. J. Thomas, *Principles and Parctice of Heterogeneous Catalysis* (VCH, 1997).

[6] *Ullmann's Encyclopedia of Industrial Chemistry* (Wiley-VCH, 2002), sixth edn.

[7] www.indexmundi.com.

[8] H. S. Bengaard, *et al.*, *J. Catal.* **209**, 365 (2002).

[9] C. J. H. Jacobsen, *et al.*, *J. Mol. Catal. A* **163**, 19 (2000).

[10] R. v. Hardeveld, A. v. Montfoort, *Surf. Sci.* **4**, 396 (1966).

[11] J. Sehested, J. Gelten, I. Remediakis, H. Bengaard, J. Nørskov, *J. Catal.* **223**, 432 (2004).

[12] H. S. Bengaard, Methane Activation and Steam Reforming on Ni Surfaces A Density Functional Study, Ph. d. thesis, Technical University of Denmark, Lyngby (2001).

[13] A. K. Datye, *J. Catal.* **216**, 144 (2003).

[14] D. B. Williams, C. B. Carter, *Transmssion Electron Microscopy* (Plenum Press, 1996).

[15] J. Goldstein, *et al.*, *Scanning Electron Microscopy and X-ray Microanalysis* (Kluwer Acedemic/Plenum Publishers, 2003), third edn.

[16] J. B. Wagner, In situ transmission electron microscopy of catalyst particles, Ph. d. thesis, University of Copenhagen (2002).

[17] T. W. Hansen, Electron energy loss spectroscopy in the tem: A study of some carbon based materials, Master's thesis, University of Copenhagen (2001).

[18] J. C. H. Spence, *Experimental High-Resolution Electron Microscopy* (Oxford University Press, 1996), second edn.

[19] E. Merzbacher, *Quantum Mechanics* (Wiley, 1998), third edn.

[20] R. F. Egerton, *Electron energy loss spectroscopy in the electron microscope* (Plenum, New York, 1996), second edn.

[21] H. Hashimoto, T. Naiki, T. Eto, K. Fujiwara, *Japanese Journal of Applied Physics* **7**, 946 (1968).

[22] R. T. K. Baker, P. S. Harris, *J. Phys. E Sci. Instrum.* **5**, 793 (1972).

[23] R. T. K. Baker, *Catal. Rev. Sci. Eng.* **19**, 161 (1979).

[24] R. T. K. Baker, *J. Catal.* **37**, 101 (1975).

[25] E. D. Boyes, P. L. Gai, *Ultramicroscopy* **67**, 219 (1997).

[26] G. Wulff, *Z. Kristallogr.* **34**, 449 (1901).

[27] K. H. Hansen, Atomic-scale characterization of a model catalytic system, Ph.D. thesis, University of Århus (2001).

[28] D. R. Lide, ed., *Handbook of Chemistry and Physics* (CRC Press, 2004), 85th edn.

[29] C. J. H. Jacobsen, *J. Catal.* **200**, 1 (2001).

[30] Z. Kowalczyk, S. Jodzis, W. Raróg, J. Zielínski, J. Pielaszek, *Appl. Catal. A* **173**, 153 (1998).

[31] T. Hansen, *et al.*, *Science* **294**, 1508 (2001).

[32] J.-D. Grunwaldt, A. M. Molenbroek, N.-Y. Topsøe, H. Topsøe, B. S. Clausen, *J. Catal.* **194**, 452 (2000).

[33] P. L. Hansen, *et al.*, *Science* **295**, 2053 (2002).

[34] www.gel.usherbrooke.ca/casino/.

[35] D. Joy, *J. Microsc.* **161**, 343 (1991).

[36] P. Hovington, D. Drouin, R. Gauvin, *Scanning* **19**, 1 (1997).

[37] L. Reimer, C. Tollkamp, *Scanning* **3**, 35 (1980).

[38] P. Wynblatt, N. A. Gjostein, *Acta Metall.* **24**, 1165 (1976).

[39] C. H. Bartholomew, *Appl. Catal. A* **107**, 1 (1993).

[40] J. R. Rostrup-Nielsen, *Catal. Today* **18**, 125 (1993).

[41] J. Sehested, A. Carlsson, T. Janssens, P. Hansen, A. Datye, *J. Catal.* **197**, 200 (2001).

[42] P. Wynblatt, N. A. Gjostein, *Prog. Solid State Chem.* **9**, 21 (1975).

[43] J. T. Richardson, J. G. Crump, *J. Catal.* **57**, 417 (1979).

[44] H. K. Kuo, P. Ganesan, R. J. De Angelis, *J. Catal.* **64**, 303 (1980).

[45] C. H. Bartholomew, W. L. Sorensen, *J. Catal.* **81**, 131 (1983).

[46] M. Agnelli, M. Kolb, C. Mirodatos, *J. Catal.* **148**, 9 (1994).

[47] A. C. S. C. Teixeira, R. Giudici, *Chem. Eng. Sci.* **54**, 3609 (1999).

[48] C. T. Campbell, S. C. Parker, D. E. Starr, *Science* **298**, 811 (2002).

[49] J. Sehested, *J. Catal.* **217**, 417 (2003).

[50] P. Wynblatt, R. A. Dalla Betta, N. A. Gjostein, *The Physical Basis for Heterogeneous Catalysis*, E. Draglis, R. I. Jaffee, eds. (New York, 1975), p. 501.

[51] B. K. Chakraverty, *J. Phys. Chem. Solids* **28**, 2401 (1967).

[52] J. A. Horsley, C. H. Bartholomew, D. B. Dadyburjor, *Stability of Supported Catalysts: Sintering and Redispesion* (Catalytica Studies Division, 1991).

[53] R. Finsy, *Langmuir* **20**, 2975 (2004).

[54] Y. De Smet, L. Deriemaeker, R. Finsy, *Langmuir* **13**, 6884 (1997).

[55] Y. De Smet, D. Danino, L. Deriemaeker, R. Finsy, *Langmuir* **16**, 961 (2000).

[56] A. Sault, V. Tikare, *J. Catal.* **211**, 19 (2002).

[57] M. Zinke-Allmang, L. Feldman, S. Nakahara, B. Davidson, *Phys. Rev. B* **39**, 7848 (1989).

[58] G. Rosenfeld, K. Morgenstern, M. Esser, G. Comsa, *Appl. Phys. A* **69**, 489 (1999).

[59] P. Shewmon, *Metallurgical Society of American Institute of Mining, Metallurgical and Petroleum Engineers – Transactions* **230**, 1134 (1964).

[60] E. E. Gruber, *J. Appl. Phys.* **38**, 243 (1967).

[61] G. Somorjai, *Principles of Surface Chemistry* (Prentice-Hall, 1976).

[62] L. E. Willertz, P. G. Shewmon, *Metall. Trans.* (1970).

[63] K. Y. Chen, J. R. Cost, *J. Nucl. Mater.* **52**, 59 (1974).

[64] F. A. Nichols, W. W. Mullins, *Metallurgical Society of American Institute of Mining, Metallurgical and Petroleum Engineers – Transactions* **233**, 1840 (1965).

[65] F. A. Nichols, *J. Appl. Phys.* **37**, 2805 (1966).

[66] E. Ruckenstein, B. Pulvermacher, *J. Catal.* **29**, 224 (1973).

[67] E. Ruckenstein, B. Pulvermacher, *AIChE J.* **19**, 356 (1973).

[68] M. Jose-Yacaman, *et al.*, *J. Phys. Chem. B* **109**, 9703 (2005).

[69] C. G. Granqvist, R. A. Buhrman, *Appl. Phys. Lett.* **27**, 693 (1975).

[70] S. E. Wanke, P. C. Flynn, *Catal. Rev.-Sci. Eng.* **12**, 93 (1975).

[71] G. A. Fuentes, E. D. Gamas, *Catalyst Deactivation* (Elsevier, Amsterdam, 1991), vol. 68 of *Studies in Surface Science and Catalysis*, p. 637.

[72] G. A. Fuentes, E. Salinas-Rodriguez, *Stud. Surf. Sci. Catal.* **139**, 503 (2001).

[73] P. C. Flynn, S. E. Wanke, *J. Catal.* **34**, 400 (1974).

[74] S. Wanke, *J. Catal.* **46**, 234 (1977).

[75] A. K. Datye, Q. Xu, K. C. Kharas, J. M. Mcarty, *Accepted for publication in Catal. Today* (2005).

[76] R. Glang, *Handbook of Thin Film Technology*, Handbook of Thin Film Technology (McGraw-Hill Inc., 1970).

[77] P. J. Feibelman, *Phys. Rev. Lett.* **85**, 606 (2000).

[78] S. Horch, *et al.*, *Nature* **398**, 134 (1999).

[79] F. B. Rasmussen, J. Sehested, H. T. Teunissen, A. M. Molenbroek, B. S. Clausen, *Appl. Catal. A* **267**, 165 (2004).

[80] E. Ruckenstein, S. H. Lee, *J. Catal.* **86**, 457 (1984).

[81] P. Stone, S. Poulston, R. Bennett, M. Bowker, *Chem. Commun.* p. 1369 (1998).

[82] M. J. J. Jak, C. Konstapel, A. van Kreuningen, J. Verhoeven, J. W. M. Frenken, *Surf. Sci.* **457**, 295 (2000).

[83] R. Baker, P. Harris, R. Thomas, *Surf. Sci.* **46**, 311 (1974).

[84] W. T. Wallace, B. K. Min, D. W. Goodman, *J. Mol. Catal. A* **228**, 3 (2005).

[85] R.-J. Liu, *et al.*, *Microscopy and Microanalysis* **10**, 77 (2004).

[86] S. Helveg, *et al.*, *Nature* **427**, 426 (2004).

[87] D. Pearson, C. Ahn, B. Fultz, *Physical Review B (Condensed Matter)* **47**, 8471 (1993).

[88] T. S. Hummelshøj, Ni-metaloxid vekselvirkningen studeret med in situ transmissions elektron mikroskopi, Master's thesis, Technical University of Denmark (2005).

[89] L. Vitos, A. V. Ruban, H. L. Skriver, J. Kollár, *Surf. Sci.* **411**, 186 (1998).

[90] C. G. Granqvist, R. A. Buhrman, *J. Appl. Phys.* **47**, 2200 (1976).

[91] J.-O. Malm, *et al.*, *Angew. Chem. Int. Edit.* **27**, 555 (1988).

[92] J.-O. Malm, J.-O. Bovin, *Surface Science* **200**, 67 (1988).

[93] G. A. Somorjai, N. Materer, *Top. Catal.* **1**, 215 (1994).

[94] V. G. Gryaznov, A. M. Kaprelov, A. Y. Belov, *Phil. Mag. Lett.* **63**, 275 (1991).

[95] C. H. Bartholomew, R. B. Pannell, R. W. Fowler, *J. Catal.* **79**, 34 (1983).

[96] H. L. Gruber, *J. Phys. Chem.* **66**, 48 (1962).

[97] R. T. K. Baker, P. S. Harris, D. J. Kemper, R. J. Waite, *Carbon* **12**, 179 (1974).

[98] J. O. Bovin, R. Wallenberg, D. J. Smith, *Nature* **317**, 47 (1985).

[99] P. Harris, E. Boyes, *Inst. Phys. Conf. Ser.* pp. 275–278 (1983).

[100] J. Carrey, J. L. Maurice, F. Petroff, A. Vaures, *Phys. Rev. Lett.* **86**, 4600 (2001).

[101] R. S. Goeke, Novel catalyst supports for mechanistic studies of catalyst sintering, Master's thesis, University of New Mexico (2003).